RADAR SYSTEM STUDIES USING SIMULATION TECHNIQUES

(Studies of Pulse-Compression)

RADAR SYSTEM STUDIES USING SIMULATION TECHNIQUES

by

CARL MAGNUS THORSTEINSON, B.Sc., M.Eng.

A Thesis
Submitted to the School of Graduate Studies
in Partial Fulfilment of the Requirements
for the Degree
Doctor of Philosophy
McMaster University

(November) 1972

DOCTOR OF PHILOSOPHY (1972)
(Electrical Engineering)

McMASTER UNIVERSITY
Hamilton, Ontario.

TITLE: Radar System Studies Using Simulation Techniques

AUTHOR: Carl Magnus Thorsteinson,
B.Sc. (University of Manitoba)
M.Eng. (McMaster University)

SUPERVISOR: Professor S. S. Haykin

NUMBER OF PAGES: xiv, 221.

Abstract

Pulse-compression is a technique used in radar to transmit a long pulse while retaining the range resolution of a short pulse. The echo from the target is compressed in the matched filter of the radar receiver and the range resolution becomes equal to the width of the central peak of the auto-correlation function of the transmitted signal. A range tracking loop and a range surveillance moving target indicator (MTI) radar using pulse-compression techniques are studied in this thesis. The antenna of these systems is assumed to point along a constant azimuth to simplify the radar surroundings so that the nonlinear aspects of the circuits may be investigated.

In a range tracking loop the nonlinearity arises in the delay error feedback process, while in an MTI radar it arises through the limited dynamic range of the circuits used. This thesis presents a computer simulation study of these nonlinear radar systems using Monte Carlo techniques. The computer used in the study is of an interactive kind with oscilloscope display.

A new range tracking loop referred to as the decision-directed delay-lock loop has been developed using the fast Fourier transform (FFT) for cross-correlation with a stored replica of the transmitted signal. The loop uses all the lagged products of the FFT cross-correlator output, and is shown to have a wide dynamic range for large steps of input delay. Using signals already available in the loop, additional features

such as automatic feedback gain control and a mechanism for detection of unlocking are built into the loop.

The MTI pulse-compression radar has been investigated to determine the effect of a linear-limiting intermediate frequency (IF) amplifier on the signal-to-noise ratio (SNR) at the MTI output. For this study the FFT was used for the purpose of matched filtering and for generating various types of coherent clutter. It has been shown that large SNR losses due to the time-varying effective gain of the clutter-captured limiter may occur at some ranges with particular types of clutter spatial distributions.

Acknowledgement

I wish to express many thanks to my Ph.D. thesis supervisor, Dr. S. S. Haykin for his guidance during the course of this research and for the help he has given in many ways.

I would also like to thank Dr. R. de Buda for his continued interest in my work and for his valuable help with much of the theoretical analysis of Part II of this thesis.

I would like to thank the other members of my Ph.D. Supervisory Committee, Dr. S. H. Chisholm and Dr. T. J. Kennett.

Special gratitude is due to Ms. BettyAnne Bedell for speedy and accurate typing of this thesis.

Finally I would like to express thanks to the National Research Council of Canada for my scholarship and to McMaster University for my assistantship.

TABLE OF CONTENTS

LIST OF FIGURES, TABLES AND GRAPHS

Figure Page

Figure

Page

Preface

Two areas are investigated in this thesis by the method of interactive computer simulation. These areas are delay estimation and coherent MTI radar with envelope limiting. These two systems can be considered to use pulse-compression techniques. The two topics were investigated together in this thesis as they were both amenable to investigation by computer simulation using the fast Fourier transform for cross-correlation. Both systems contain nonlinear elements which make simulation desireable.

In the text the terms additive white Gaussian noise and thermal noise are used interchangeably. Also the words range and delay are intended to be equivalent.

In the MTI radar studies the complex envelope representation of signals is used. The computer simulation is restricted to baseband systems and thus the simulation and the complex envelope analysis should yield the same results as they are both baseband techniques. However the carrier frequency is important in nonlinear studies as harmonics are generated and the division of power in these harmonics is usually impossible to predict intuitively. Computer simulation is restricted from a precise standpoint to baseband systems and thus analytical work for carrier systems is still very much in demand.

Chapter 1

Introduction

In this chapter the scope and content of the thesis will be described. The thesis involves essentially a study of a range tracking radar and a moving target indicator radar by computer simulation and the method of Monte Carlo trials. In a certain sense, pulse-compression techniques are used in both radar systems. The two systems also have the common feature in that they both contain nonlinear devices which make their study by computer simulation highly desirable in order to obtain quantitative data and insight about their behaviour. In simulating these radars the fast Fourier transform (FFT) is used to perform cross-correlation with a stored replica of the transmitted signal. Good agreement is shown between the mathematical theory and the results of the simulation for both radar systems.

The development of the delay-lock loop is discussed in Chapter 2. The delay-lock discriminator automatically tracks the delay of a known analog waveform buried in noise. The loop can be developed from the concept of matched filtering; it is similar to the phase-lock loop. A hybrid (analog and digital) version of the delay-lock discriminator using fixed delay-lines switched in and out by the output of a cross-correlator was developed by the author for the M.Eng. degree.

In this thesis a new decision-directed delay-lock loop is described using the FFT for the purpose of cross-correlation. The formulation of this new delay-lock loop is the subject of Chapter 3.

The decision-directed loop operates by the method of maximum likelihood which was introduced by P. M. Woodward [26]. The statistics at the output of an FFT cross-correlator are measured in Chapter 3 to ensure that the "largest of" decision will be an optimum decision. Then for comparison purposes a computer simulation is developed of both a digital version of the delay-lock discriminator and the new decision-directed loop. The performance of the decision algorithms of the decision-directed delay-lock loop was optimized by operating these two simulated loops side by side.

Chapter 4 contains trials of the acquisition and tracking ability of the decision-directed loop. In addition the ability to detect unlocking and to automatically switch between the modes of tracking, unlocking and acquisition is demonstrated. The error bounds of the measurements were calculated using the equations for Monte Carlo error (which are developed in Appendix A).

The range tracking radar studied in Chapter 2, 3 and 4 can locate and track a target in thermal noise but the tracking decision algorithm will break down in a field of fixed clutter. One method of eliminating the effect of fixed clutter is to use a delay-line canceller. Radars using delay-

line cancellers are called moving target indicator radars or MTI radars. Most simple MTI systems have a limited dynamic range and are often therefore preceded by limiters to reduce the incoming dynamic range. In Chapter 5 the literature on the effect of limiters in MTI radar is reviewed. Bogotch and Cook [1] deal with the loss in detectability due to a hard-limiter in pulse-compression radar. Grasso and Guarguaglini [36] and Zeoli [37] are also relevant for coherent MTI radar.

A mathematical theory is formulated in Chapter 6 to study the effect of a linear-limiting IF amplifier in pulse-compression MTI radar. A linear-limiting IF amplifier will be interpreted to mean a circuit which is linear up to a threshold A and completely clips any of the signal envelope which exceeds the level A. Also in Chapter 6 a computer simulation using the FFT for cross-correlation and convolution, is developed to provide data to confirm the theory. The simulation employs complex pre-envelope signals to represent bandpass processes in the system.

The results of the simulation are given in Chapter 7. The cases of both fixed and fluctuating clutter are considered. It is assumed that the clutter exceeds the limiter threshold A by a considerable amount while the desired echo plus thermal noise alone would not exceed the limiter threshold A. Thus

we are considering a clutter-captured limiter in these studies. The Barker 13 biphase code and a 63 bit random code are tested in single and distributed clutter. A large signal-to-noise ratio loss is shown to occur when strong fixed clutter captures the limiter and attenuates the partially overlapping echo and noise to a time-varying degree. Fluctuating clutter is considered to demonstrate the problem of residual clutter produced at the MTI output. This residual clutter may be partially due to antenna scanning and to spectral spreading of the clutter by the limiter; however these two mechanisms are not considered specifically in this work.

The important contributions to the advance of knowledge produced by the study, and suggestions for future work are contained in Chapter 8.

Chapter 2

The Delay-Lock Loop

In this chapter the detection of known signals in Gaussian noise will be discussed. Basically, the detection of known signals in noise can be achieved using matched filtering or cross-correlation with a replica of the signal. Feedback can be applied around a cross-correlator to improve the tracking of weak signals in noise. Two loops which employ feedback around a cross-correlator are the phase-lock loop and the delay-lock discriminator. The delay-lock discriminator is a more general type of loop which will cross-correlate arbitrary analog waveforms in place of the sinusoids used in the phase-lock loop. When the variable delay of the delay-lock discriminator is replaced by binary weighted fixed delay-lines a new loop is produced which is called a quantized delay-lock discriminator. The all digital binary delay-lock loop uses a binary sequence generator such as a feedback shift register and a clock to produce a locally generated replica of the signal. The advent of small fixed-point computers and fast analog-to-digital converters allows a delay-lock loop to be built using computer hardware and software. Therefore the application of the fast Fourier transform (FFT) to cross-correlation is explored to prepare the way for the formulation of a new decision-directed delay-lock loop using FFT cross-correlation.

2.1 Matched Filtering

For illustrative purposes let s(t) be a signal the energy of which is almost entirely contained in a finite time interval. Let this signal be embedded in additive white Gaussian noise. A filter with the property of maximizing the signal-to-noise ratio at its output at one particular instant in time was first mentioned by North [2]. The impulse response of this filter should be the time reversed signal replica with sufficient delay T_o to insure realizeability. If the input to the filter consists of the desired signal s(t) and white Gaussian noise n(t) then for a matched filter with impulse response h(t) we may write the output y(t) of the filter as:

$$y(t) = \int_{-\infty}^{\infty} h(t-x)[s(x) + n(x)]\, dx$$

$$= \int_{-\infty}^{\infty} s(x-t+T_o)[s(x) + n(x)]\, dx \qquad (1)$$

The expected value of the filter output y(t) will be a maximum when $t = T_o$ in Equation (1) and this maximum value will be equal to the signal energy. Of course the improvement in signal-to-noise ratio is made by processing the incoming noisy signal so as to transform the elements of the signal plus noise into a new co-ordinate system where all the elements that are the same as the desired signal are maximized in one

dimension and all the elements due to noise are spread in the remaining dimensions. Thus we are maximizing the output signal-to-noise ratio by clever processing.

Equation (1) suggests an alternate method of matched filtering. The incoming signal plus noise may be multiplied by a stored replica of the signal and the product may be integrated. This process yields the cross-correlation between the input and the replica. The expectation of the cross-correlation is a maximum when the time of arrival of the signal is such that the stored replica and the signal component in the input are coincident in time.

Viterbi [3] has considered the transmission of bits and binary coded words over a channel with white additive Gaussian noise and detecting these messages by correlating them with stored replicas in the receiver. The error probabilities are determined as a function of the received signal energy per bit divided by the one-sided noise power per unit bandwidth, N_o.

2.2 Improving Cross-Correlation by the Application of Feedback

2.2.1 The Phase-Lock Loop

Matched filtering operations, in general, are easier to perform in the time domain by cross-correlation than in the frequency domain by filtering. For instance the detection of a sinusoid in white Gaussian noise requires a filter with a sinusoidal impulse response. If the impulse response does not decay with time then the filter is unrealizeable in practice because a narrow-band filter of zero bandwidth is required. It

is much easier to build an oscillator with a very stable sinusoidal output than to build a filter with zero bandwidth. Filtering is therefore replaced by cross-correlation with the oscillator.

Feedback from the correlator to the oscillator to control its phase allows the phase of the oscillator to track the phase of the incoming sinusoid. This filtering circuit with feedback is called the phase-lock loop and is shown in block diagram form in Fig. 1.

The correlator is made up of the multiplier and the low-pass filter. The time of integration T, is set by the bandwidth of the low-pass filter so that, approximately, the integration time is the reciprocal of the bandwidth of the low-pass filter. The frequency of the voltage controlled oscillator (VCO) is controlled by the voltage applied to it. The phase output of the oscillator is therefore proportional to the integral of the applied voltage, since frequency is $\frac{1}{2\pi}$ times the derivative of phase with respect to time.

The phase-lock loop will track the phase of the incoming sinusoid and produce an estimate of the phase, at any time, which is equal to the cross-correlation of the input and the oscillator output over the last T seconds. The phase error estimate of the correlator output is a nonlinear function of the phase error between the input sinusoid and the oscillator output. In addition the magnitude of this error voltage is proportional to the input sinusoidal amplitude which means that

the loop gain of the phase-lock loop is dependent on the input signal strength. These problems have been treated by Jaffe and Rechtin [4]. Using a linearized model of the phase-lock loop they derived compensating low-pass filters for the loop which minimize the sum of transient phase errors due to the specified input phase and phase jitter due to input noise. They also showed that a band-pass limiter was desireable before the input to the phase-lock loop to minimize the change in input power level. Jaffe and Rechtin demonstrated that a fixed component loop preceded by a band-pass limiter would yield near optimum performance over a wide range of input signal and noise levels. For communicating a message by radio transmission a radio frequency (RF) carrier is often used. The message is modulated onto the carrier by amplitude, frequency or phase modulation for example. For coherent reception of the modulation the phase of the received carrier must be available to the receiver. Viterbi [5] has considered an RF message system in which a reasonable estimate of the phase is available from a phase-lock loop. This receiver has been called a "partially coherent" receiver.

Gupta [6] has shown how to optimize the phase-lock loop filter when sampled data feedback is used. The filter which gives minimum summed square error of transient plus noise jitter is derived using modified z-transform techniques [7].

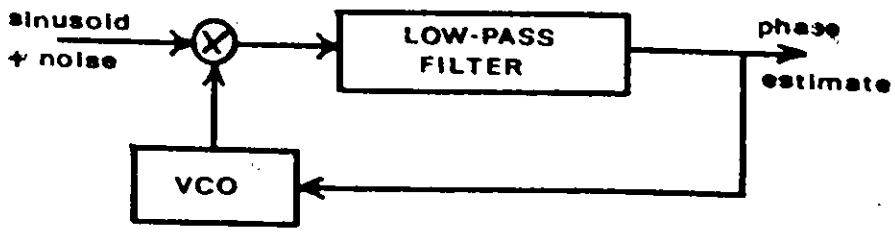

VCO - Voltage Controlled Oscillator

figure 1. The Phase-Lock Loop

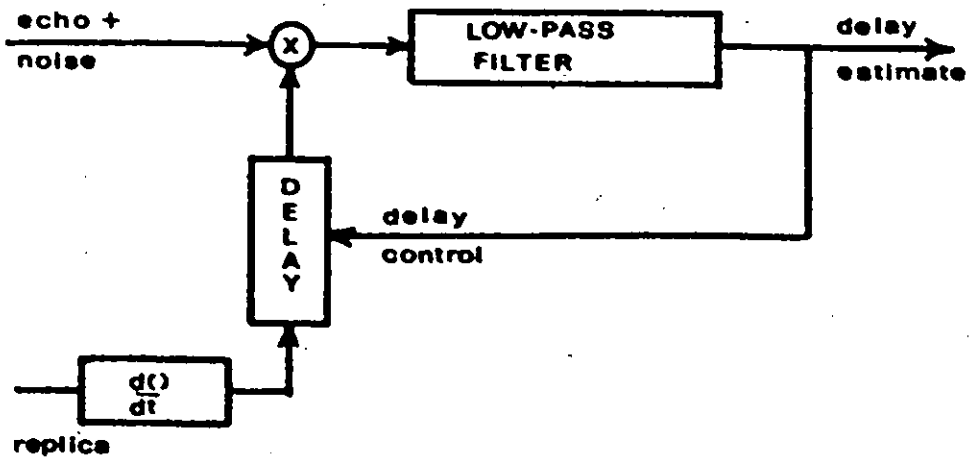

figure 2. The Delay-Lock Discriminator

2.2.2 The Delay-Lock Loop

Another cross-correlation system which uses feedback to improve the performance is called the delay-lock discriminator. This device described in 1961 as an optimum radar tracking device by Spilker and Magill [8] has the block diagram shown in Fig. 2.

The delay-lock discriminator as shown in Fig. 2 requires access to a noise free replica of the low-pass signal. This limits use of the device as shown, to applications where the receiver is located near to the modulator so that the signal may be used as the replica. Later a binary loop free of this restriction will be shown. The delay-line which delays the replica must have a continuously variable delay which can be controlled by an electrical signal. We shall consider only video low-pass signals and will discuss RF techniques for transmission later. Assuming such a delay-line is available the mean output of the low-pass filter in Fig. 2 will be proportional to the first derivative of the auto-correlation function of the replica signal. To show that the cross-correlation of a signal and its derivative produces the derivative of the autocorrelation function of the signal the following proof is presented. Let the signal be s(t), so that:

$$R_{ss}(\tau) = \lim_{T\to\infty} \frac{1}{2T} \int_{-T}^{T} s(t)\, s(t+\tau)\, dt \qquad (2)$$

$$\frac{d}{d\tau} R_{ss}(\tau) = \frac{\partial}{\partial \tau} \lim_{T\to\infty} \frac{1}{2T} \int_{-T}^{T} s(t)\, s(t+\tau)\, dt \qquad (3)$$

Assuming that $\int_{-T}^{T} s(t)\, s(t+\tau)\, dt$ is uniformly convergent for all τ we may take the partial derivative under the integration sign, thus:

$$\frac{d}{d\tau} R_{ss}(\tau) = \lim_{T\to\infty} \frac{1}{2T} \int_{-T}^{T} s(t)\, s'(t+\tau)\, dt \qquad (4)$$

where $s'(t+\tau)$ is the derivative of $s(\cdot)$ with respect to its argument. For example if the one-sided power spectrum of $s(t)$ is a low-pass Gaussian curve described by:

$$G(f) = \frac{2\sqrt{\pi}}{B_s} \exp - \left(\frac{\pi f}{B_s}\right)^2 \qquad (5)$$

where B_s is the frequency which bounds essentially all the signal power and $B_s = \pi \sqrt{2}\, \sigma_f = 4.44\, \sigma_f$ where σ_f is the standard deviation of the power spectrum, then by the Wiener-Khintchine theorem [9]:

$$R_{ss}(\tau) = \int_{0}^{\infty} G(f) \cos 2\pi f\tau \, df$$

$$= \frac{1}{\sigma_\tau \sqrt{2\pi}} \exp - \left(\frac{\tau}{\sigma_\tau \sqrt{2}}\right)^2 \qquad (6)$$

where $\sigma_\tau = \frac{1}{B_s\sqrt{2}} = 1/(2\pi\ \sigma_f)$ is the standard deviation of the normal autocorrelation curve $R(\tau)$. The error correction feedback is proportional to:

$$-R'_{ss}(\tau) = 2\ B_s^2\ \tau\ \exp - (B_s\ \tau)^2 \qquad (7)$$

where τ is the relative delay error between the echo and the delayed replica. The shape of the nonlinear feedback characteristic $-R'_{ss}(\tau)$ is shown in Fig. 3. As long as the relative delay error τ remains less than σ_τ in magnitude then the error characteristic is approximately linear. For $|\tau| > \sigma_\tau$ the feedback loop gain falls off rapidly. The value $\tau_{Max} = \sigma_\tau$ forms a threshold for the relative delay error, beyond which the loop may lose lock.

Viterbi [10] has calculated the statistical distribution of the tracking errors in first order phase-lock loops and delay lock-loops using Fokker-Planck techniques. The expected time to lose lock is calculated for any arbitrary periodic or nonperiodic odd error function. However the solution for higher than first order loops is beyond explicit mathematical solution and this impasse suggests that simulation studies using Monte Carlo techniques may be useful.

2.3 A Quantized Delay-Lock Discriminator

The difficulty of finding a suitable method of electrically controlling the delay of an analog replica prompted

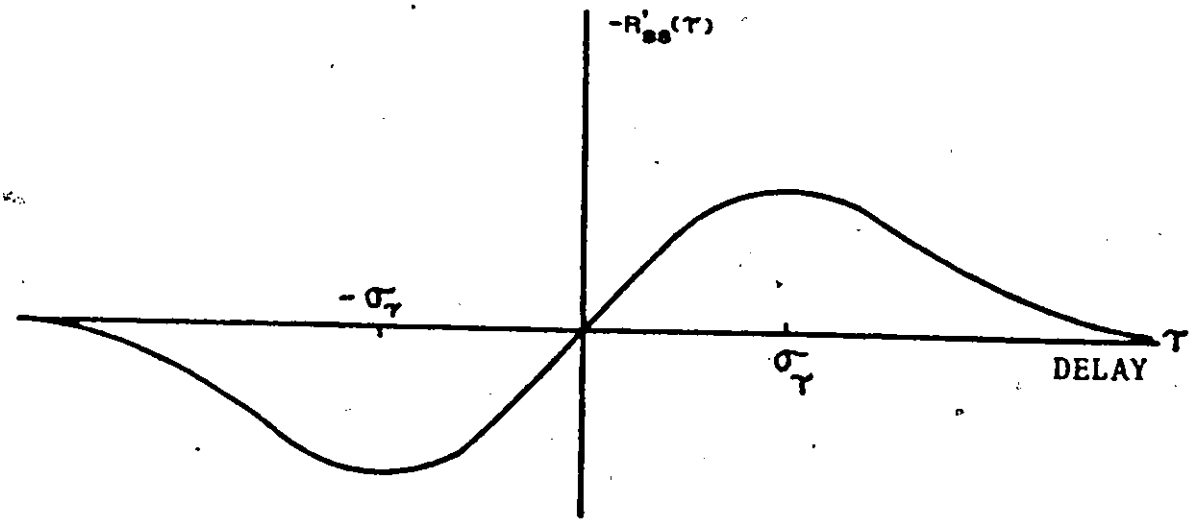

figure 3. Non-Linear Feedback Characteristic of the Delay-Lock Discriminator

the development of a new delay-lock loop for analog waveforms [11]†. Fixed delay-lines were switched in and out depending on the output of a correlator. The delay lines were made of different lengths in a binary weighted fashion and were controlled and switched by a simple binary counter. A block diagram of the system is shown in Fig. 4.

The completed loop would track the delay of analog signals of up to 2 MHz bandwidth by approximating the required replica delay by one of thirty-two evenly spaced fixed delays in the range zero to 7 3/4 μs. Very fast delay changes were possible and good linearity of output delay estimate versus input delay was demonstrated.

Details of the quantized delay-line are shown in Fig. 5 for two of the five stages of fixed delay. The two stages shown in Fig. 5 can provide four different delays, i.e., 0, 1/4, 1/2, and 3/4 μs. N stages of delay provide 2^N different fixed delays. The switching was accomplished by transistors and each delay-line was matched and isolated at each end by buffer amplifiers. The total delay was proportional to the binary number held by the stages of the binary counter. A reversible up-down counter was used and two methods of applying feedback were tested.

The simplest feedback was relay feedback, in which the counter was fed by a constant frequency clock and the sign

---

† The quantized delay-lock discriminator described, and shown in Fig. 4, was developed by the author in partial fulfilment for the M.Eng. degree (1968).

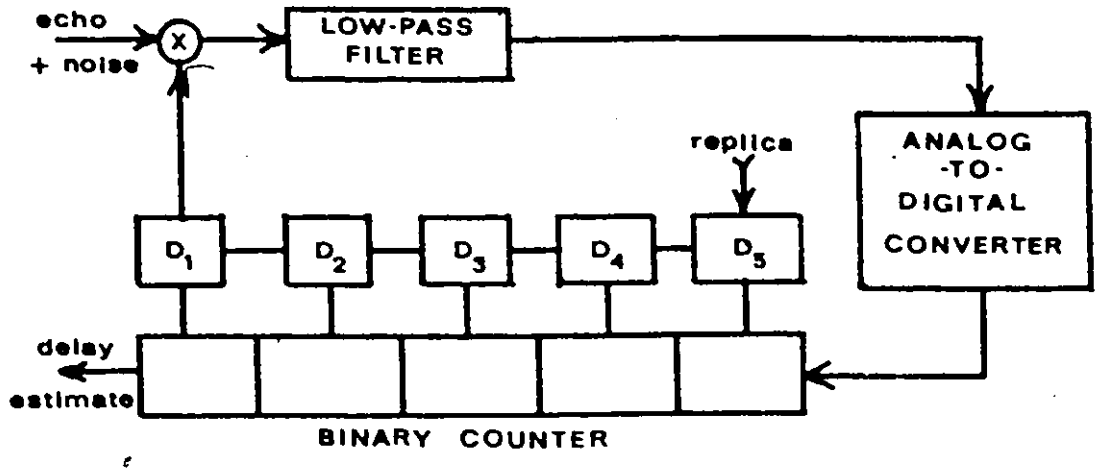

figure 4. A Quantized Delay-Lock Discriminator

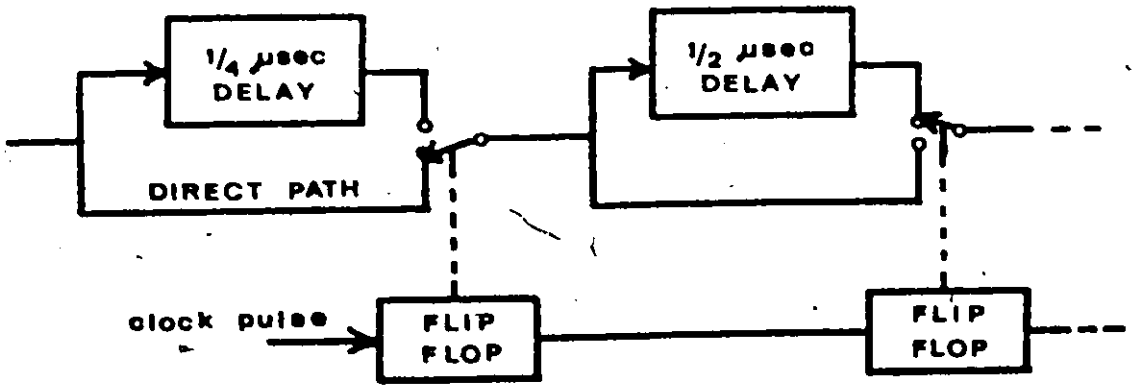

figure 5. Two Stages of the Quantized Delay-Line

of the correlator output controlled the direction of the counter. Alternately a more sophisticated feedback was provided by an analog-to-digital converter in which the number of pulses sent to the counter was proportional to the magnitude of the error.

For demonstration purposes the transmit signal was chosen to be a 30 kHz square wave. This wave was easily reproduced in delayed form by a 33 μs monostable multivibrator. A variable delay input echo was simulated by triggering the monostable from the output of an analog voltage differential comparator with one input tied to a 30 kHz linear voltage ramp. The delay estimate output of the quantized delay-lock discriminator is shown in Figs. 6(a) and 6(b) for relay feedback and analog-to-digital converter feedback, respectively.

2.4 The Binary Delay-Lock Loop

A delay-lock loop which tracks the delay of a binary pseudo-noise (PN) code composed of a shift register sequence of -1's and +1's, for example, was described by Spilker [12]. In this binary delay tracking loop the replica is generated within the receiver by a sequence generator and the delay of the replica is adjusted by controlling the frequency of the clock which drives the sequence generator. A block diagram of the video form of this binary delay-lock loop is shown in Fig. 7. The PN sequence generator usually produces a maximal length sequence, the M sequence, where N stages in the shift register produces a code with 2^N-1 bits or elements. In Fig. 8(a)

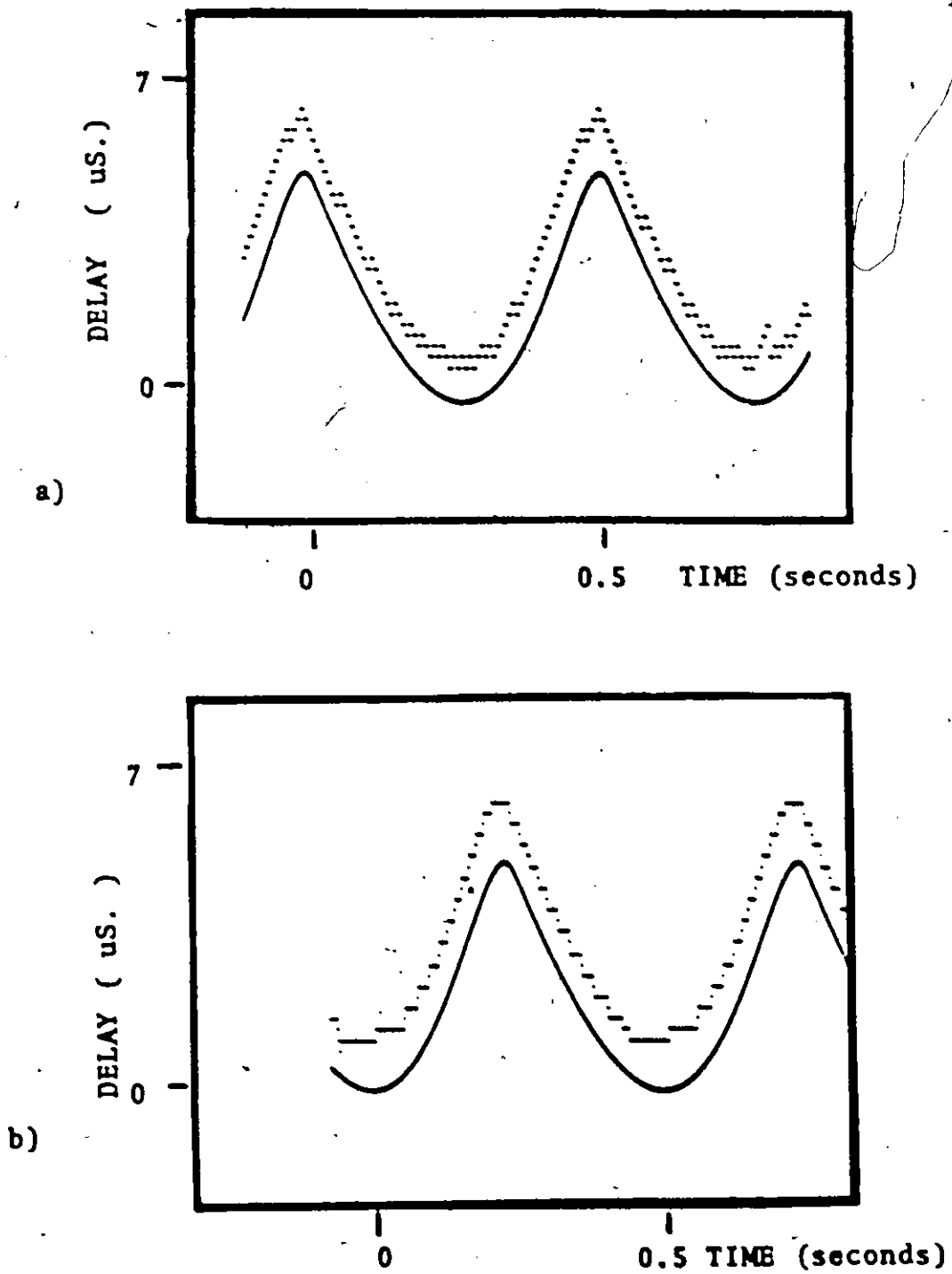

Figure 6. Delay Tracking Response to a Noise Free Echo for the Quantized Delay-Lock Discriminator with, a) Relay Feedback and, b) Analog-to-Digital Converter Feedback. In Each Photograph the Upper Trace is the Delay Estimate and the Lower Trace is the Delay of the Echo.

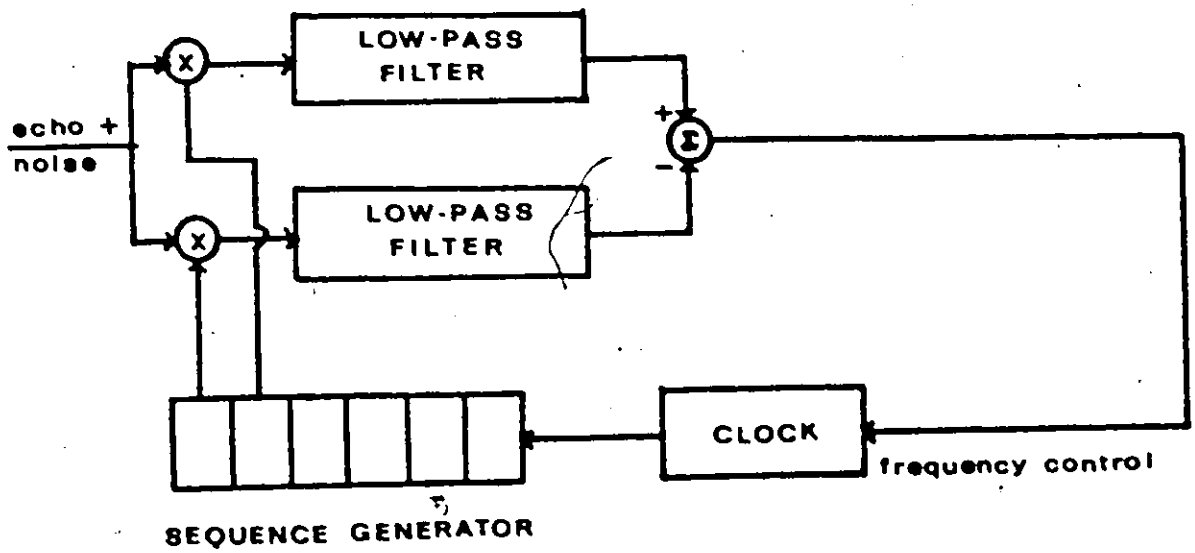

figure 7. The Binary Delay-Lock Loop

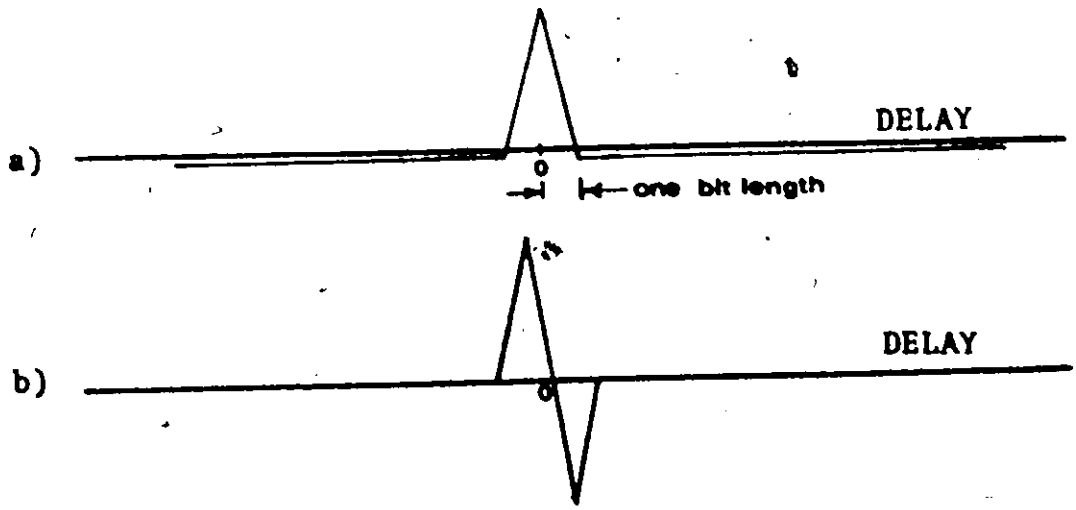

figure 8. a) The Autocorrelation Function of a Maximal Length Binary Sequence b) The Delay Error Characteristic Obtained by Cross-Correlating Against Two Replicas Spaced Two Bits Apart

the autocorrelation function of an M sequence is shown where the central peak is of a height equal to the number of elements and the sidelobes are equal to minus one for one element shifts [13]. The compression ratio which is equal to the length of the code before matched filtering divided by the length of the central peak of the autocorrelation function after matched filtering is therefore equal to the number of bits in the code. For example for N = 15, there are $2^{15} - 1 = 32,767$ bits or elements in the code. This very high compression ratio allows very low input signal-to-noise ratios to be used.

This binary delay-lock loop has several advantages over the conventional delay-lock discriminator. The binary loop does not need access to the transmitter replica but generates its own replica locally. The clock which advances the sequence generator takes the place of the variable delay-line and is inexpensive. In addition the multiplier may be replaced by a digital polarity coincidence detector such as an AND gate which is also inexpensive.

The delay error feedback correction is developed by cross-correlating the input against two replicas of the sequence spaced two bits apart. The corresponding error characteristic is shown in Fig. 8(b). When the loop is in lock a deviation in the relative delay of the input and the replica will cause an error voltage of the correct sign to be fed around the loop. Lock will be lost if the relative delay of the input and the replica exceeds two bits.

Gill [14] has considered the practical problem of transmitting the bits at RF and tracking the delay of the carrier modulation. Video, IF with envelope detection, and phase-coherent systems are considered. An IF envelope detection system is shown in Fig. 9(a) and a phase coherent system is shown in Fig. 9(b). A 3 db advantage in signal-to-noise ratio was shown for the phase-coherent delay-tracking loop over amplitude modulation. The phase-coherent system shown in Fig. 9(b) is similar to the "partially coherent" binary communication system described by Viterbi [15]. In systems in which a reasonable estimate of the phase of the carrier is obtained by a phase-lock loop the optimum modulation detector was shown by Viterbi to be a linear combination of the correlation detector and the squared envelope detector which are optimum for the coherent and noncoherent cases respectively.

The binary delay-lock loop has found many applications for range measurement particularly in satellite tracking and deep space communications. Ward [16] has proposed a loop which would communicate with a space probe to the planet Mars using very low signal-to-noise ratios. The extremely large compression ratios of the binary-delay-lock loop allow great signal enhancement. Ward and Strubel [17] also describe measurements of extremely precise range between a ground station and an orbiting satellite repeater. Using a 15 stage feedback shift register producing a code of length 32,767 bits, range measurements of 22,000 miles were performed with a total error of less than 120 feet, range jitter of about 3 feet and a readout resolution of one foot.

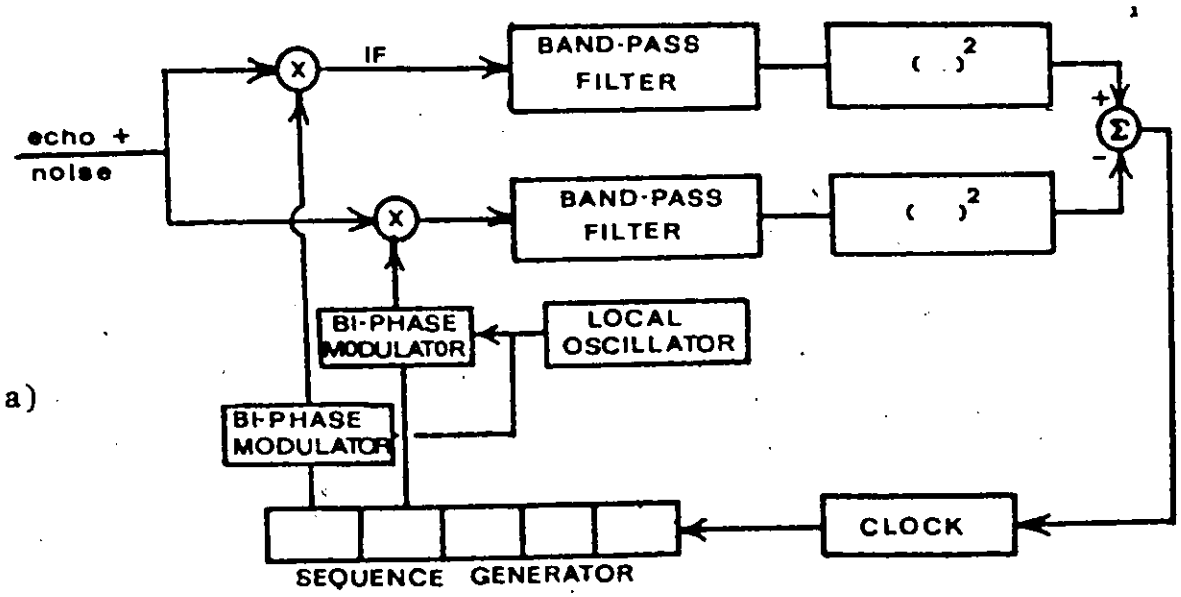

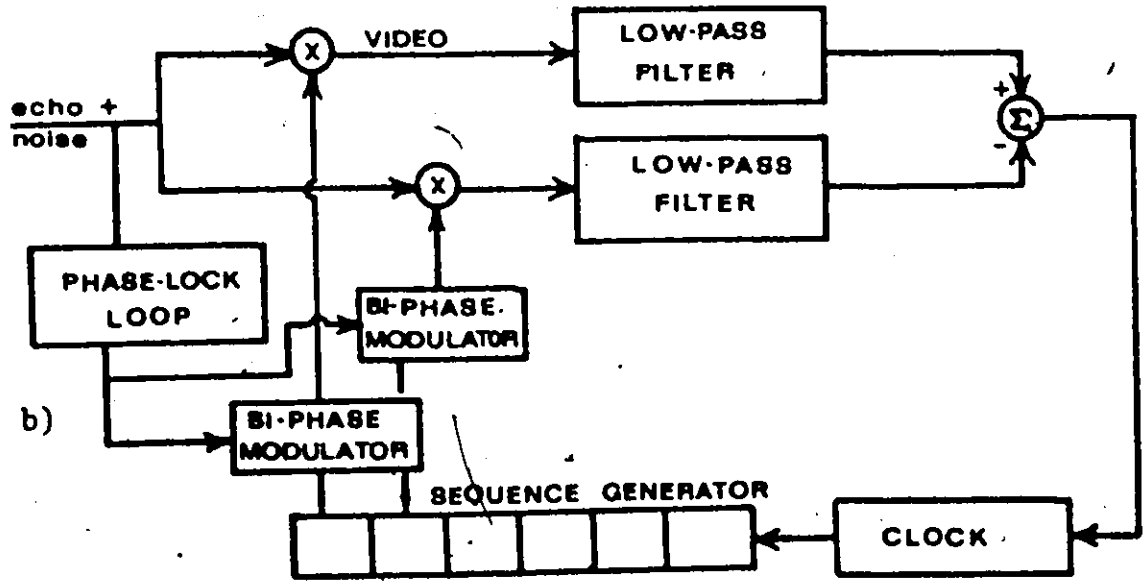

figure 9. Two RF Binary Delay-Lock Loops, a) Using IF Envelope Detection, b) Phase-Coherent.

Huff and Reinhard [18] have described and analysed a sampled data binary delay-lock loop which tracks the arrival time of a biphase modulated pulsed envelope radio frequency (RF) carrier. A PN code generator was used. The loop was intended to synchronize the pulsed envelope signals of a time-division multiple-access satellite system. Their synchronizing loop corresponds to that of Fig. 9(a) and provides bit synchronization for differential phase shift modulation.

2.5 The Fast Fourier Transform and Its Application to Correlation

The fast Fourier transform (FFT) [19] provides a convenient method of calculating the discrete Fourier transform (DFT) in a minimum amount of computer time. It makes use of an iterative algorithm which reduces the number of operations required to compute the transform by a large factor compared to classical methods.

Our interest in the transform lies in its speed and convenience in performing convolution and correlation for radar simulation. However the advent of hard-wired FFT processors for connection to data systems increases the speed to that of the real-time world for some applications. For instance a 1024 point transform can be completed in 22 ms. by equipment now in the field [20]. This implies real-time operation for signals with a bandwidth of 25 kHz. It is reasonable that advances in computer hardware will greatly increase this bandwidth.

There are a number of differences between the classical Fourier transform and the discrete Fourier transform

which must be understood to avoid some of the pitfalls [21] of blind FFT application. Consider, first, the mathematical operation of convolution which may be written in sampled form. This convolution takes N^2 operations.

$$y_c(t_k) = \Delta t \sum_{i=0}^{N-1} h(t_i)\, x(t_{k-i}) \qquad (8)$$

The summation of products of h and lagged values of x is referred to as the summation of lagged products. We may recognize this convolution as the inverse discrete Fourier transform of two input DFT's only when we give special attention to the indexes of the samples of h and x. Both h and x must be regularly sampled N times with a sampling period Δt and the lagged samples $x(t_{k-i})$ must be interpreted with k-i evaluated modulo N. This is equivalent to considering the input to be a periodic time function with period $N\Delta t$. The convolution operation as defined by Equation (8) is a circular or periodic convolution which we shall denote as $y_c(t_k)$; we may perform convolution using the FFT as follows:

$$y_c(t_k) = \text{FFT}^{-1}\,[\text{FFT}\,(h(t_k)) \cdot \text{FFT}\,(x\,(t_k))] \qquad (9)$$

$$= \text{FFT}^{-1}\,[H(f_n)\, X(f_n)]$$

The high speed convolution by FFT of Equation (9) takes a time proportional to 3N log N. The factor 3 arises from the two forward and one inverse FFT's required. For two arrays of N samples the FFT convolution is faster than direct methods when

N is equal to 32 or greater. For N = 1024 the saving in computation time over the direct method is approximately 50 times.

In a fast fixed-point FFT processor the samples are represented by fixed-point binary numbers. These numbers may be considered to be in integer form, i.e., 15 bits = 2^{15} = 32768_{10} and are subject to underflow (going smaller than 1) and overflow. The effect on error in convolution versus the number of bits used to represent the samples in the FFT is shown by Glisson, Black and Sage [22]. They also show the trade-off between automatic array scaling and conditional array scaling, two processes used to prevent overflow at intermediate stages in the computation.

The principal pitfall in FFT convolution lies in failing to allow for the circular nature of the output $y_c(t_k)$. In Fig. 10 the convolution of a narrow square and an RC impulse response are shown for two different cases. The effect of sampling too slowly, or of having an insufficient number of samples, is to introduce an undesireable additional component at the output of the convolution. This error component is due to aliasing which means that parts of the periodic output overlap and therefore add together and smear the output. The aliasing error can be reduced by taking enough samples so that the output of the convolution will have died to near zero before one period at the output is completed.

Two other pitfalls of FFT use are the "picket fence effect" and the "finite aperture" or "window" effect [21]. Of

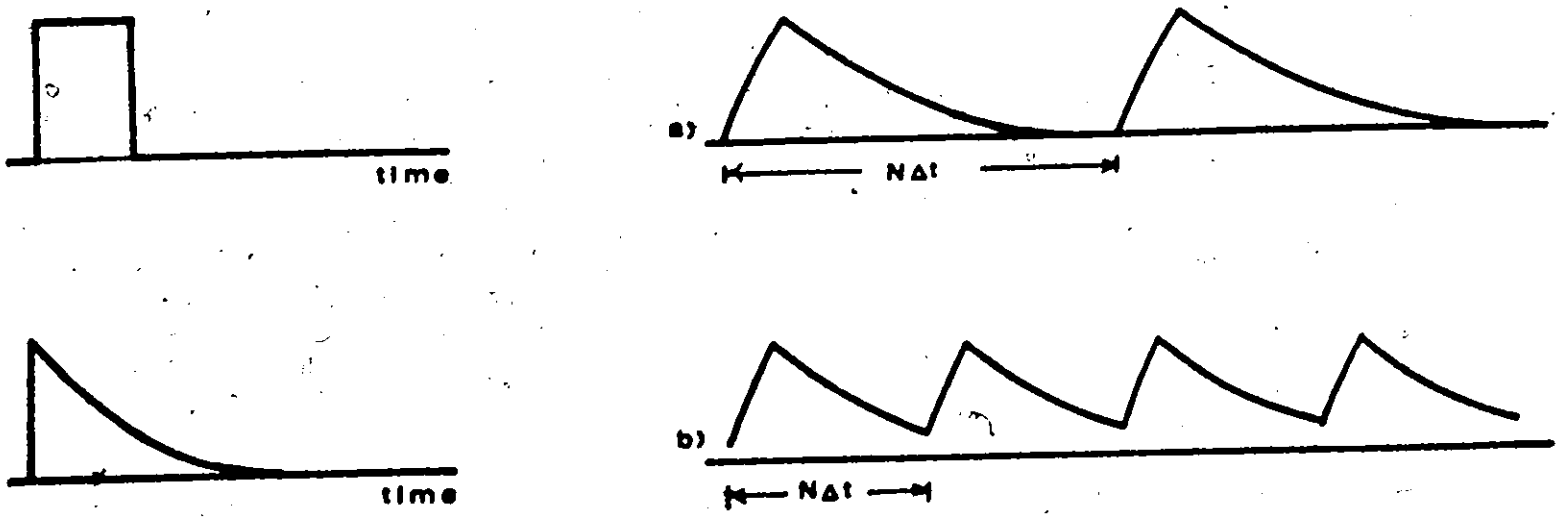

figure 10. The Circular Convolution of a Rectangle and a Low-Pass RC Impulse Response, a) Without Aliasing ($N\Delta t$ large), b) Illustrating Aliasing ($N\Delta t$ small).

these two pitfalls of FFT use the window effect is the only one which needs attention while performing discrete convolution. The window may introduce an unintentional discontinuity into the input data. In Fig. 11 a non-periodic low-pass noise waveform has been truncated and a periodic version created but this periodic version of the signal is discontinuous.

This discontinuity introduces a ringing into the output of the convolution process. The ringing may be avoided by designing an improved data window. In Fig. 12 an improved data window is shown along with its effect on the same low-pass noise waveform. Long data records may be convolved with short filter impulse responses by sectioning the input record and performing the convolution on each section separately. Two methods of sectioning records called overlap-add and overlap-save have been described by Cooley, Lewis and Welch [23].

Cross-correlation is performed on two sets of input data of equal size by first time-reversing one input. Thus cross-correlation used for matched filtering becomes identical to convolution with a filter impulse response which is the time-reversed replica of the desired signal.

Cross-correlation is subject to the same errors due to aliasing and finite data window, that occur in convolution. Aliasing errors in the autocorrelation output will not be a problem if the autocorrelation function of the desired signal falls to zero within a delay range less than one period of the correlator output. For our simulations this was the case so that no aliasing error was encountered. Also the ringing caused

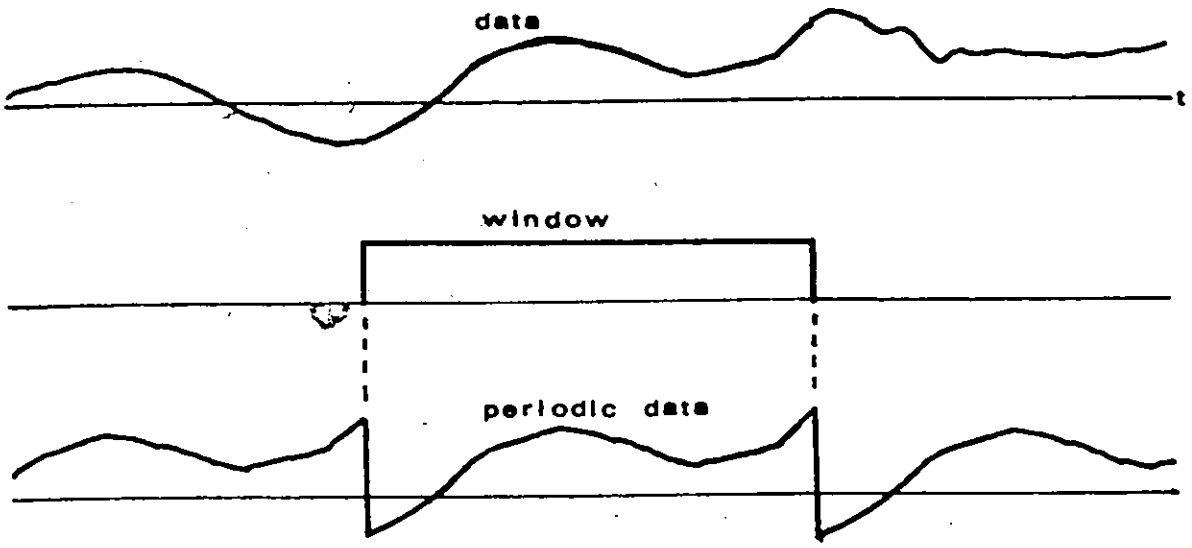

figure 11. The Discontinuity Introduced Into the Data by a Rectangular Data Window.

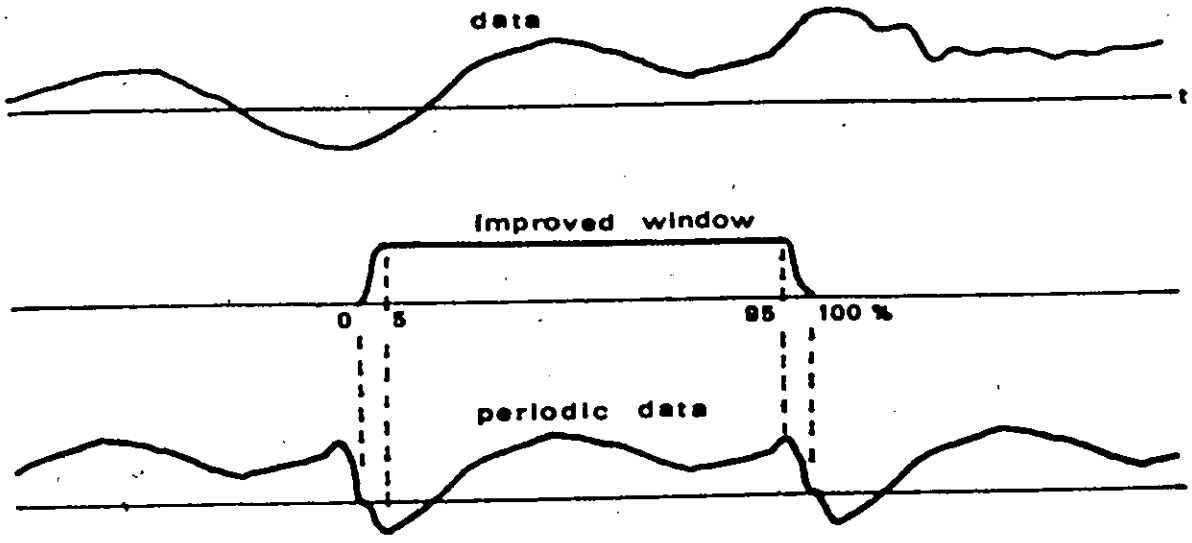

figure 12. Illustrating the Improved Data Window which Forces Continuity in the Periodic Data.

by window induced discontinuities in the input data was avoided in the simulation studies reported in Chapter 4 of this thesis by generating continuous periodic data, as will be described in Chapter 3.

Chapter 3

Formulation of the Decision-Directed Delay-Lock Loop using FFT Cross-Correlation

The advent of small high-speed fixed-point computers has enabled many new systems to be considered which were not previously possible or even economical. Indeed, the cost of computation is decreasing even as the speed of computation goes up. For continous tracking of radar range by a computer the process of FFT cross-correlation improved by feedback of computer made decisions suggests itself. Like the quantized delay-lock discriminator the delay would be quantized and the feedback loop would operate on correlator outputs which were discrete in time. The fast Fourier transform (FFT) can be used for cross-correlation and has the advantage that it produces the complete set of lagged products of the echo and the replica. Although the single lagged product of the delay-lock discriminator is adequate for closing the feedback loop, and can even be shown to be optimum for tracking some types of targets [8] the additional correlator outputs of the FFT are found to be useful for providing additional information about the target range.

In this chapter the assumptions as to the type of target, its surroundings, and its motion are stated. The range measuring signal waveform and the input noise are described. This is followed by Woodward's theory of delay measurement [26]. For the random low-pass signal used for range measurement a

random structure appears around the central peak of the auto-correlation. This random structure is called the "sidelobes" of the compressed signal. These sidelobes for a non-repetitive signal are also called "self-noise", as they arise from the interaction of non-overlapping parts of the signal return and the replica in the cross-correlation. The compressed output from the cross-correlator contains another "noise function" due to the action of the input noise and the replica. The statistics of this noise function are examined for white and "colored" input noise where colored refers to noise with the same spectrum as the signal. The simulation system is described including the computer and its peripherals. Finally the logical step-by-step development of a decision-directed delay-lock loop using FFT cross-correlation is described.

3.1 Formulation of the System

A decision-directed delay-lock loop using fast Fourier transform (FFT) correlation was simulated on the computer to explore the advantages of using the complete set of correlator lagged products which is produced by the FFT. The decision-directed loop was developed by a series of simulated experiments, often using a sampled version of the delay-lock discriminator for comparison of performance. Initially the decision-directed loop was implemented in a very simple form. Each deviation from ideal response which was discovered during the simulation, to be described, was cured by the addition of a refinement to the basic decision loop.

The radar signal to be transmitted, to be stored as the replica, and to be received as the echo was chosen from a random ensemble of real low-pass waveforms with a Gaussian power spectrum. These signals were generated in the computer by a process to be described. Although it is not practical to transmit a low-pass signal it may be modulated onto an RF carrier. If phase-coherent detection is available at the receiver a noise modulated range measuring radar could use a low-pass signal for phase modulation of the transmitted carrier and the delay-lock loop could determine the range from the phase modulation recovered by the demodulator. Transmitting and receiving a low-pass signal by frequency modulation or amplitude modulation is also a possibility, with some loss in signal-to-noise ratio [58].

For range measurement a random low-pass signal has the advantage that it never repeats itself, as a periodic signal does, so that the largest unambiguous range can be infinite. The Gaussian power spectrum produces such a desireable property, as do other random low-pass signals such as white noise passed through a filter with only poles on the negative real axis of the s plane [8]. The target was idealised as a real constant amplitude point reflector in a clutter free environment. It was also assumed that the strength of the echo would be constant regardless of the target range. This basic idealised target was buried in a background of thermal noise. This simple situation of target and noise was chosen to prove the viability of the decision-directed loop.

The rate of change of delay was also restricted. For a delay-lock loop preceded by a phase-lock loop for coherent demodulation we assume the Doppler frequency to be zero or to be tracked out of the low-pass modulation so that the only change in the low-pass modulation due to motion of the target is a pure change in delay. A "range bin" for the delay-lock loop is defined to be the smallest delay change resolvable by the low-pass modulation used in the delay-lock loop. For the delay-lock cross-correlation system the target is assumed to remain in one range bin long enough to integrate its echo for the length of time required by the correlator. During acquisition the target is required to be stationary in range.

The noise was assumed to be random Gaussian noise with a flat (white) spectrum. Only additive echo noise was considered. This white additive noise has the desireable property that after the replica is cross-correlated with the noisy echo, a one-dimensional decision space is produced in which the optimum decision as to target range involves simply choosing the largest peak of the correlator output [24] assuming no prior range probability is considered.

The case of wideband colored noise input was not studied extensively for the decision-directed loop as the main emphasis was on proving the viability of using feedback with FFT cross-correlation. However the cross-correlator output noise statistics were studied for the case of colored noise and procedures for producing a one-dimensional correlator output

were studied. The cross-correlation technique for colored echo noise involves first pre-whitening the replica and the noisy echo before cross-correlation [25].

3.2 Woodward's Theory of Delay Measurement

Woodward's theory [26] of delay measurement deals in a simple basic fashion with the theoretical problems of range measurement. Although the signals which he considers are continuous rather than sampled, the theory has wide application to sampled systems also. Later, theoretical values obtained from Woodward's theory will be used to explain and support the FFT correlation simulations.

The echo signal returned from the target is idealised to suffer only constant delay and the noise in the return is assumed to be additive white Gaussian noise. The received echo $y(t)$ is written as:

$$y(t) = u(t-\tau) + n(t) \tag{10}$$

where $u(t-\tau)$ is the delayed signal with delay τ and $n(t)$ is the noise.

The maximum information about the delay τ is gained from the return $y(t)$ by computing the posterior distribution of the probability of delay τ which is written as $p_y(\tau)$ indicating the probability density of τ given $y(t)$. This distribution is also referred to as the likelihood function of τ. We may write the probability density of τ given $y(t)$ as:

$$p_y(\tau) = k\, p(\tau)\, \exp\left\{-\frac{1}{N_o}\int_{-\infty}^{\infty} (y(t) - u(t-\tau))^2\, dt\right\} \quad (11)$$

where N_o is the one-sided power spectral density of the noise. In Equation (11) $p_y(\tau)$ is proportional to the probability of the noise waveform received, times $p(\tau)$ the prior probability of the delay τ, with k included to normalize $p_y(\tau)$. In Equation (11) the term $u(t-\tau)$ is the delayed signal replica with delay τ which is tested (for each value of τ) against the noisy delayed echo $y(t)$. Equation (11) may be simplified, for our purposes, by eliminating those terms not a function of τ. Expanding the integral inside the exponential in Equation (11) the terms $u^2(t)$ and $y^2(t)$ may be absorbed into k since they do not depend on the delay τ. Thus Equation (11) becomes:

$$p_y(\tau) = k_1\, p(\tau)\, \exp\left\{\frac{2}{N_o}\int_{-\infty}^{\infty} y(t)\, u(t-\tau)\, dt\right\} \quad (12)$$

This assumes that the transmitted energy and the received energy are constants. The integral inside the exponential is the "sufficient" part in that it is sufficient to enable the posterior distribution to be derived without further reference to y. Let us define $q(\tau)$ to be equal to the integral inside the exponential of Equation (12), thus:

$$q(\tau) = \frac{2}{N_o}\int_{-\infty}^{\infty} y(t)\, u(t-\tau)\, dt \quad (13)$$

We may write Equation (12) in a compact form.

$$p_y(\tau) = k_1\, p(\tau)\, \exp\,(q(\tau)) \tag{14}$$

In discrete form this equation may also be written as sums taken over successive samples of the waveforms y and u at regular intervals 1/2W in time, where W is the frequency beyond which y and u have no components.

$$p_y(\tau) = k_1\, p(\tau)\, \exp\,\{\tfrac{1}{N} \textstyle\sum_t y^* u^*\} \tag{15}$$

In the above equation y^* and u^* are written with an asterisk to denote their sampled form and N is the variance of the noise samples, $N = WN_o$. The function $q(\tau)$ may be separated into its signal and noise components.

$$q(\tau) = g(\tau) + h(\tau) \tag{16}$$

$g(\tau)$ is called the signal function and $h(\tau)$ is called the noise function.

$$g(\tau) = \frac{2}{N_o} \int_{-\infty}^{\infty} u(t-\tau_o)\, u(t-\tau)\, dt \tag{17}$$

$$h(\tau) = \frac{2}{N_o} \int_{-\infty}^{\infty} n(t)\, u(t-\tau)\, dt \tag{18}$$

The signal function $g(\tau)$ can be expressed as $\frac{2}{N_o} R_u(\tau-\tau_o)$ where $R_u(\tau)$ is the autocorrelation function of u(t). Accordingly $g(\tau)$ has a maximum at $\tau = \tau_o$ the true delay

of the target and the value of this maximum is:

$$g_{max} = 2E/N_o = R \tag{19}$$

where E is the integrated square of the signal u(t).

The noise function $h(\tau)$ is a random function of τ. Its value for any particular τ is a weighted average of the original noise n(t) and therefore has a Gaussian distribution of zero mean. The variance of $h(\tau)$ is given for the case of discrete samples as:

$$\overline{h^2} = \left(\frac{1}{WN_o}\right)^2 \Sigma\, WN_o\, u^{*2} \tag{20}$$

$$= \frac{2E}{N_o} = R$$

Evidently the parameter R is a fundamental quantity. R is in fact the total signal energy divided by the energy of the noise in one degree of freedom.

Besides being the peak value of the signal function $g(\tau)$, the parameter R is the variance of the noise function $h(\tau)$, and the target peak squared to noise variance ratio of the target and noise peaks in $q(\tau)$. Therefore $\sqrt{R}$ is the peak to root mean square ratio of the correlator output. The value of R thus tells a great deal about the quality of the posterior distribution $p_y(\tau)$. If R is small then the target peak in the correlator output $q(\tau)$ may be small compared to the noise. The target posterior range is therefore ambiguous.* When R is large the target peak g_{max} will be seen clearly above the correlator

* The range estimate variance is greater than a lower bound, see [24], p. 275, eqn. (106).

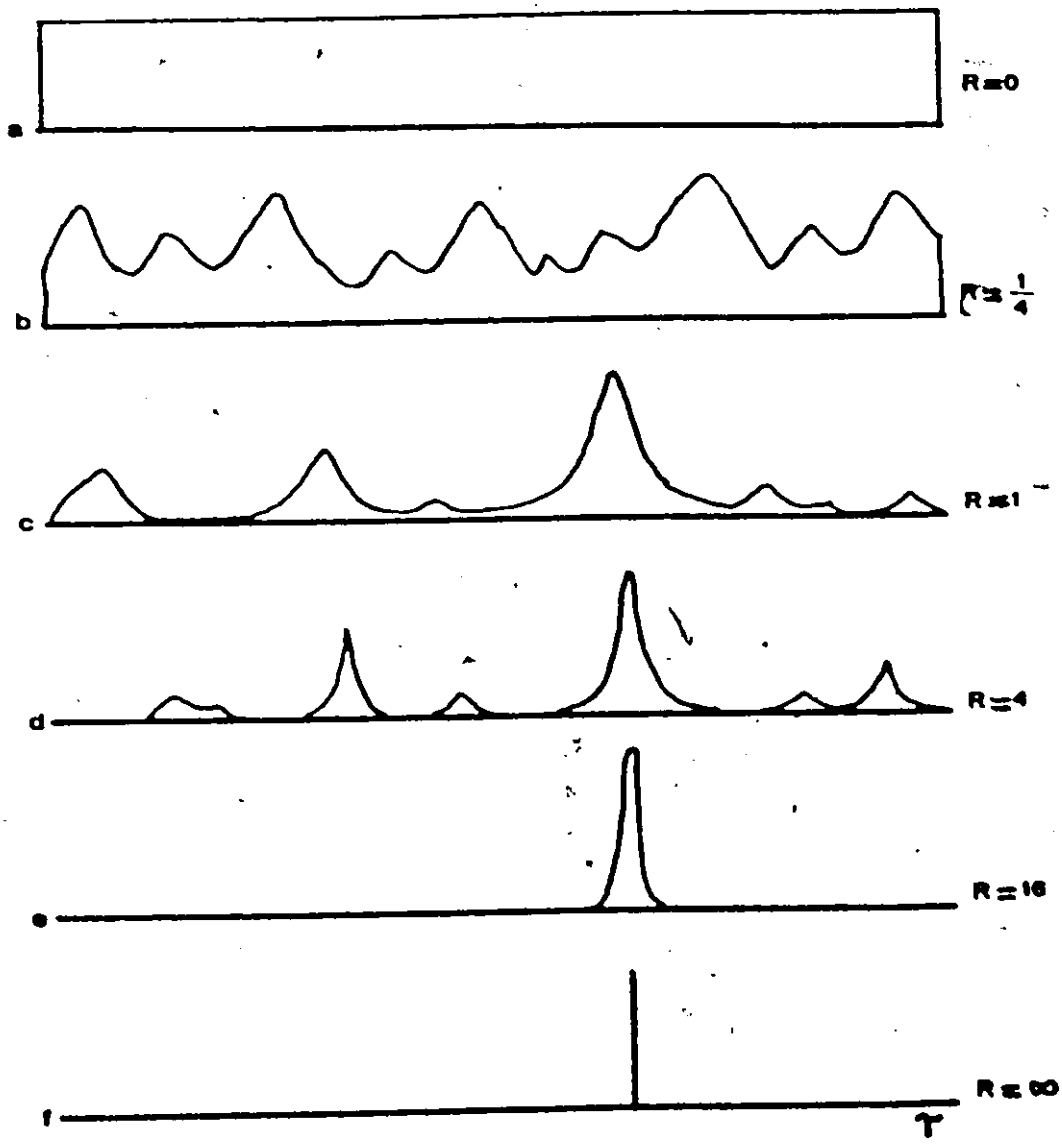

figure 13. The Structure of the Likelihood Function $p_y(\tau)$ for Various Values of the Cross-Correlator Output Signal Function to Noise Function Ratio "R" (from Woodward [26]).

noise. A series of graphs of the likelihood function $p_y(\tau)$ for various values of R is shown in Fig. 13.

The structure of $p_y(\tau)$ falls into two classes. The first when R is large shows one obvious target range and the noise is negligible. The second when R is small shows a large number of equally likely possibilities for the posterior target range when the noise peaks often exceed the target peak.

The "threshold of intelligibility" is chosen as that value of R at which the area under the true target peak and the total area under the noise peaks are equal. This threshold value of $R = R_t$ is given by:

$$R_t \doteq 2 \ln R_t \Upsilon\beta \qquad (21)$$

where $\Upsilon\beta$ is the product of the bandwidth β of the signal and the prior possible range extent Υ.

Information about the delay τ is gained at two different rates depending on the value of R. At high signal-to-noise ratio where R is large the target peak at the cross-correlator output appears unambiguously. But the posterior distribution need not have its peak at precisely the delay τ because the noise causes the peak of the signal plus noise function to be displaced by an amount approximately equal to the variance of the peak $p_y(\tau)$ [27]. When R is above the threshold R_t the accuracy of the observation of delay increases as $\sqrt{R}$ and the gain of information therefore increases logarithmically with R. The following equation is given by Woodward for $R > R_t$.

$$I_1 = \frac{1}{2} \ln \left(\Upsilon\beta\right)^2 R/2\pi e) \qquad \text{nats} \quad (22)$$

$$R > R_t$$

where $\Upsilon\beta$ is the prior delay range times the signal bandwidth as before and e is the base of natural logarithms. In Equation (22) I_1 is the rate of gain of information given in natural units called nats (as opposed to log to base two units of information called bits). When R is small and $p_y(\tau)$ is ambiguous then the rate of gain of information is given by:

$$I_2 = \frac{1}{2} R - \frac{1}{2} \ln (2\pi R/e) \qquad \text{nats} \quad (23)$$

These two rates of gain of information are shown in Fig. 14 for $\Upsilon\beta = 30$.

This graph of rate of gain of information will be referred to later in the chapter on results to explain the operation of the decision-directed loop.

3.3 Theory of Self-Noise in Circular Correlation

Woodward's signal function as defined in Equation (17) includes the assumption that the signal function has one well defined maximum and falls quickly to zero on both sides of this maximum. This assumption holds for pulsed radar bursts and for continuous radar signals if an infinite amount of integration time is available. However for a short time segment of a random low-pass function the assumption does not hold. In particular consider a 1024 sample section of a random

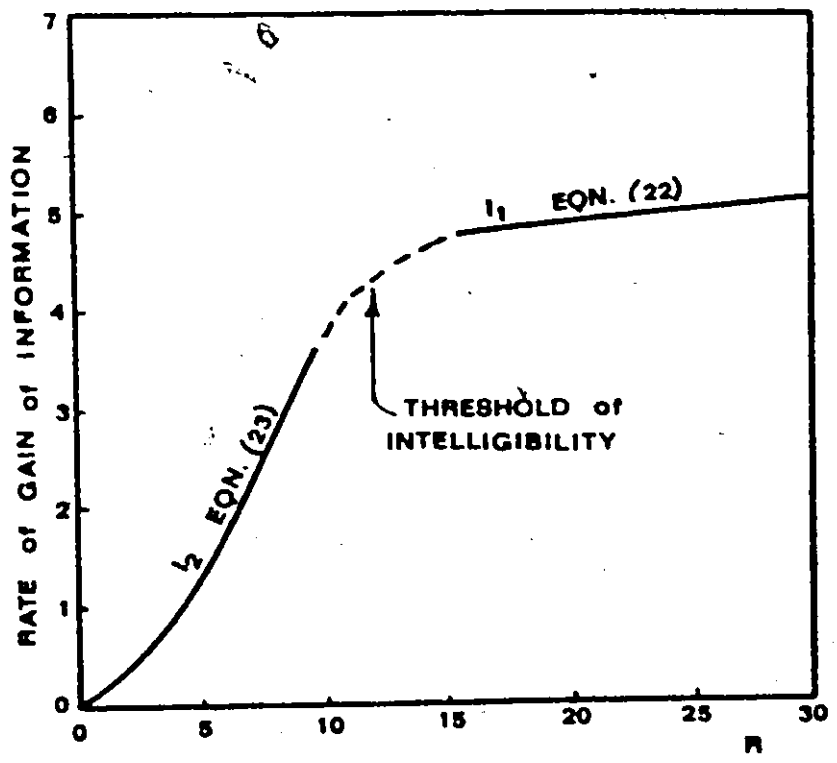

figure 14. The Rate of Gain of Information (nats per cross-correlator iteration) Versus R.

low-pass signal with a Gaussian power spectrum. It will be convenient here to assume that the variance of the power spectrum is equal to 50 samples since this was the spectrum used in the simulation.

The circular cross-correlation used to detect the range of the target is shown in Fig. 15. Without loss of generality assume that the delay of the target is zero. If the input noise component $n(t_k)$ is assumed to be zero then the discrete cross-power spectrum $S^2(f_k)$ has no significant frequency components greater than the 24^{th} complex component as shown in Fig. 20(b). The equivalent rectangular spectrum to that of Fig. 20(b) has 15 equal strength frequency components. For simplicity the self-noise problem will be reduced to the case of independent samples at the correlator output. This can be done by reducing the sampling rate of the circular signal function $R_c(\tau_k)$ as shown in Fig. 15 until the critical Nyquist sampling rate is reached. For the signal spectrum considered with an equivalent spectrum having 15 equal strength independent frequency components as few as 30 samples of the circular autocorrelation function may be taken without undersampling.

The low-pass signal may be sampled in time at this reduced rate. Let the independent samples of the time signal be a_i, $i = 1, 2, \ldots 30$ and let the a_i be chosen from random white Gaussian noise with variance equal to unity. This simplified model of the cross-correlation will be used to calculate an upper bound on the circular signal function-to-noise

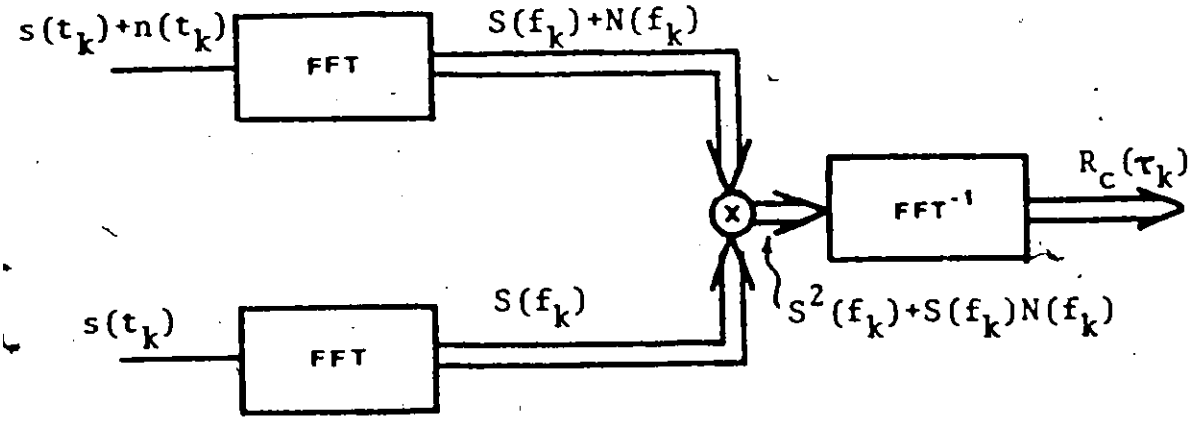

figure 15. The Circular Cross-Correlation using the FFT. $s(t_k)$ is the Sampled Signal and $n(t_k)$ is the Sampled Noise.

function energy ratio R. The circular autocorrelation function of the independent time samples a_i may be written:

$$R_c(N) = \sum_{i=1}^{30} a_i \, a_{i+N} \tag{24}$$

where i+N is evaluated modulo 30. The central peak $R_c(0)$ of the circular autocorrelation function is equal to:

$$\overline{R_c(0)} = \overline{\sum_{i=1}^{30} a_i^2} = 30. \tag{25}$$

where the bar denotes mean value. The sidelobe structure of $R_c(N)$ is made up of those values of $R_c(N)$ with $N \neq 0$. The individual products in Equation (24) $m = a_i \, a_{i+N}$, $N \neq 0$, have a variance which was calculated by simulation. The Gaussian distribution of the samples a_i is written:

$$p_a(a_i) = \frac{1}{\sqrt{2\pi}} \exp(-a_i^2/2) \tag{26}$$

where the value of a_i is restricted to magnitudes less than six due to the method by which the random Gaussian numbers were produced [28]. This limitation has little effect on the product m as the probability of a Gaussian variable exceeding six times the standard deviation is negligible. Accordingly 10,000 products $m = a_i \, a_{i+N}$, $N \neq 0$ were squared and summed to yield the mean square value:

$$\overline{m^2} = 1.02 \pm 0.03 \tag{27}$$

The error bounds shown are for a 90% confidence level and were obtained by estimating the variance of 10 trials of 1000 products each by the Monte Carlo method (see Appendix A). In fact it can be shown from theory that $\overline{m^2} = 1$ which is proven as follows.* Let the probability density of $m = a_1 a_2$ be $p_m(m)$. The elements contributing to the product m where m is constant lie along a hyperbola defined by $m = a_1 a_2$ thus:

$$p_m(m)\, dm = p_a(a_1)\, p_a(a_2)\, d a_1\, d a_2 \qquad (28)$$

We may integrate Equation (28) with respect to a_1 using the substitition $a_2 = m/a_1$, $d a_2 = dm/a_1$:

$$p_m(m) = 2 \int_0^\infty \frac{1}{2\pi} \exp\left(-\frac{a_1^2}{2} - \frac{m^2}{2a_1^2}\right) \frac{da_1}{a_1} \qquad (29)$$

Because of Equation (29) we may assume without loss of generality that "m" is positive. Let $x = a_1^2$ and $dx = 2 a_1\, d a_1$ so that Equation (28) may be written in the form

$$p_m(m) = \frac{1}{2\pi} \int_0^\infty \exp\left[-\frac{m}{2}\left(\frac{x}{m} + \frac{m}{x}\right)\right] \frac{dx}{x} \qquad (30)$$

We may express the bracket inside the exponential in Equation (29) as a hyperbolic cosine function by making the substitution $\frac{x}{m} = e^y$

---

* An alternate proof is as follows:

$$E\{m^2\} = \int_{-\infty}^{\infty} \int_{-\infty}^{\infty} a_1^2\, a_2^2\, p_a(a_1)\, p_a(a_2)\, da_1\, da_2$$

$$= \left[\int_{-\infty}^{\infty} a_1^2\, p_a(a_1)\, da_1\right]^2 = 1$$

so that $dx = m\, e^{y}\, dy$ and we may write Equation (30) in the form:

$$p_m(m) = \frac{1}{2\pi} \int_{-\infty}^{\infty} \exp\left[-m\left(\frac{e^{y} + e^{-y}}{2}\right)\right] dy$$

$$= \frac{1}{2\pi} \int_{-\infty}^{\infty} \exp\left[-m \cosh y\right] dy \qquad (31)$$

From tables of definite integrals [29] we find Equation (31) is one definition of the modified Bessel function of order zero commonly denoted as $K_o(m)$. We may write the solution to the integral in Equation (31) as:

$$p_m(m) = \frac{K_o(m)}{\pi} \qquad (32)$$

Finally the variance of the product $m = a_1\, a_2$ where a_1 and a_2 are independent random Gaussian numbers with unity variance is given by:

$$\overline{m^2} = 2 \int_{o}^{\infty} m^2\, p(m)\, dm \qquad (33)$$

Thus we substitute Equation (32) into Equation (33) and using tables of Bessel integrals [30] we find:

$$\overline{m^2} = 2 \int_{o}^{\infty} \frac{m^2\, K_o(m)}{\pi}\, dm = \frac{4\, \Gamma^2(3/2)}{\Gamma^2\left(\frac{1}{2}\right)} = 1. \qquad (34)$$

where $\Gamma(\frac{1}{2})$ is the Gamma function [29] evaluated for the argument 1/2. We may compare the variance of m obtained by simulation Equation (27) with the variance obtained by theory

Equation (34) and note that they agree within the measured experimental error. We may now calculate the variance of the sidelobes of $R_c(N)$ defined by Equation (24).

$$\overline{R_c^2(N)} = \overline{\sum_{i=1}^{30} m_i^2} = 30. \ , \ N \neq 0 \tag{35}$$

The ratio of the energy of the central peak of the autocorrelation function to the energy of the sidelobes is, from Equation (24) and (25),

$$R_{max} = \frac{\overline{R_c^2(0)}}{\overline{R_c^2(N)}_{N\neq 0}} = \frac{30^2}{30} = 30 \tag{36}$$

Thus the self-noise of the random low-pass signal limits the maximum correlator output signal function to noise function energy ratio to less than 30 even when the input noise is reduced to zero. This places a restriction on the amount of information about target range which can be obtained from one correlator output. Substituting $R_{max} = 30$ into Woodward's equation for rate of gain of information at large values of R, Equation (22) the maximum information gained per correlator output is:

$$\begin{aligned} I_{1_{max}} &= \tfrac{1}{2} \log_2 (\tau^2 \beta^2 R_{max}/2\pi e)) \\ &= \tfrac{1}{2} \log_2 (30^2 \cdot 30/2\pi e) \\ &\doteq 5 \text{ bits} \end{aligned} \tag{37}$$

where Υ_β is the number of resolvable range elements in the prior range interval Υ. If the correlator output has 1024 samples of range then 10 bits of information are required to pick one range sample from all the others, in the absence of prior information about range. Thus it can be inferred that the signal used is not capable of pinpointing range to one sample in 1024 in one correlator output or iteration. More information per iteration could be gained by increasing the bandwidth and the compression ratio of the signal.

3.4 The Covariance of the Circular Noise Function at the FFT Cross-Correlator Output

The covariance along the delay axis of the circular noise function was obtained by averaging circular noise products at the correlator output. The circular noise function is defined by:

$$H_c(k\Delta\tau) = H_c(k) = \sum_{i=1}^{N} n(t_i)\, s(t_{i-k}) \qquad (38)$$

where $n(t_i)$ is the noise sampled at time $i\Delta t$ where $\Delta\tau = \Delta t$ and $s(t_{i-k})$ is the sampled signal with the index i-k evaluated modulo N. The covariance of the circular noise function is written:

$$R_H(k) = E\ \{H(m)\ H(m-k)\} \qquad (39)$$

where m and k are integers and E {·} stands for expectation of the argument. The covariance of the noise function $R_H(k)$ is important as it indicates if any further processing of the

correlator output would increase the output signal-to-noise ratio. Both white and colored input noise are considered.

The transmitted signal was chosen to be random Gaussian low-pass noise as obtained by passing white noise through an RC low-pass filter with a cut-off frequency at 200 Hz. The resulting noise waveform was converted to digital form by a 14 bit analog-to-digital converter sampling at a 25 kHz rate. The white noise and colored noise to be added to the signal were also obtained from the same source.

The signal plus noise was cross-correlated with a noise free signal replica using an FFT convolution of 1024 sample arrays. After cross-correlation the mean target peak was subtracted from the output and the covariance of the remaining noise function was computed. The circular autocorrelation function of the signal $R_s(k)$ was fitted to an empirical formula given by:

$$R_s(k) \doteq (3680/3313)\ \mathrm{EXP}\ (-\ 0.051\ k) - (318/3313)\ \mathrm{EXP}\ (-\ 0.003\ k) - (44/3313)\ \mathrm{EXP}\ (-\ 1.1\ k) \qquad (40)$$

Thus to a first approximation the circular autocorrelation function of the signal was an exponential decay on the positive delay axis with a decay constant of $1/0.051 = 19.6$ samples. From theory for an RC low-pass noise with a cut-off frequency of f_o Hz the corresponding autocorrelation function is given by:

$$R(\tau) = \int_0^\infty 2\, G_s(f) \cos \omega\tau \, df \qquad \omega = 2\pi f$$

$$= \int_0^\infty 2 \frac{K/2}{1 + (\omega/\omega_o)^2} \cos \omega\tau \, df \qquad (41)$$

$$= K \frac{\omega_o}{4} \text{ EXP } (- \omega_o |\tau|)$$

where $\omega_o = 1/RC = 2\pi f_o$ and K/2 is the input white noise power to the RC filter given in volts^2 per Hz, and $G_s(f)$ is the power spectrum of the low-pass signal.

Comparing Equation (41) and (40) we can calculate the measured cut-off frequency of the RC low-pass filter; thus:

$$f_o = \frac{\omega_o}{2\pi} = \frac{25000}{2\pi} \times 0.051 = 203 \text{ Hz} \qquad (42)$$

where 25000 corresponds to the sampling rate. This agrees closely with the actual cut-off frequency at 200 Hz as indicated previously.

The measured signal circular autocorrelation function $R_s(k)$ is graphed in Fig. 16. The circular noise function covariance $R_H(k)$ is also shown in Fig. 16 for both white and colored input noise. Here "colored" noise means noise having the same spectrum as the desired signal. It can be shown theoretically that the covariance of the noise function is equal to the convolution of the two autocorrelation functions of the signal and the noise respectively. This proof is restricted to infinite sample sizes and will be given here in terms of continuous waveforms. The theoretical curves of Fig. 16 were

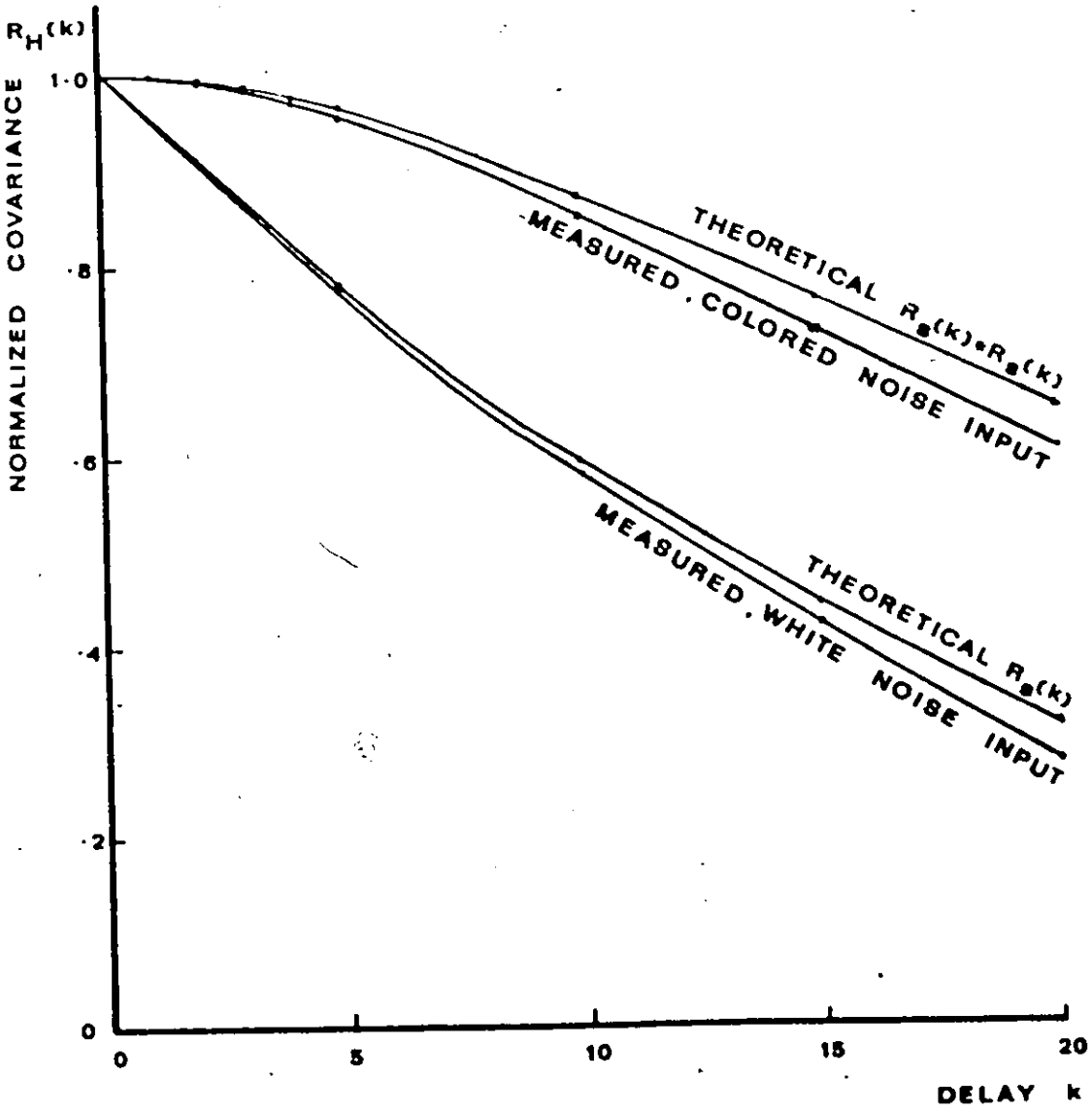

figure 16. The Covariance of the FFT Cross-Correlator Output Noise Function for White Noise and Colored Noise Input.

calculated using this theorem.

Let $R_{ss}(\tau)$ be the autocorrelation function of the signal and let $R_{nn}(\tau)$ be the autocorrelation function of the noise. $R_h(x)$ is the covariance of the noise function $h(\tau)$. We may draw a model matched filter, Fig. 17, which may not be realizeable because of the infinite extent of the signal.

The power spectral density of the noise function output of the filter is given by:

$$G_h(f) = B^2(f)\, G_n(f) \tag{43}$$

where B(f) is the frequency transfer function of the matched filter. But the filter has the impulse response s(-t) and hence:

$$B^2(f) = G_s(f) \tag{44}$$

where $G_s(f)$ is the power spectral density of the signal. Hence we may write:

$$G_h(f) = G_s(f)\, G_n(f) \tag{45}$$

and the inverse Fourier transform of this equation is:

$$R_h(x) = F^{-1}\{G_h(f)\} = F^{-1}\{G_s(f)\, G_n(f)\}$$

$$R_h(x) = R_{ss}(\tau) * R_{nn}(\tau) \tag{46}$$

where the asterisk denotes convolution. For example if the noise is white and $R_{nn}(\tau) = \delta(\tau)$ where $\delta(\tau)$ is an impulse occurring at $\tau = 0$ then we may write:

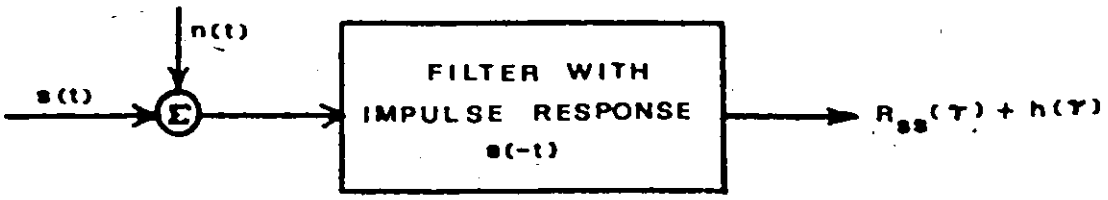

figure 17. A Matched Filter Model of Cross-Correlation.

$$R_h(x) = R_{ss}(\tau) * \delta(\tau) = R_{ss}(x) \tag{47}$$

and if the noise is colored and has the same spectrum as the signal then:

$$R_h(x) = R_{ss}(\tau) * R_{ss}(\tau) \tag{48}$$

Theoretical curves from Equations (47) and (48) have been plotted in Fig. 16. From the agreement between theory and the measured covariance of the FFT correlator output we conclude that the finite sample sizes used in FFT correlation do not alter the statistical theory of signal detection. Thus for our delay detector we shall use a correlator followed by a "largest of" detector. For this purpose, we may reduce the received waveform to a single number which is a point in a decision space. This operation is performed physically by a correlation operation and is invariant to the decision criterion that we plan to use [31]. For example when the noise input is white, the circular noise function has a covariance equal to the circular autocorrelation function of the signal. When this state is reached at the correlator output no further maximization of the target signal function to noise function energy ratio is possible. We conclude that picking the largest correlator output is an optimum detection rule for white input noise, notwithstanding the finite sample size and the self-noise produced by the signal.

3.5 Computer Peripherals and Subroutines Available for Simulation

The simulations were performed on a fixed-point computer (CDC 1700) having analog-to-digital converters, an FFT subroutine, and digital-to-analog converters for oscilloscope display. A high speed disk storage holding 1.5 million 16 bit samples provided intermediate storage for data and results. The analog-to-digital converter had 14 bit accuracy and was used to convert analog random Gaussian noise to random digital samples. The FFT subroutine would accept arrays of complex 14 bit samples and convert, say, 1024 complex time samples to 1024 complex spectral coefficients.

The circular cross-correlation of two input time sequences is performed by first time-reversing one of the sequences before storing it in its array. Next each input array is converted in place to a discrete spectrum by a forward FFT. By multiplying each spectral coefficient by its corresponding coefficient in the other array, an array of cross-power spectral components was generated, the inverse FFT of which would yield the circular cross-correlation of the two time input arrays.

Before, during and after cross-correlation the arrays were observed on an oscilloscope after buffered digital-to-analog conversion to 15 bit accuracy. The observation of these arrays corresponds to measuring and observing analog voltages on an oscilloscope and serves three important purposes. Firstly the display ensures that no intermediate results have overflowed.

Secondly the display provides a fast convenient way of observing the elements of the correlator output (the decision space). Thirdly it allows the stored results to be retrieved from disk storage and photographed.

3.6 The Simulation Block Diagram

The delay-lock discriminator is a range tracking device with a block diagram shown in Fig. 2. The replica is differentiated with respect to time in order that the output of the correlator will contain the first derivative of the signal autocorrelation function with respect to delay (see chapter 2, section 2.2.2 for a proof). When the autocorrelation function is a maximum the first derivative with respect to range passes through zero. Thus an error correction voltage nonlinearly dependent on range, equal to the differentiated autocorrelation function, appears at the cross-correlator output and supplies the corrective feedback.

The delay-lock discriminator was simulated in discrete form as shown in Fig. 18(a). The multiplier and low-pass filter of the analog device were replaced by the FFT cross-correlator. The FFT cross-correlator acts in a manner equivalent to a multiplier followed by an integrate and dump filter where the time of integration is equal to the time over which the input time sequences were taken. The first difference of the FFT cross-correlator output is taken in place of the device which differentiates the replica in the corresponding analog delay-lock discriminator. Although only the central element

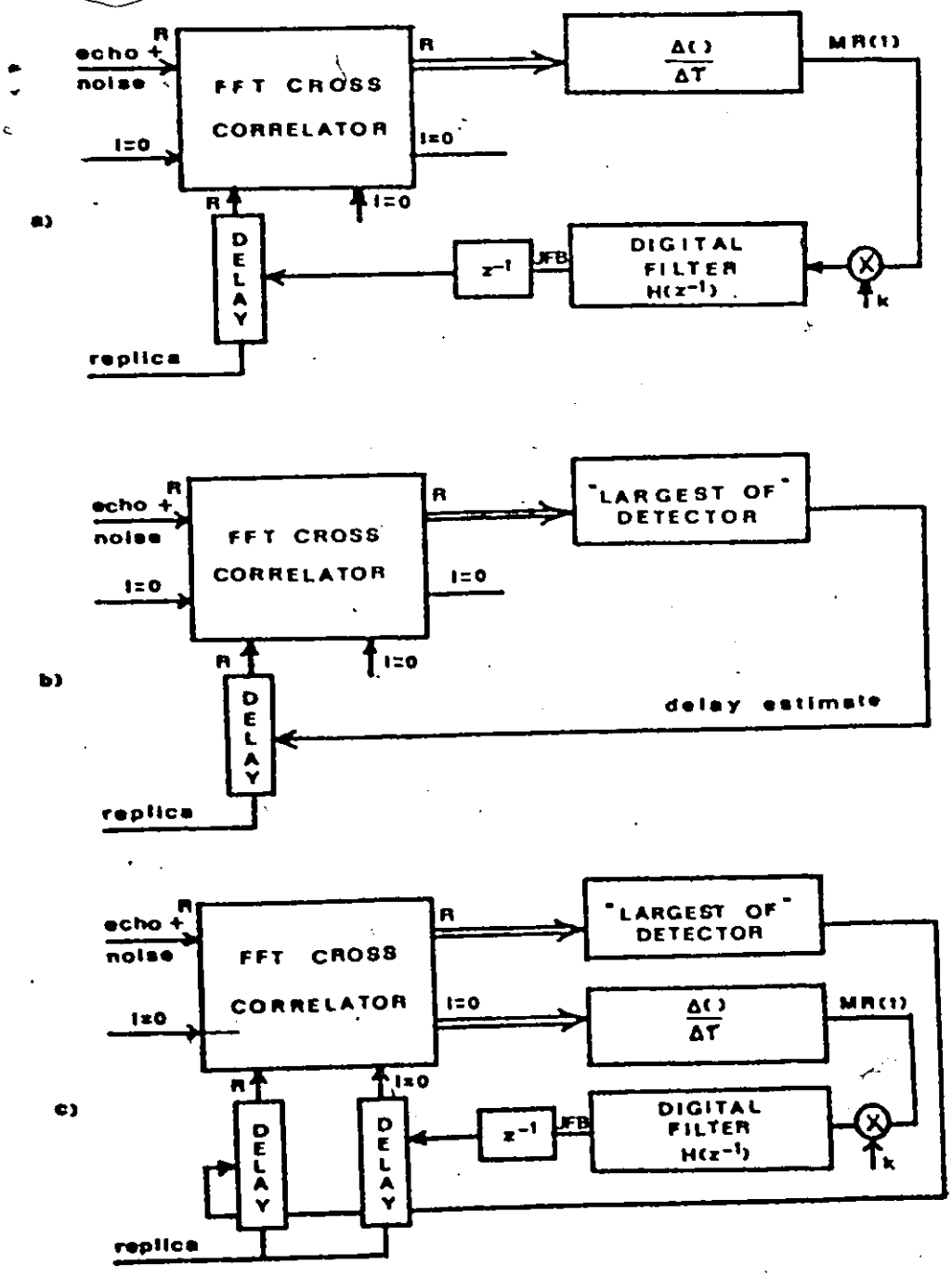

figure 18. Side by Side Simulation of the Two Delay-Lock Loops,a) Delay-Lock Discriminator,b) Decision-Directed Delay-Lock Loop c) The Two Delay-Lock Loops Combined. R is the Real Input and I is the Imaginary Input.

MR(1) of the first difference of the correlator output is fed back, the entire first difference was observed during simulation to examine the cause of nonlinear response. A constant k multiplies the output MR(1) to control the loop gain. This delay-lock discriminator operates as a sampled data feedback loop in that the output of the correlator can only be sampled periodically at the end of each correlator period. The digital filter with transfer function $H(z^{-1})$ has input k.MR(1) and an output denoted by JFB. The unit-delay operator z^{-1} at the digital filter output serves to represent the fact that the digital filter output JFB has no effect on the loop until the end of the next cross-correlator period or iteration. In other words the presence of the z^{-1} as a multiplying factor inside the feedback loop assures real-time realizeability [32].

The corresponding decision-directed loop is shown in Fig. 18(b). The "largest of" detector helps identify the delay of the largest peak of the cross-correlator output. The delay estimate obtained in this way is fed back to correct the delay of the replica. Notice that a differentiator is not necessary in this case and that all of the lagged products of the cross-correlator are used in the decision process.

The two loops of Fig. 18(a) and 18(b) have real inputs. In Fig. 18(c) the functions of the delay-lock discriminator and the decision-directed loop are carried out simultaneously by FFT processing of two real signals as real and imaginary parts of one complex signal. This was done in order to compare the

performance of the two devices side by side.

The task of generating the required signals with Gaussian power spectrum has been simplified by allowing the inputs to be white noise and shaping their spectrum after the first FFT as shown in Fig. 19. This was done for two reasons. First, by neglecting shaping the spectrum of the signal until absolutely necessary the repetitious filtering of long input records was eliminated. Second, by shaping the white noise spectra and then using an inverse FFT to produce the input time sequence the continuity of the input data was guaranteed and the ringing due to "window effect" was avoided (see Chapter 2, section 2.5).

The variable delay was simulated by transferring 15,360 samples of white noise to the disk storage and picking up the section of noise desired by means of a word addressable disk driver subroutine. The input noise on the disk was renewed after each correlator output.

The array used to weight the voltage spectrum at the output of the FFT is shown in Fig. 20(a). This weighting $S_w(f_k)$ was equal to the square root of a Gaussian curve having a variance of 50 samples and is given by:

$$S_w(f_k) = 15000\ [\exp(-k^2/100)]^{1/2} \qquad (49)$$

$$k = 0, \pm 1, \pm 2, \ldots \pm 512$$

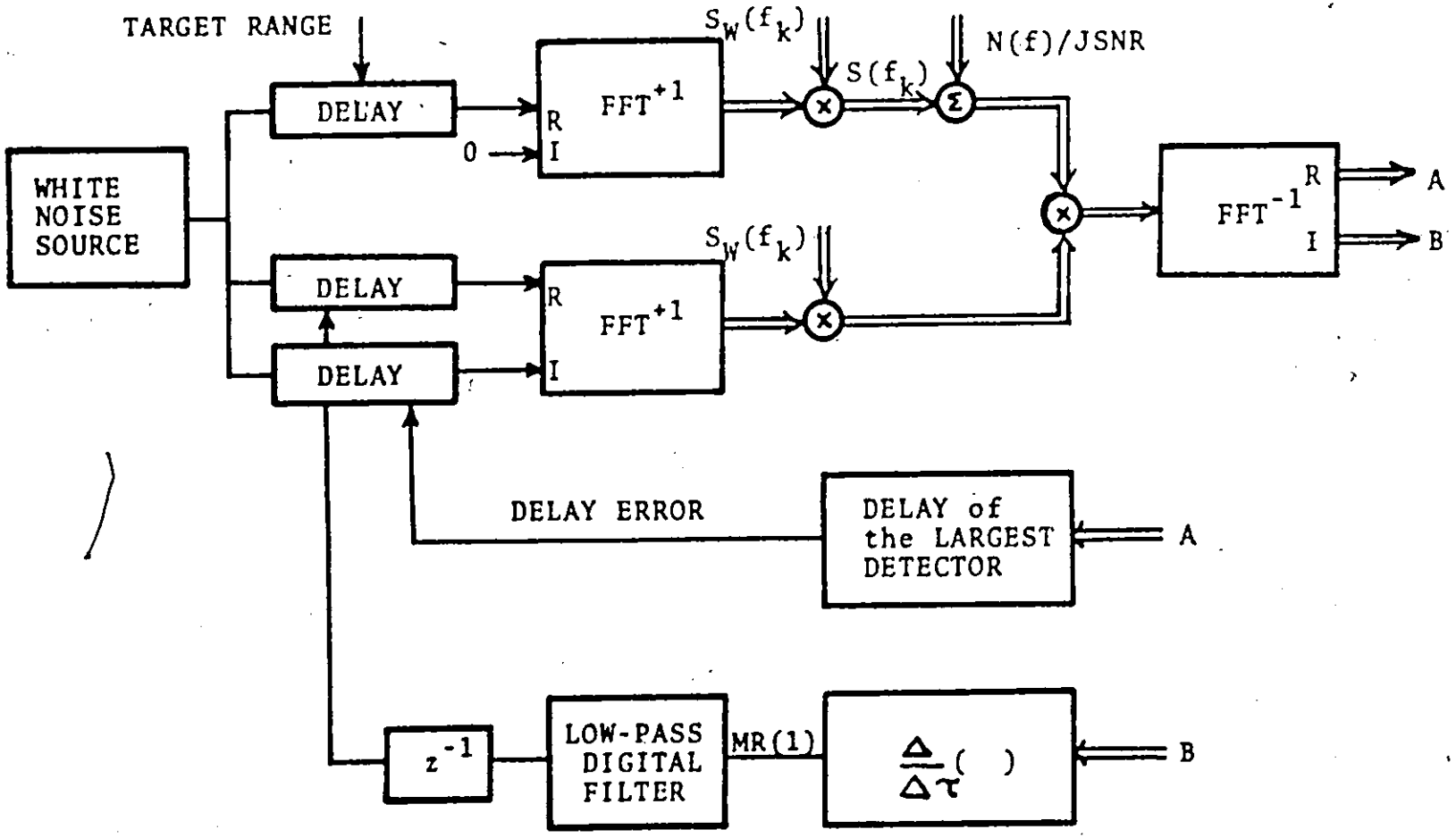

figure 19. Details of the Method of Spectral Weighting and the Addition of White Input Noise. Notice the Factor JSNR Which Controls the Amplitude of the Input Noise.

A typical spectrum obtained by weighting white noise is shown in Fig. 20(b) and the corresponding sequence in time obtained by an inverse FFT is shown in Fig. 20(c). The two ends of the time sequence wrap around and join at the origin of Fig. 20(c) showing a smooth joint with no discontinuity.

In Fig. 19 details of the spectral weighting and the addition of white noise are shown. Notice that the white noise is added to the delayed input signal only after the target delay and the first FFT. This saves time otherwise spent in adding noise to the entire possible input sequence of 15,360 samples. As the voltage spectrum of white noise is also white [33] this simplification is justified. The signal-to-noise ratio was controlled by dividing the noise by an integer quantity called JSNR in the simulation program. In section 3.8 this parameter will be related to $R = 2\ E/N_0$ where E is the total signal and $N_0/2$ is the noise energy in one degree of freedom. A signal plus noise time sequence is shown in Fig. 21 for JSNR = 2. As a result of the cross-correlation of the replica with the target echo plus noise the correlator output forms many smooth peaks, all similar to the autocorrelation function of the noise free signal and one of these peaks must be identified as the target. In Fig. 22 the correlator output and the first difference of a similar correlator output are shown. The delay-lock discriminator generates its feedback on the basis of one central element of the first difference shown. The decision-directed loop makes its decision on the basis of the entire set of lagged products

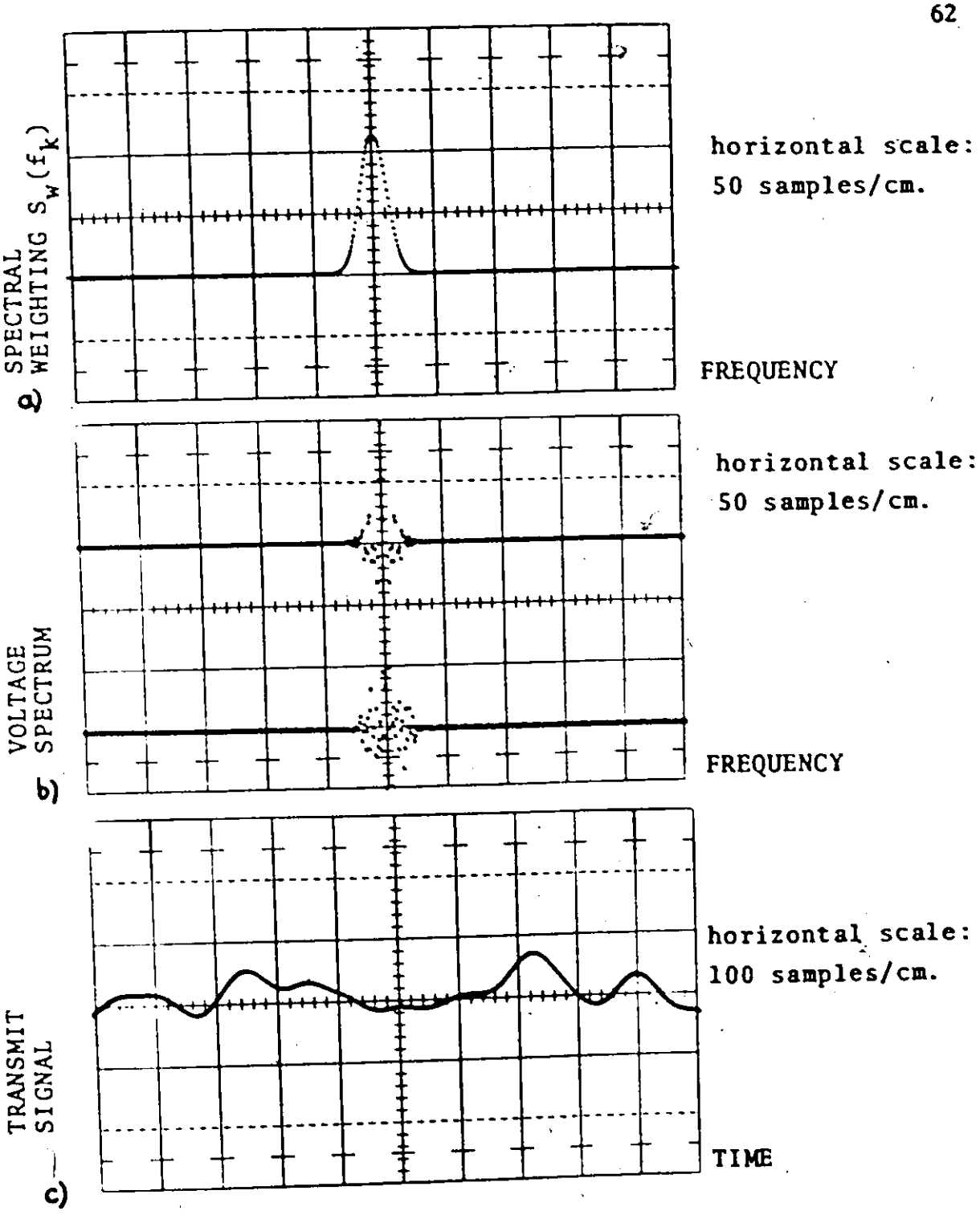

figure 20. Generation of the Transmit Signal, a) Spectral Weighting (Eqn. (49), b) Typical Spectrum, c) Transmit Signal Obtained by Inverse FFT of Typical Spectrum.

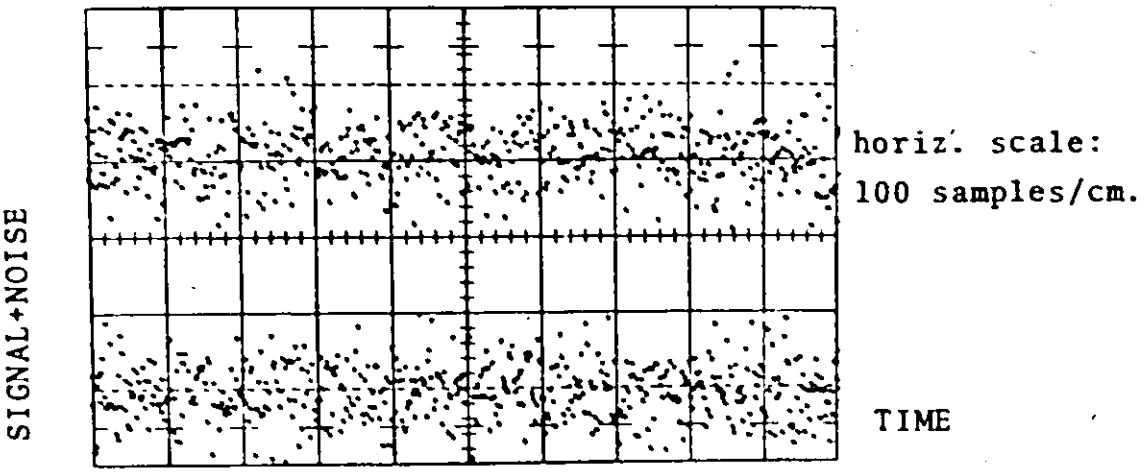

figure 21. Signal Plus Noise for JSNR=2. Real Part Above and Imaginary Part Below.

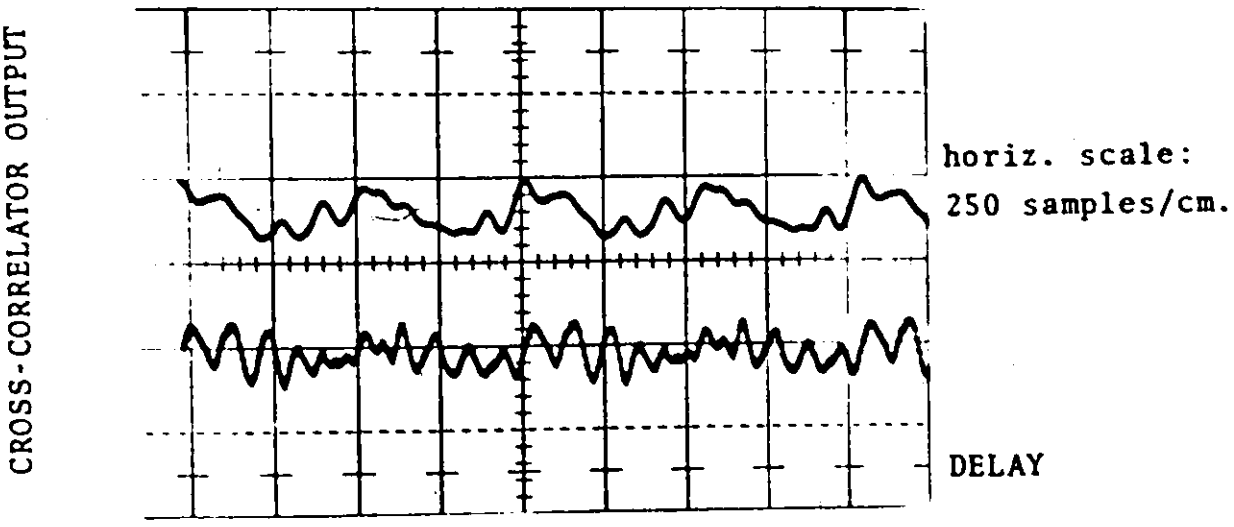

figure 22. The Output of the Cross-Correlator (Upper Curve) and the First Difference of the Cross-Correlator Output for JSNR=2, (Lower Curve).

of the correlator. The simulation of the delay-lock discriminator will be discussed first.

3.7 The Delay-Lock Discriminator

3.7.1 The Delay-Lock Discriminator with No Digital Filter

The simplest delay-lock discriminator tested involves no digital filtering of the FFT cross-correlator output. The performance of this loop was tested by varying the loop gain factor "k" of the system as shown in parts a, b and c of Fig. 23. This loop is clearly not suitable as a tracking device for two reasons, a) it is incapable of reducing the steady state error for a step input of delay to zero and, b) when the loop gain is set at a high value to reduce this error the output begins to hunt.

3.7.2 The Delay-Lock Discriminator with First-Order Digital Filter

The performance of the delay-lock discriminator can be improved by the addition of a first-order digital filter $H(z^{-1})$ that is the digital equivalent of a low-pass RC filter. The inclusion of the filter serves to reduce the delay jitter caused by noise. This digital filter may be obtained by applying the impulse equivalent analog-to-digital transformation [34].

$$\frac{1}{s+p} \Rightarrow \frac{1}{1-e^{-pT}z^{-1}} \quad (0<e^{-pT}<1) \qquad (50)$$

where p is the pole of the Laplace transform of the low-pass RC filter impulse response and T is the period of one iteration in

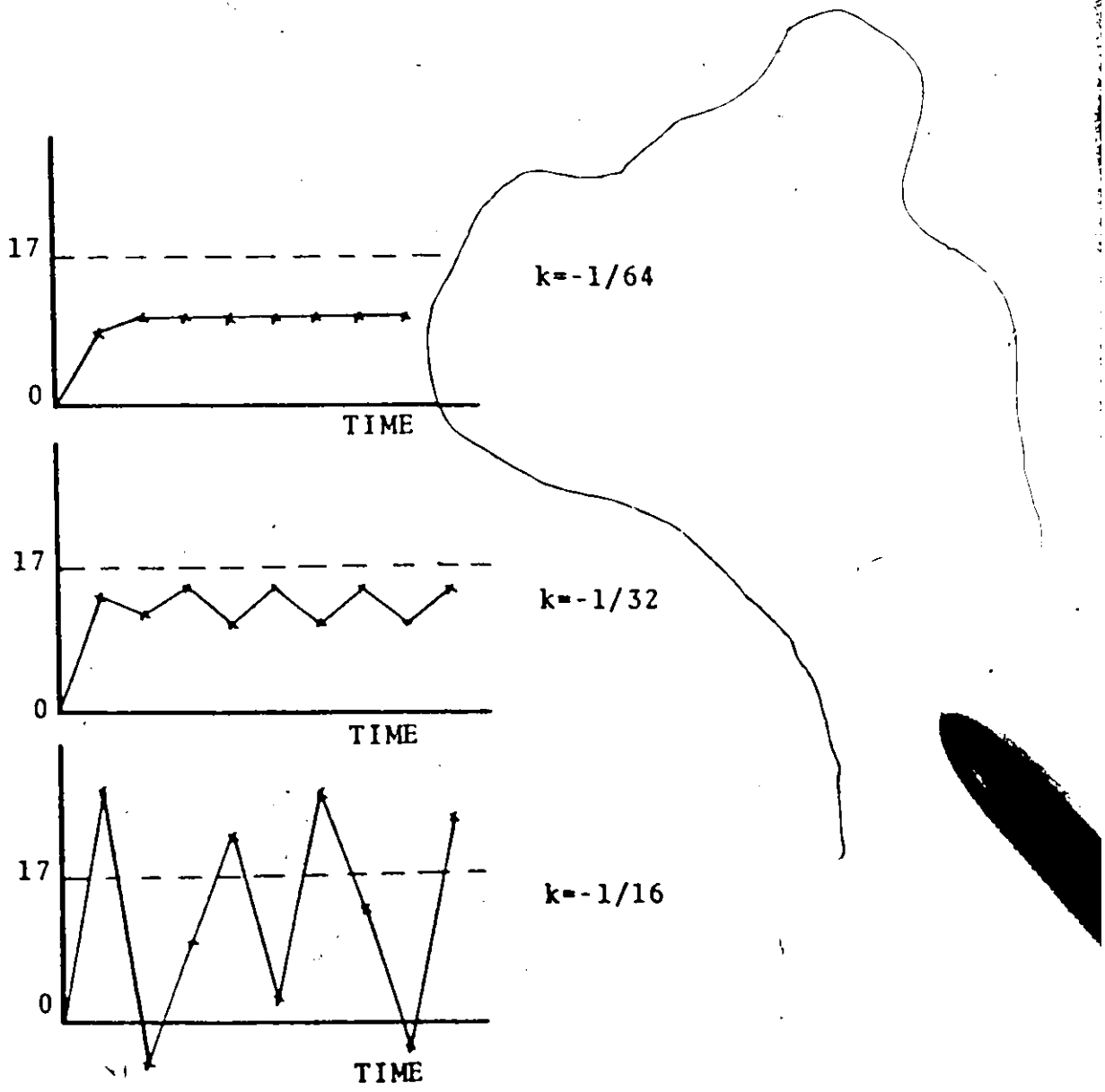

figure 23. Step Response of the Delay-Lock Discriminator with no Digital Filter. The Parameter k Controls the Feedback Gain.

the loop. When the factor e^{-pT} approaches zero the bandwidth of the loop is reduced and delay jitter is reduced at the expense of transient error. When on the other hand e^{-pT} approaches unity the bandwidth of the loop is increased and transient error is reduced at the expense of an increase in delay jitter. The low-pass digital filter obtained in this way is as shown in Fig. 24. Thus the program to represent this digital filtering operation is:

$$JFB_n = e^{-pT} JFB_{n-1} + INPUT_n \qquad (51)$$

Note that according to Fig. 18(a) the INPUT to the digital filter is equal to k.MR(1) where k is the loop gain factor and MR(1) is the central element of the first difference of the correlator output. JFB_n is the digital filter output at time t = nT, and JFB_{n-1} is the past value of the digital filter output (i.e., at t = nT-T).

In Fig. 25, five step responses of the delay-lock discriminator are shown to demonstrate the effect of varying the time constant of the loop, that is e^{-pT}, the loop gain factor k, and the amplitude of the step input of delay. In Fig. 25(a) the response appears rather sluggish with a steady state error; the system settles down at a delay value slightly above the input step amplitude. This effect is caused by the quantization of delay. In Fig. 25(b) leaving e^{-pT} unchanged but increasing the gain results in an oscillating limit cycle. Similarly oscillation is obtained for a slightly different e^{-pT} in Fig. 25(c). In Fig. 25(d) the steady state error of one sample is

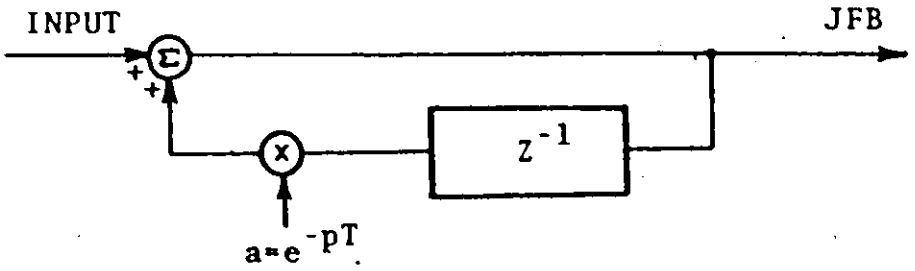

figure 24. A Digital Filter Impulse Equivalent to an RC Analog Low-Pass Filter. The INPUT is Equal to k·MR(1).

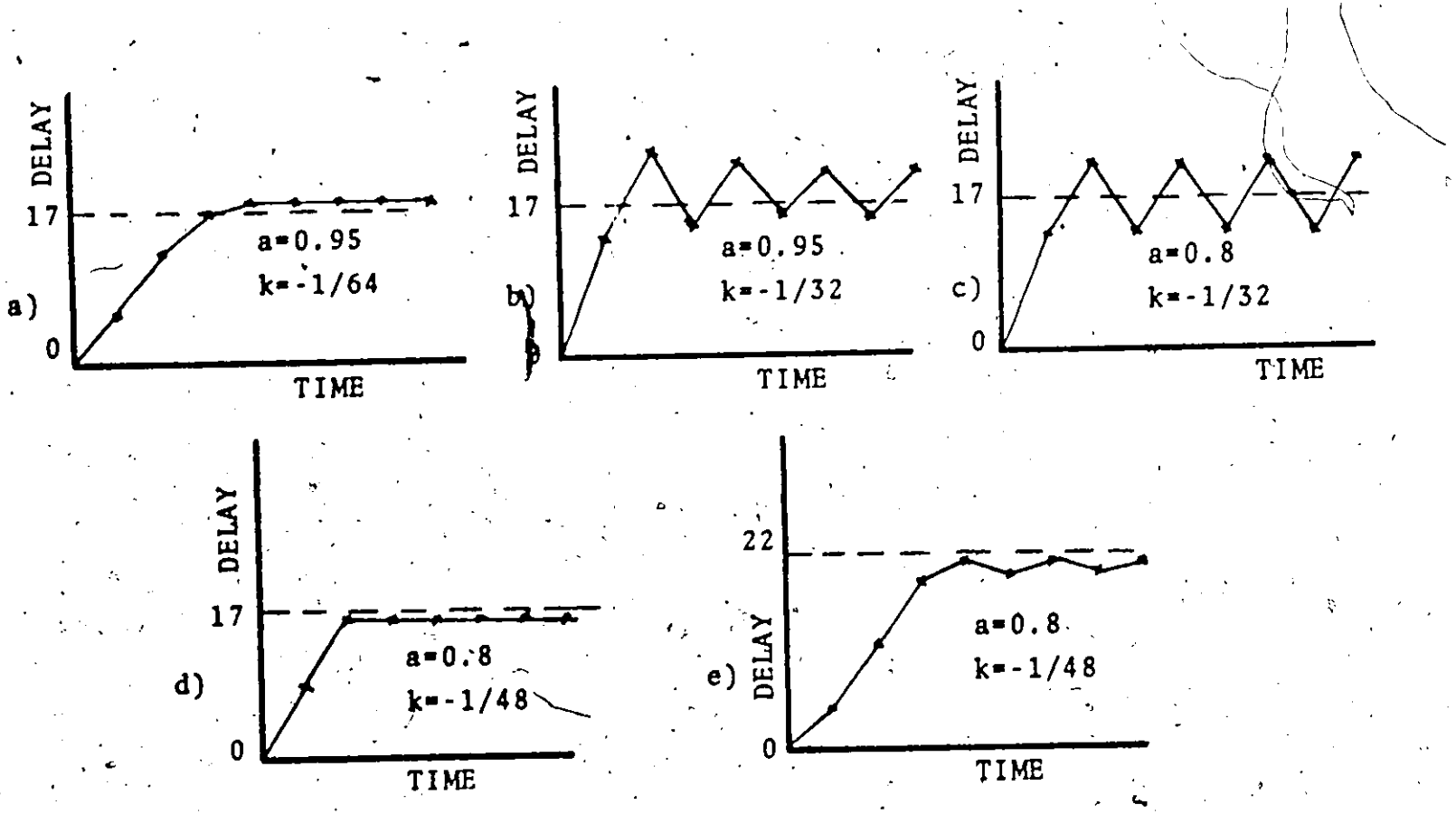

figure 25. Step Response of Delay-Lock Discriminator with First-Order Digital Filter. The Parameter "a" Equals e^{-pT} and Controls the Bandwidth. The Parameter "k" Controls the Loop Gain.

reached in only 2 iterations; however for a larger input step amplitude this is not the case as in Fig. 25(e). Notice in case (e) the slow initial response to the step followed by an increasing response as the final delay is approximated more closely. This is due to the value of the step input of delay being increased so that the error feedback characteristic shown in Fig. 26 is pulled away from the linear central portion.

3.7.3 The Delay-Lock Discriminator with Second-Order Digital Filter

The next version of the delay-lock discriminator investigated used a second order digital filter with a transfer function defined by:

$$H(z^{-1}) = \frac{1}{(1-z^{-1})(1-e^{-pT}z^{-1})} \qquad 0 < e^{-pT} < 1 \qquad (52)$$

The factor $\frac{1}{1-z^{-1}}$ represents the digital equivalent of an ideal integrator; it was included in the loop in order to reduce the steady state error of the loop to zero. As in the previous delay-lock discriminator the digital filter defined by Equation (52) contains the factor $\frac{1}{1-e^{-pT}z^{-1}}$ which is the impulse equivalent of an RC low-pass filter, included in order to reduce the delay jitter caused by noise. The block diagram of the digital filter defined by Equation (52) is shown in Fig. 27.

The delay-lock discriminator and the decision-directed loop are intended to operate simultaneously to compare their

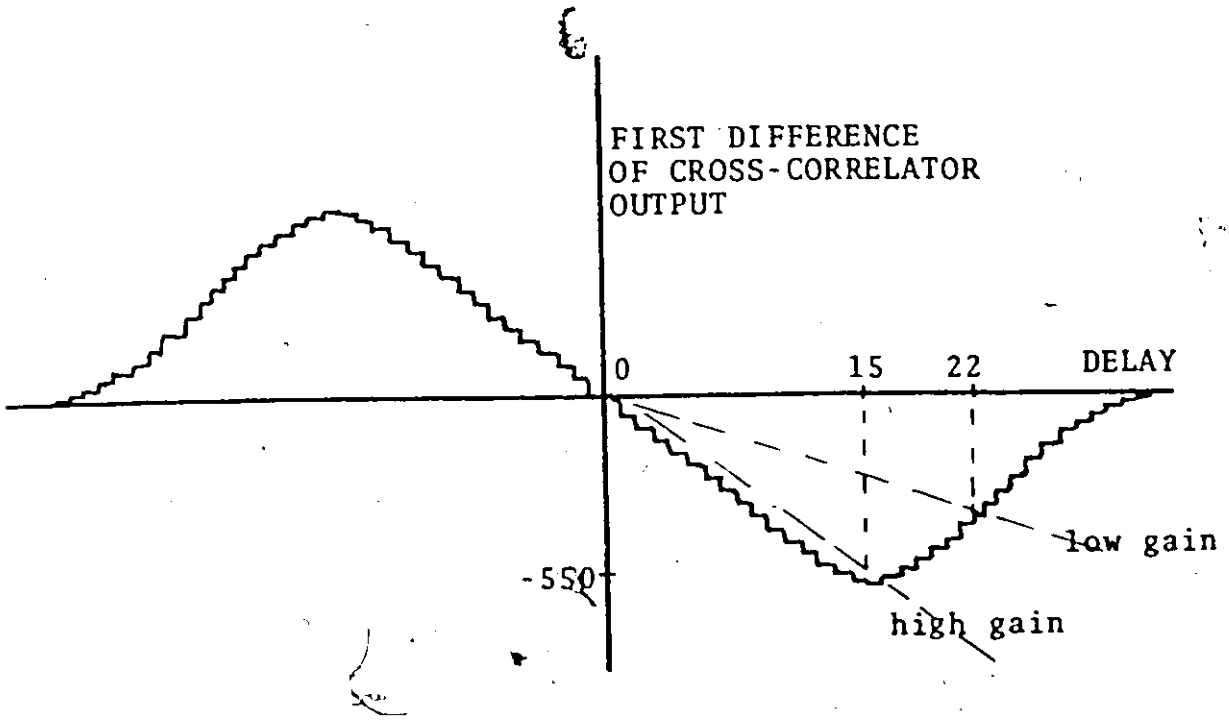

figure 26. Error Feedback Characteristic of the Delay-Lock Discriminator. The Delay Input is Measured in Samples Showing the Nonlinearity Caused by a Large Input.

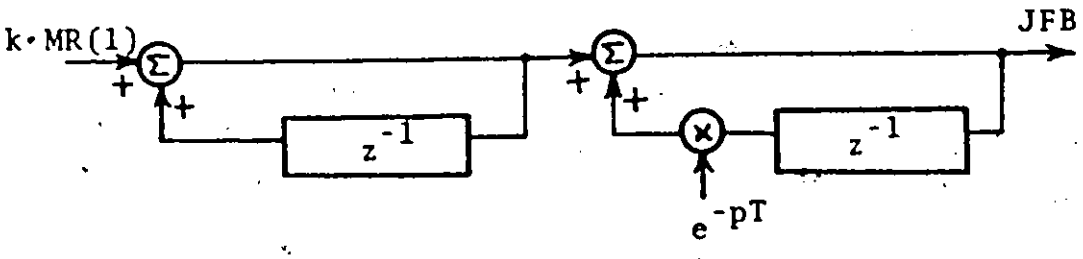

figure 27. The Second-Order Digital Filter for the Delay-Lock Discriminator.

performance at high and low signal-to-noise ratios. However a meaningful comparison of the performance of the two devices for a given input of delay (step input, for example) can only be made if the delay-lock discriminator is operating in an optimum fashion for that input. The error characteristic of the delay-lock discriminator is nonlinear as shown in Fig. 26. Accordingly the delay-lock discriminator using the second-order digital filter of Fig. 27 was optimized for a step input of 20 delay samples by means of computer simulation. Specifically the mean squared error for the delay step over 20 iterations was minimized by varying the loop gain factor k and the exponential factor e^{-pT} for a signal-to-noise ratio JSNR = 2. The value of e^{-pT} thus determined was found to be $e^{-pT} = 0.2$ and the value of the loop filter factor k was found to be $k = -1/28$. The step response of the optimized delay-lock discriminator with second-order filter will be shown in Chapter 4.

3.8 The Decision-Directed Delay-Lock Loop

In this section the statistical distributions of the target and the noise at the output of the FFT correlator are shown. The decisions of the decision-directed loop are based on the calculation of the distribution of the target range posterior probability. The decision process was successively refined to allow consideration of up to three possible target ranges as indicated by the three largest peaks of the correlator output.

3.8.1 FFT Correlator Output Statistical Distribution

The FFT correlator performs circular cross-correlation on two segments of 1024 samples of the two input sequences, the replica and the target echo plus noise respectively. The amplitude statistics of the signal function and the noise function at the correlator output were measured so that the feedback for the decision-directed loop could be determined in an optimum manner. The two 1024 sample segments of echo and replica were chosen from the signal record stored on the disk storage. The fraction of 1024 samples which are identical in both segments determines the fractional overlap between the echo and the replica. The remaining fraction which is not coincident in the two segments is called the offset.

The target echo amplitude after circular cross-correlation is equal to the value of the target function peak. This signal peak is located away from the origin of the range axis at the correlator output by an amount equal to the offset. As the overlap decreases the target peak amplitude decreases in a linear fashion. A large number of peak values of a single target were computed for different amounts of overlap from 100 to 50 percent, as shown in Fig. 28. We can see that the peak value and the overlap are directly proportional to each other. This is to be expected from any echo which is coherent with the replica. The proportional linear curve shown in Fig. 28 extends to the origin of delay at zero overlap. Two periods of the circular correlation are shown in Fig. 29. Both periods are identical and they serve to illustrate range ambiguity.

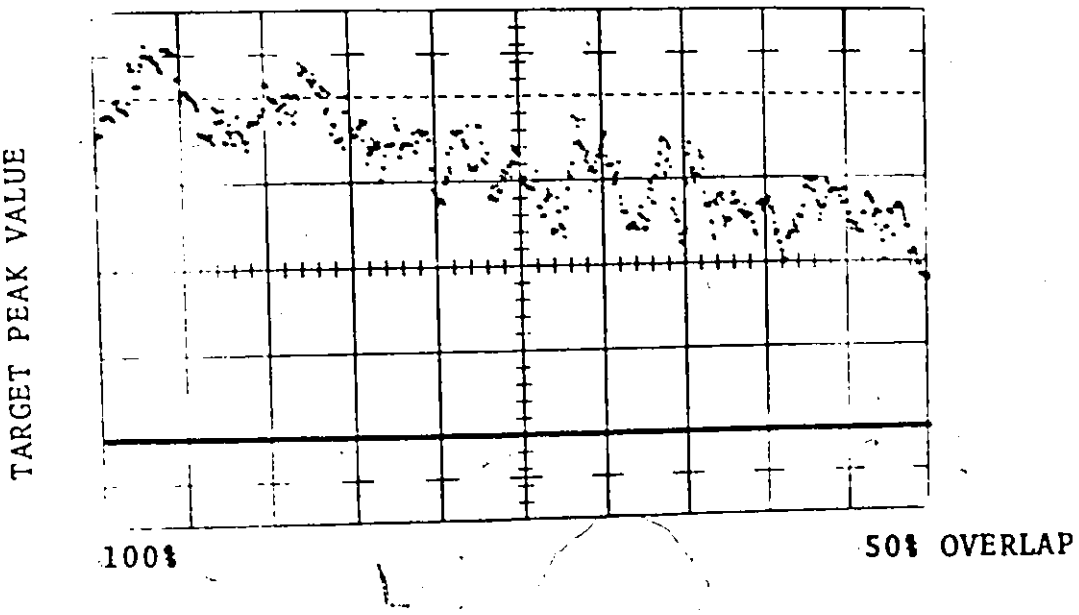

figure 28. Amplitude of Target Peak Versus Overlap.

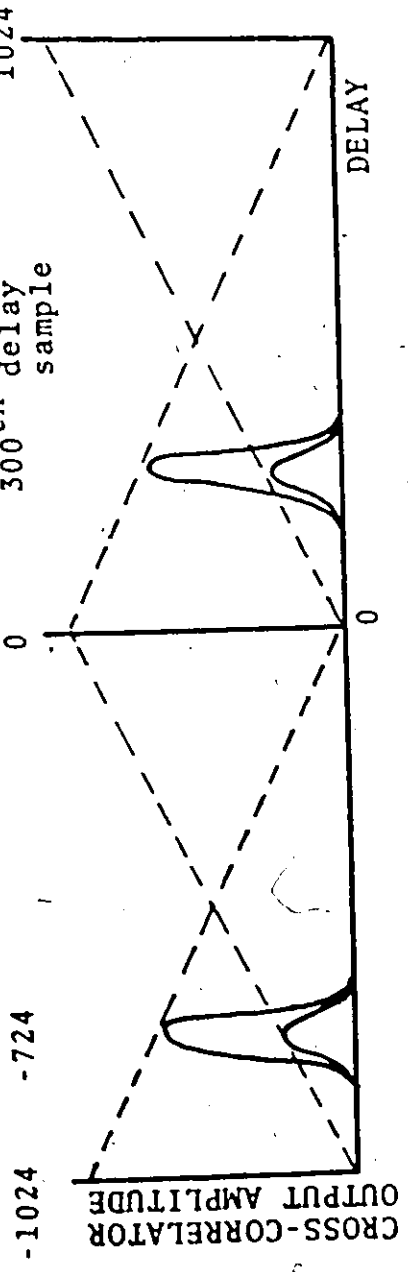

figure 29. FFT Circular Cross-Correlator Output Illustrating Range Ambiguity.

If in Fig. 29 we observe a target peak at the 300th positive delay sample we cannot be sure that it may not be due to a negative offset of 724 delay samples. The only means of resolving this ambiguity is to observe the target peak amplitude as the replica delay is altered. If the replica delay is increased by 300 samples either the target peak will be maximized or the target will disappear. If the target peak disappears the correct offset was previously - 1024 + 300 = 724 delay samples. This ambiguity is not a problem if the observations of target peaks are made near the delay origin in the center of Fig. 29. At this location nearly all the targets observed will have near zero offset as the amplitude of the ambiguous targets is very small.

The target peak value for zero offset is not constant however because of the statistical variation in the energy of the low-pass random signal. In Fig. 30 the cummulative distribution of target peak value is shown for zero and 500 sample offsets. An error function equal to the integral of a Gaussian curve can be fitted to the target peak amplitude cummulative distribution. From this fitted curve the mean value of the target peak for zero offset is 1500 and the standard deviation is 400 at JSNR = 10. Similarly for an offset of 500 delay samples the mean is 750 and the standard deviation is 330. From this we conclude that the mean value is proportional to the offset and that the variance is also proportional to the offset, for zero input noise.

The cummulative distribution of the noise is shown in

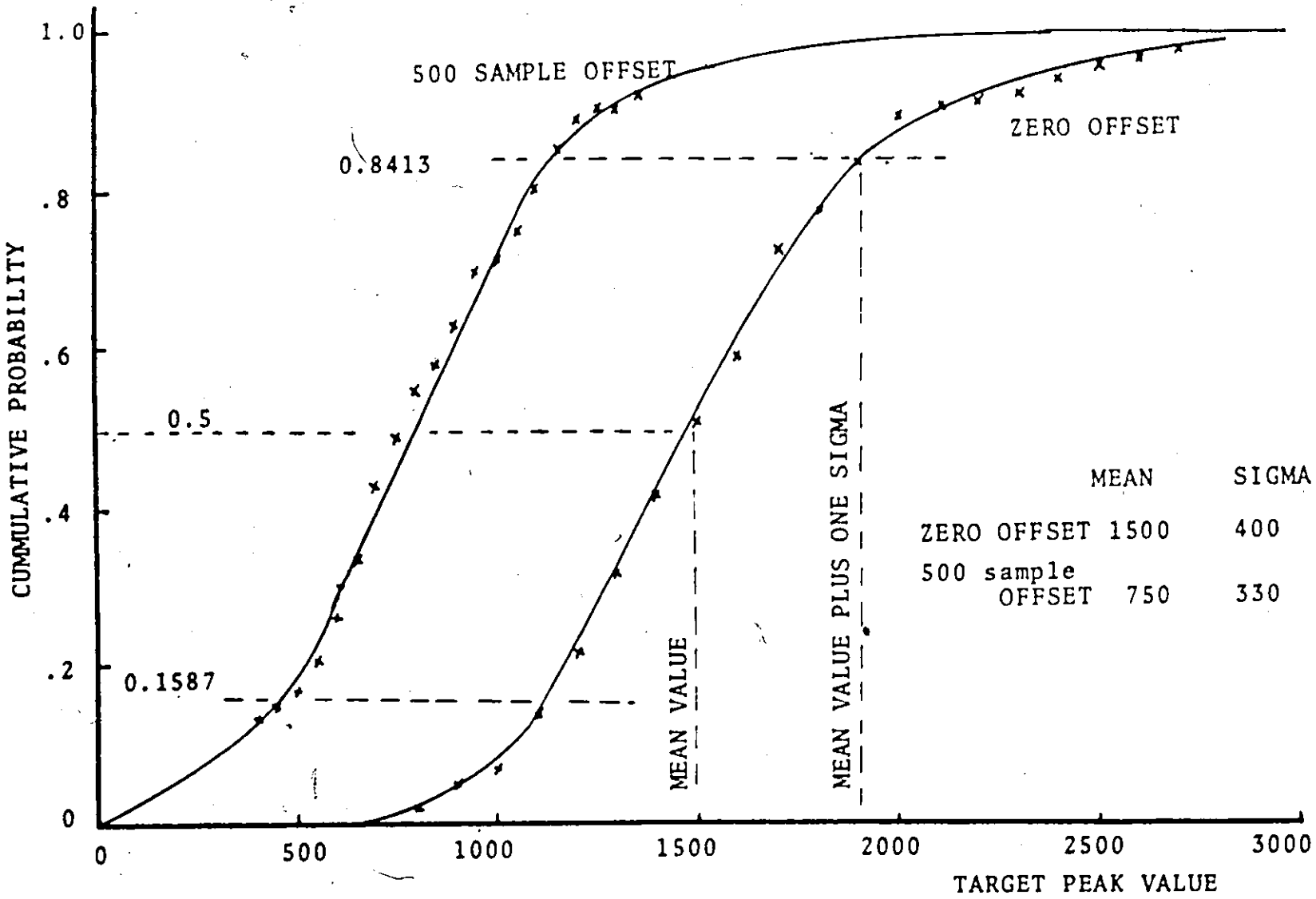

figure 30. The Cummulative Probability of the Target Peak at the Cross-Correlator Output for Zero and 500 Sample Offsets.

Fig. 31 for several values of JSNR. The distribution of the noise fits a Gaussian curve with a mean slightly greater than zero and a variance which increases with decreasing JSNR. The fact that the supposedly zero-mean noise has a slightly positive mean can be attributed to an asymmetry in the analog input noise used to generate the signal and the noise. However since this asymmetry exists in both the desired target signal and the input noise, the effect of the asymmetry may be neglected.

The distribution density of the target peak and the noise is shown in Fig. 32. If we desire to detect the target peak on the basis that it exceeds the noise we might set up a threshold which the target peak nearly always exceeds and the noise seldom exceeds. In a surveillance radar a very low probability of false alarm is desireable which would imply a high threshold. However in a tracking radar range loop the signal-to-noise ratio may be low and the system has the ability to track the target range even with the occasional range error; thus in the decision-directed loop a very low threshold can be tolerated and any noise peaks which exceed the threshold and the target peak may be rejected by the decision process. The decision process and the number of times noise generates false alarms is discussed in the section on posterior probability which follows.

3.8.2 The Calculation of the Posterior Probability of Delay

In this section the relation between the signal-to-noise ratio, JSNR, and the correlator output peak energy to noise

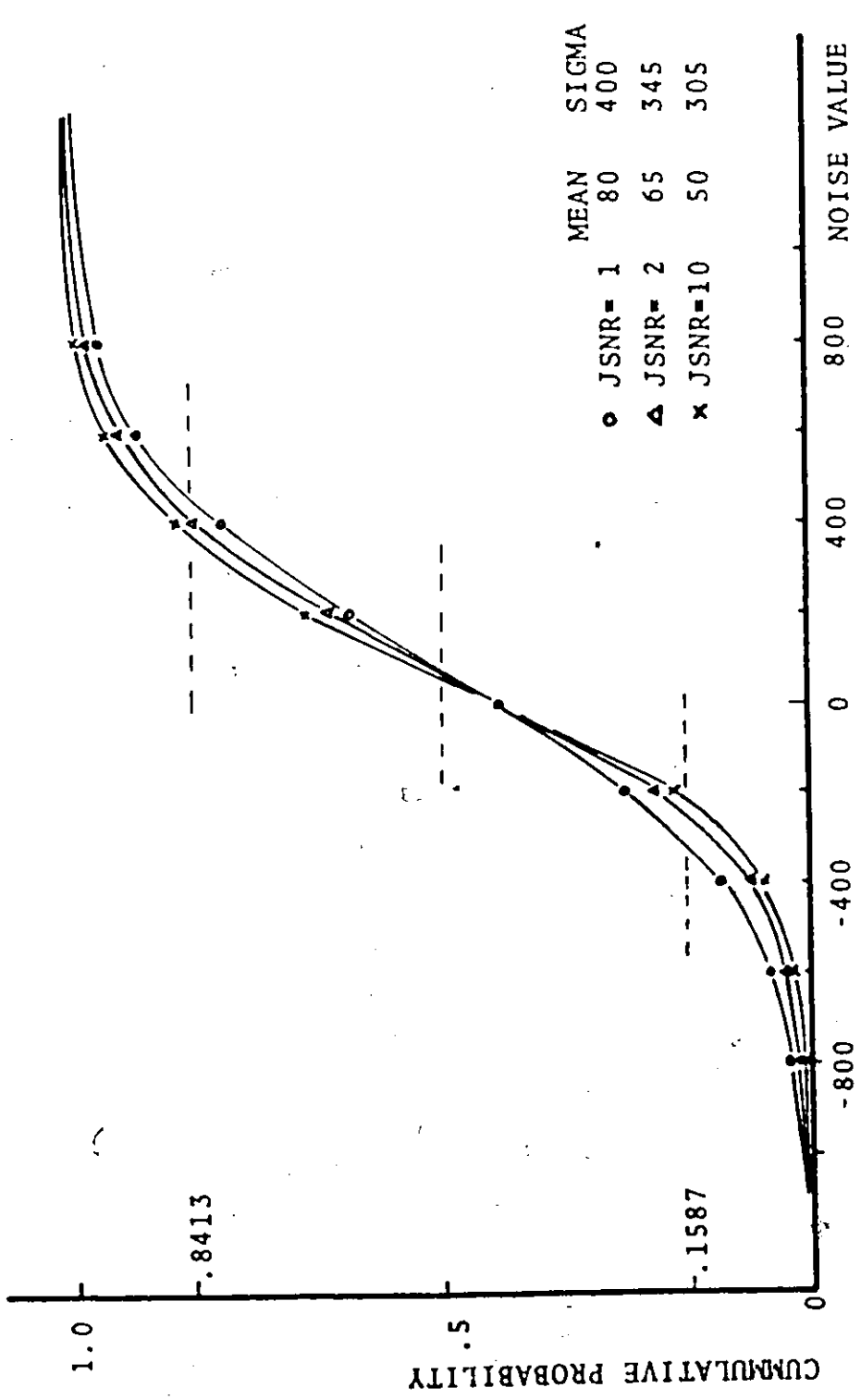

figure 31. The Cummulative Probability Distribution of the Noise Function. Sigma is the Standard Deviation of the Noise which is Equal to the Value at a Probability .8413 Minus the Mean.

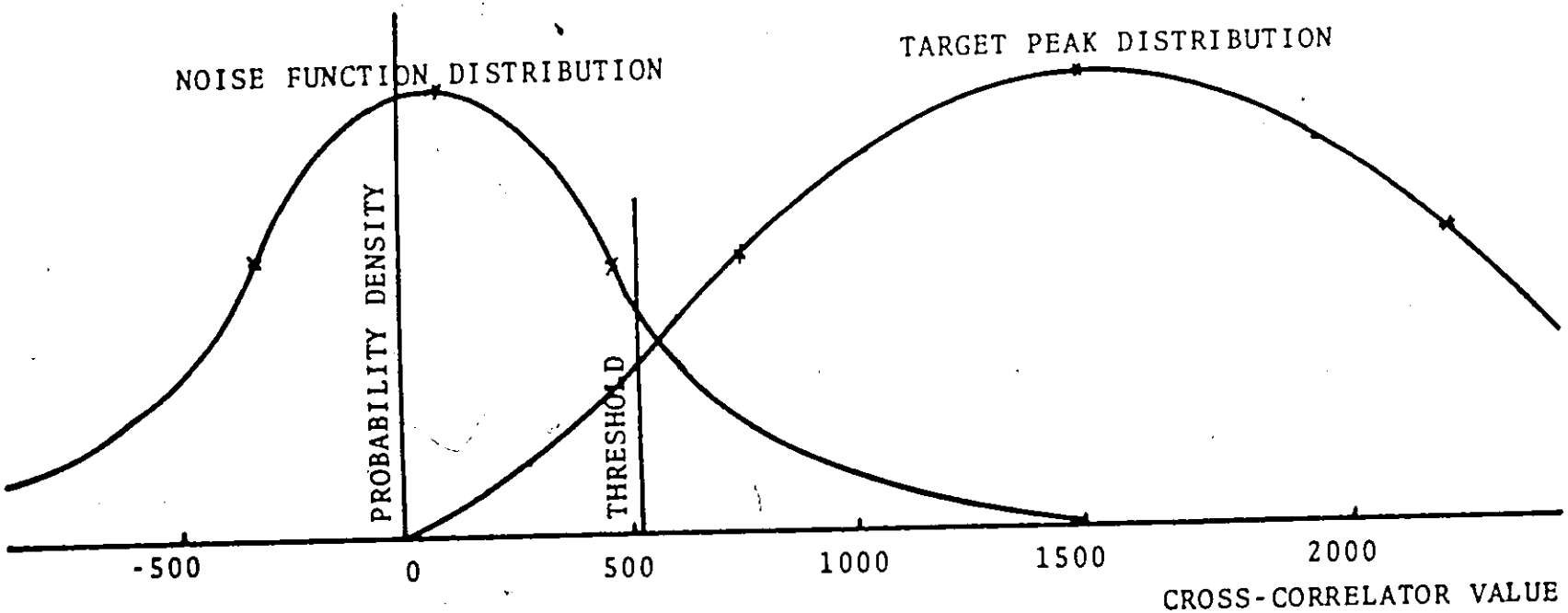

figure 32. The Probability Density of the Target Peak and the Noise Function at the Cross-Correlator Output for JSNR=1, Showing the Threshold.

function energy ratio R is shown. The dependence of R on offset is also calculated. From Woodward's theory of delay measurement the optimum decision policy is to compute the posterior distribution of the range probability and make a decision based on this information.

The relation betwen R and JSNR was obtained by computing a large number of target outputs for zero offset, with different values of signal-to-noise ratio controlled by the integer factor JSNR which divides the noise spectrum in Fig. 19. The square of the target peak was divided by the mean square noise function to obtain R. A calibration curve which will be useful to explain the results is shown in Fig. 33. R is also equal to $2E/N_o$ from Equation (19) where E is the total signal energy and $N_o/2$ is the noise energy per sample. Theoretical points calculated from Equation (19) and Equation (36) are also shown. We can see that as JSNR increases the value of R is bounded above by the self-noise produced by the random low-pass signal. For an infinite period of integration we would expect R to be proportional to the square of JSNR since the energy of the noise is proportional to $JSNR^2$. However the finite FFT integration which only sums 1024 sample products causes R to saturate very quickly. By combining several correlator outputs a larger effective value of R may be produced. Values of R below five were not measured as these values do not allow a delay-lock loop to remain in lock unless extremely long time-averaging was used inside the loop.

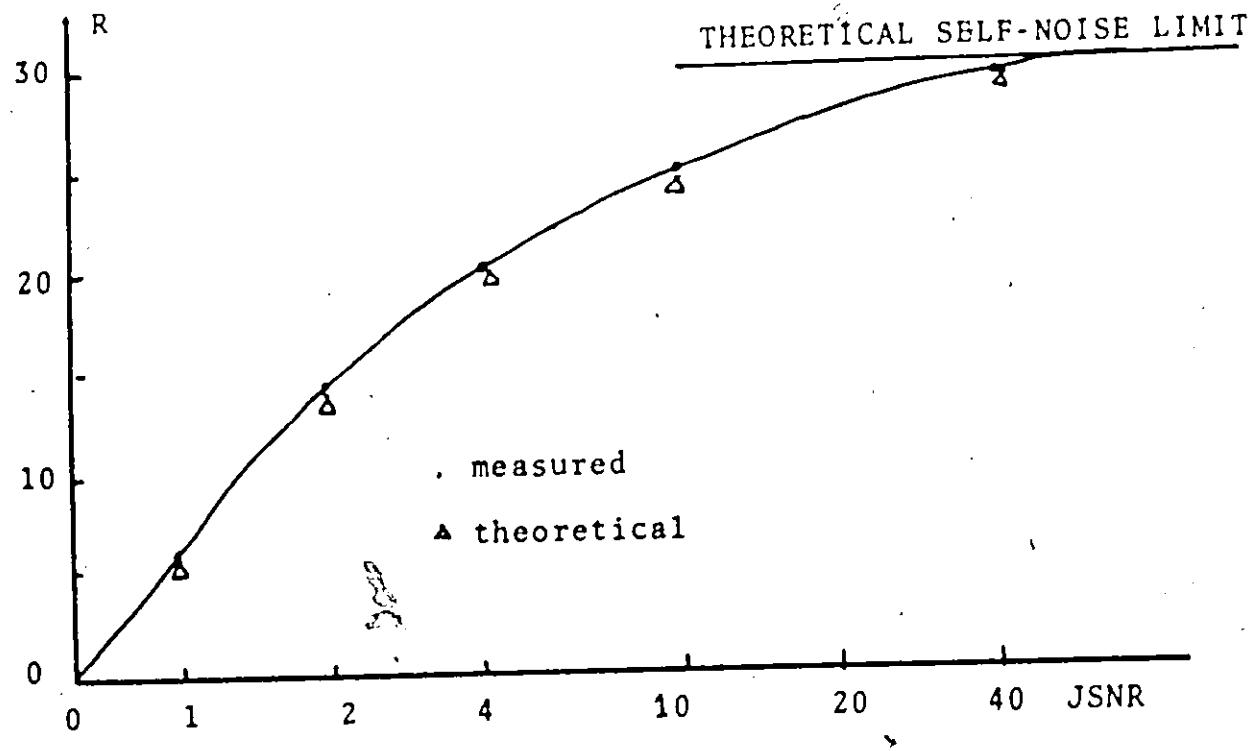

figure 33. The Signal-to-Noise Ratio Calibration Curve R versus JSNR Showing the Theoretical Limit of R Equation (36).

The value of R is also proportional to the square of the fractional overlap. The noise function and self-noise energy are independent of the overlap but the target amplitude is proportional to the overlap.

The dependence of R on JSNR and overlap indicates the information about range per correlation depends on these factors.

The calculation of the posterior probability of target delay $p_y(\tau)$ is made after the correlator output and is based on that output and the prior probability of delay as in Equation (14) which is repeated here.

$$p_y(\tau) = kp(\tau) \exp \{q(\tau)\} \tag{53}$$

where $p(\tau)$ is the prior delay probability and $q(\tau)$ is the correlator output.

The "largest of" detector of the decision-directed loop operates by choosing the delay of the largest value of $p_y(\tau)$ as the correct target delay. There are two cases to consider depending on the value of R. If R is below the "threshold of intelligibility" given by Equation (21) then the posterior probability is ambiguous and no decision is possible without a high probability of a serious error. This case is not considered suitable for the decision-directed loop. The critical value of $R = R_t$ for this threshold is:

$$R_t = 2 \ln R_t \tau \beta = 2 \ln 30 + 2 \ln R_t \qquad (54)$$

$$R_t = 11.726$$

The second case where $R > R_t$ allows decisions to be made at the rate of one per correlator iteration, and is the case which will be discussed in what follows.

In the calculation of $p_y(\tau)$ using Equation (53) it is not necessary to exponentiate the correlator output $q(\tau)$ if we rewrite Equation (53) by taking the natural logarithm of both sides.

$$\ln p_y(\tau) = q(\tau) + \ln p(\tau) + \ln k \qquad (55)$$

Since the natural logarithm is a monotonic function the most probable value of delay can be found by choosing the largest value of the left hand side of Equation (55). If the prior delay probability is flat (i.e., constant) or varies slowly over the range of delay of interest then we may approximate the maximum value of $\ln p_y(\tau)$ by picking the largest value of $q(\tau)$. This was done in the decision-directed loop to simplify the calculation of the most probable delay.

At low values of R the probability of making a decision error is related to the probability that the noise function exceeds the signal function. Since $\sqrt{R}$ is the peak of RMS ratio of the signal function to noise function at the correlator output we may calculate the number of times signal exceeds noise as a function of R by assuming the noise function to have a

Gaussian amplitude distribution. From Fig. 34 the value of R below which most of the decisions will be in error is R = 4. We conclude therefore from the calibration of R versus JSNR Fig. 33 that operation of the loop below JSNR = 1 will be erratic.

3.8.3 Refinement of the Decision-Directed Loop

The decision-directed loop was refined by a series of stages which are reported here to show the types of undesireable responses which occur when the decision process is in error.

The first decision feedback was based on detecting the largest peak of the correlator output and from its position on the delay axis the delay jump to synchronize the replica with the target echo was determined. Such a system would be dead-beat in one iteration independent of the size of the input delay error as long as the overlap between target and replica was not initially zero. For this decision process the prior delay probability was constant.

The input delay was set to stay constant for 5 iterations, to step up by 20 delay samples on the sixth iteration and to step down on the 16^{th} iteration to the former value. Such a test delay input allows both jitter and transient response to be tested. The decision-directed delay-lock loop and the delay-lock discriminator which ran simultaneously are shown in Fig. 18(c). The low-pass digital filter incorporated into the delay-lock discriminator is shown in Fig. 27. The response to the delay input of each loop is shown in Fig. 35(a) for JSNR = 18

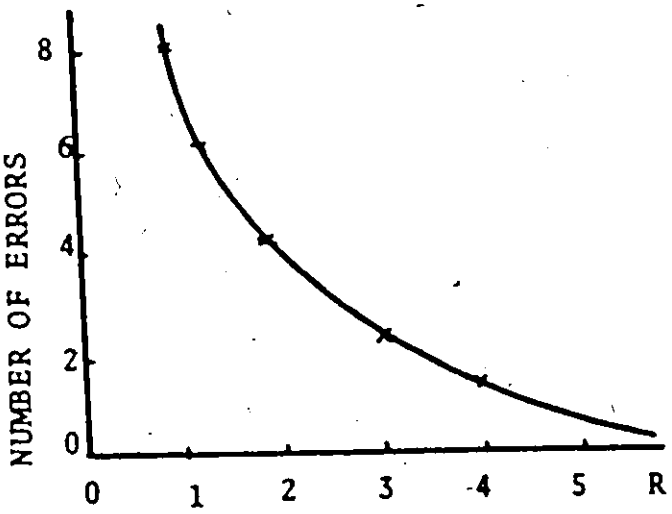

figure 34. Number of Times Per Iteration that Noise Exceeds Signal at the Cross-Correlator Output.

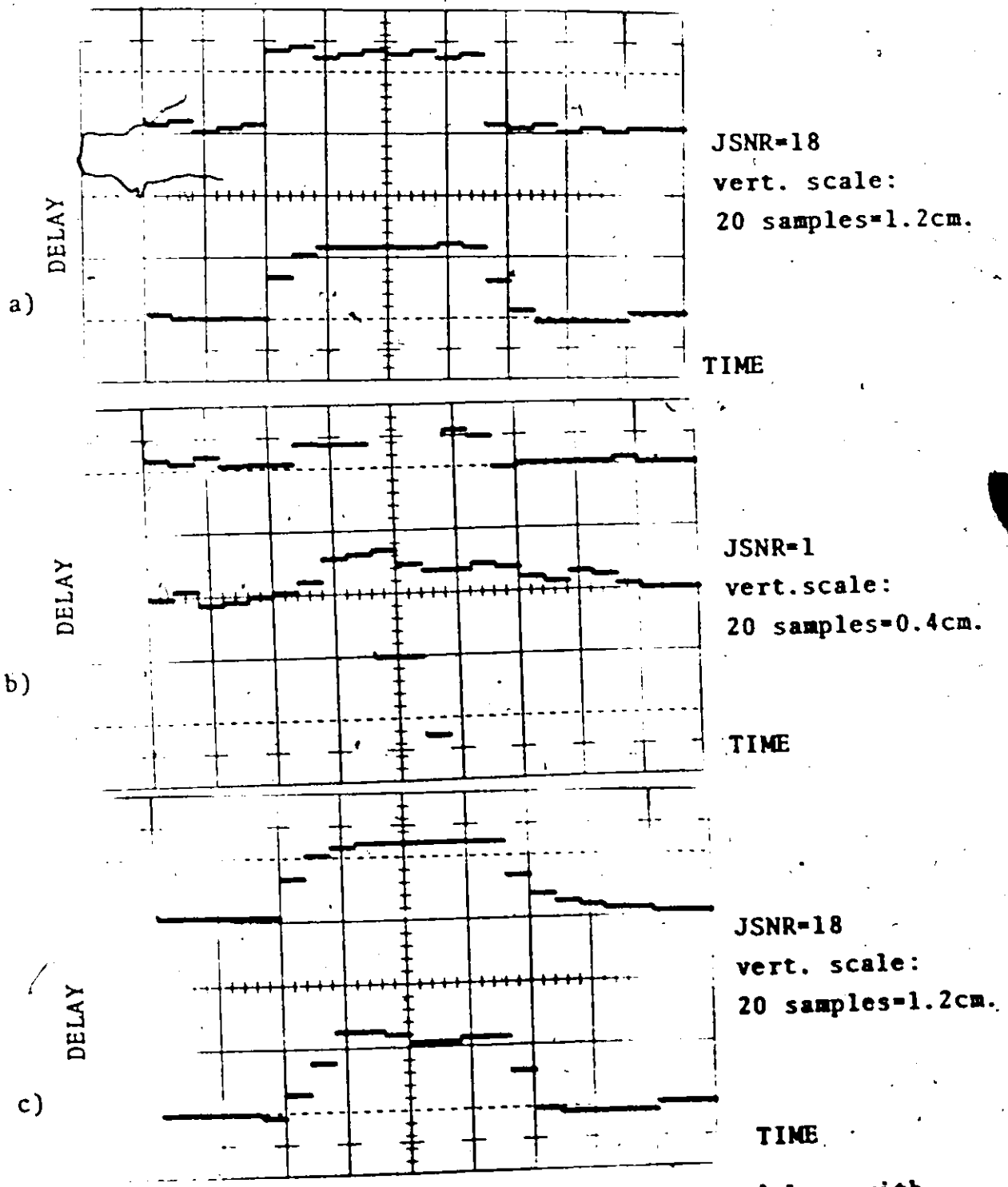

figure 35. Step Response of the Decision-Directed Loop with " One Largest " Detector (Upper Trace) and Response of the Delay-Lock Discriminator (Lower Trace). a)Direct Feedback b)Direct Feedback c) Decision Feedback Multiplied by 1/2.

and Fig. 35(b) for JSNR = 1.

At high signal-to-noise ratio the response to the decision-directed loop is dead-beat in one iteration as expected and the response is much faster than that of the delay-lock discriminator but at low signal-to-noise ratio the decision-directed loop makes occasional intolerable errors and behaves very erratically. One possible remedy is to reduce the loop gain of the decision-directed loop by a factor greater than one as shown in Fig. 35(c). However the decision-directed loop is now slower in its response although the errors are only half as bad. Obviously this is only a temporary solution.

The answer to improving the operation of the decision-directed loop lies in making use of prior range information as obtained from the previous iteration. At low signal-to-noise ratio peaks at the correlator output may exceed the target peak. The false targets which appear due to the noise may be rejected on the basis of prior target range probability. The noise peaks will betray their nature by occurring at random over the delay range while the target may appear several times in succession near the same range.

However if we pick only "one largest" at each iteration then at low signal-to-noise ratio, R equal to or less than 4, this one largest in some cases will be a noise peak. The answer to this problem lies in picking two or even three peaks at each iteration and calculating their posterior probability of being the target.

For the system which picks "two largest" the calculation of the maximum posterior probability proceeds as follows. First in the range of interest at the correlator output, where the offsets being considered are say, -512 delay samples to 512 delay samples, the two largest correlator peaks are chosen. These peaks are at, say, τ_1 and τ_2. Then from Equation (55) we may write:

$$\ln p_y(\tau_1) = q(\tau_1) + \ln p(\tau_1) + \ln k \tag{56}$$

$$\ln p_y(\tau_2) = q(\tau_2) + \ln p(\tau_2) + \ln k \tag{57}$$

The most probable target delay is chosen from the largest of either:

$$q(\tau_1) + \ln p(\tau_1) \gtrless q(\tau_2) + \ln p(\tau_2) \tag{58}$$

Therefore we record $q(\tau_1)$ and $q(\tau_2)$ as the largest correlator outputs and weight them by adding $\ln p(\tau_1)$ and $\ln p(\tau_2)$ respectively, where $p(\tau_1)$ and $p(\tau_2)$ are the prior probabilities of the target delay. If the target is assumed to be tracked by the decision-directed loop then the overlap is likely to be almost 100%. As an example assume a Gaussian probability of target delay centered at the same delay as the replica, so that:

$$p(\tau) = \exp\left(\frac{-|\tau|^2}{5000}\right) \tag{59}$$

where the standard deviation of the prior target delay is 50. This sets an allowable range of delays over which the target may appear on each iteration. If this deviation is made too

small the target will be lost if its delay changes suddenly. Substituting Equation (59) into Equation (58) we get

$$q(\tau_1) - \frac{|\tau_1|^2}{5000} \lesssim q(\tau_2) - \frac{|\tau_2|^2}{5000} \qquad (60)$$

Equation (60) sets the weights which are added to the correlator outputs $q(\tau_1)$ and $q(\tau_2)$. From an examination of Fig. 34 for the number of times on the average that noise exceeds the signal peak we can see that the method of Equation (60) will fail with a high probability for values of R less than R = 3.

A further refinement is to extend the method to "three largest" peaks. This will allow the value of R to fall as low as R = 2.5. The extension to four or more possible targets is obvious but from the steep increase in the probability of an error as shown in Fig. 34 for R < 3 the point of diminishing returns is rapidly reached. Therefore we will limit the final refinement to include the calculation of the posterior probability of three largest correlator peaks.

3.8.4 The Decision-Directed Loop with the "Three Largest" Peak Detector

In the block diagram of Fig. 36 a decision-directed delay tracking loop using a "three largest" peaks detector is shown. This detector operates by choosing one largest peak and then blanking out that region of the correlator output with zeros and then chooses the next largest from the non-zero samples remaining. After zeroing out the second largest peak the third largest is chosen. This method avoids picking all three largest

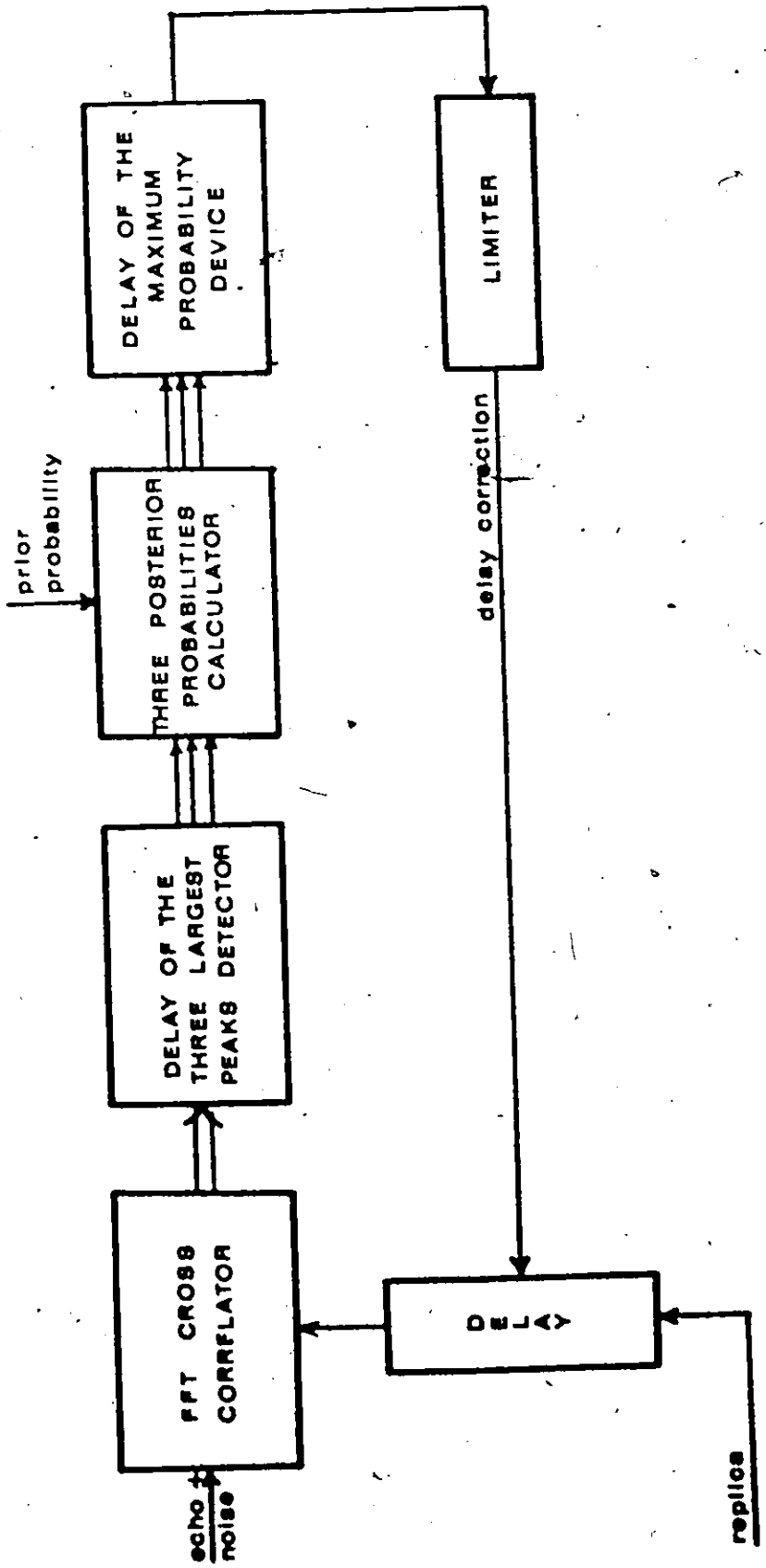

figure 36. A Decision-Directed Delay Tracking Loop using a Three Largest Peaks Detector.

samples at the same delay. The three delay values corresponding to the three largest peaks are next passed to the posterior probability calculator where the delays are assigned probabilities based on their location with respect to the last position of the target. The "maximum posterior" probability device chooses the most probable delay correction required to attain 100% overlap between the stored replica and the received echo. Finally the limiter is included to prevent large errors which may occur if all the three largest correlator peaks were due to noise and the signal went undetected.

In the next chapter of this thesis three modes of operation of the loop are studied namely acquisition, tracking and unlocking.

Chapter 4

Acquisition, Tracking and Unlocking

In this chapter the experiments using a decision-directed delay-lock will be detailed. The study of the operation of the loop is divided into four parts. The first set of experiments deals with acquisition of a stationary target of unknown range, by a gross search over all possible range elements starting from the shortest range and working outwards by constant increments. The second set of experiments measures the total square error (TSE) while tracking the delay of a target which executes a small step in range; the TSE of the decision-directed loop is compared with that of the delay-lock discriminator. In the third set of experiments, the unlocking of the decision-directed loop is detected, and the mean time to unlock is measured. Fourthly, the operation of an automatic multimode loop is described in which the modes of acquisition, tracking, unlocking and mode switching to reacquisition are combined. At the end of the chapter the important results of these experiments are summarised.

4.1 Acquisition of a Target of Unknown Range

The object of this part of the study was to locate the delay of a constant amplitude echo of unknown range in the presence of thermal noise. The intention was to find the minimum time required to positively acquire the target range for

different signal-to-noise ratios.

Since the target range is unknown the "a priori" target range probability is flat and constant over the total possible target delays. Hence the only information about the target range appeared at the correlator output in the form of large target peaks which occurred repeatedly at the same absolute range during the acquisition sweep through all possible ranges. The delay of the replica was advanced by equal increments and the absolute range of possible targets was recorded. Let us examine the probability of a target exceeding the correlator output threshold. Since we do not know the range of the target it is not likely that the replica section chosen from the stored signal will overlap the incoming echo completely. Therefore the target amplitude may be reduced by an offset between the two cross-correlator input sample batches. In Fig. 37 the correlator output is graphed for JSNR = 10 showing the mean target output peak amplitude for varying amounts of overlap. Two periods of the circular cross-correlator output are shown although they are identical. The threshold has been positioned to split the target amplitude distribution and the noise amplitude distribution so that the probability of a target miss equals the probability that noise exceeds the threshold. This threshold was picked from the cummulative target and noise distributions measured. Notice that as the target peak amplitude decreases near 50% overlap the threshold dips also. The noise however is constant in energy over the whole possible range, thus more noise peaks may cross the threshold in this area.

These additional false alarms must be tolerated to insure picking up the target as quickly as possible as it moves into coincidence with the replica.

In Fig. 37 we can see that in the delay "interval of interest" where the delay relative to the replica is $\pm$ 512 samples, for a 1024 sample cross-correlator, the target amplitude is above the threshold and above the noise. Ambiguous target range indications will not be a problem in that they are below the threshold and tend to disappear at the point where true range indications are strongest, i.e., at the origin in Fig. 37. Fig. 38 shows a stationary target as it appears at the correlator output when the replica delay is advanced by a constant number of delay samples on three successive correlator iterations. In Fig. 38 (a) the target appears on the right. In Fig. 38(b) the replica delay has advanced by JS = 250 delay samples and target amplitude is enhanced as the target echo and the replica signal overlap. In Fig. 38 (c) the target appears on the left as the replica delay advances a further 250 samples. Thus the three parts of Fig. 38 indicate that a stationary target was observed three times at the same absolute range.

4.1.1 "Three Largest" Detection and Acquisition of Stationary Targets by Two Observations at the Same Range

A gross search was made for stationary targets between 3000 and 6000 delay samples. A single target was placed at 5000 delay samples and the replica delay was advanced by 250 samples per iteration, starting from 3000 units. The object was to acquire the target delay as quickly as possible so as to minimize the time of acquisition at each signal-to-noise ratio.

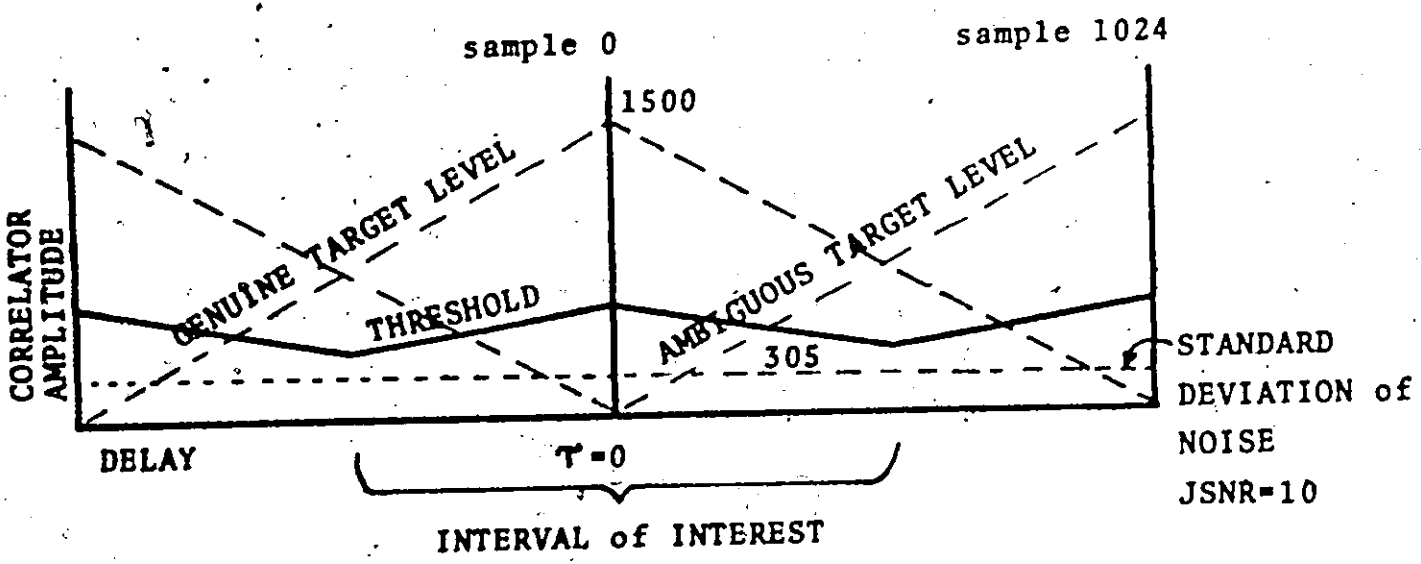

figure 37. The Output of the Circular Cross-Correlator Showing the Threshold and the Ambiguous Target Level. The Interval of Interest extends ±512 Samples about the Origin.

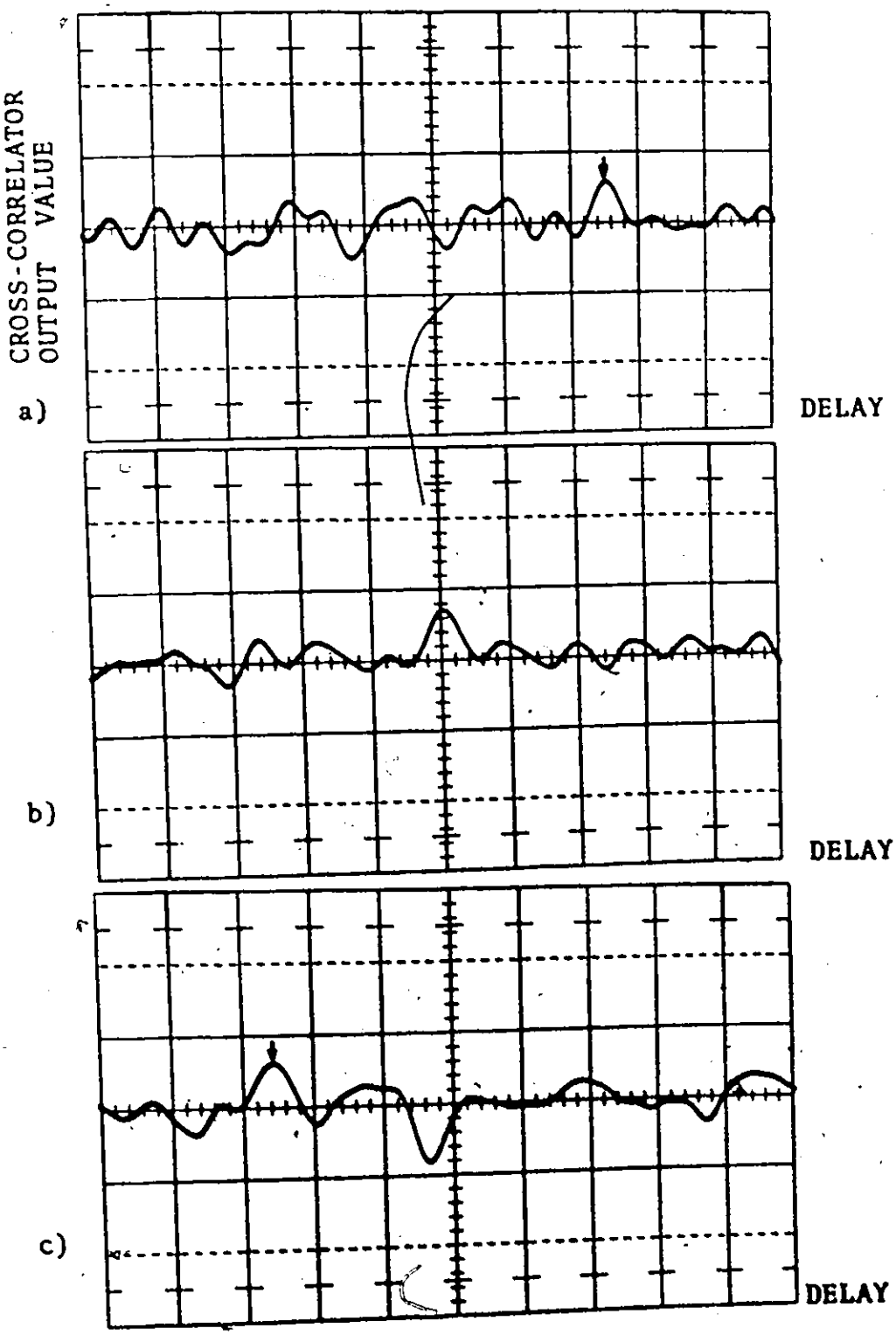

figure 38. Target Moves Right to Left 250 Samples per Iteration During Acquisition. Horizontal Scale 100 Samples per Centimeter.

To assist in making decisions about target and noise peaks at the correlator output a three element array was set up. After one iteration the largest peaks exceeding the threshold up to three in number (or as little as none if the threshold was not exceeded) had their absolute ranges stored in the array. On the next iteration up to three largest peaks were chosen again and their absolute ranges compared with the previously stored ranges at which "hits" had occurred. When a near coincidence of absolute ranges occurred on two successive iterations an acquisition was declared. Allowance was made for delay jitter by calling any two absolute ranges within 20 delay units a coincidence.

With the signal-to-noise parameter JSNR equal to 4 and JS, the replica delay increment equal to 250 the results were as follows. Out of 50 acquisitions, 12 produced the wrong target range and 38 produced 5000 ± 3. Thus approximately 24% of the acquisitions were in error. With JSNR = 2 and JS = 250, out of 50 acquisitions 12 were wrong and 36 were correct (5000 ± 5). Two failures to acquire anything (i.e., complete misses during the gross delay search) were recorded. Again the acquisitions in error were approximately 24%. These false acquisitions were due to coincident noise peaks on two successive iterations. Evidently the probability of two noise peaks within 20 delay samples was fairly high. In fact, the probability of a noise appearing to be a target due to its coincidence in range on two successive iterations is easy to calculate. Since on the average one noise peak with an allowable range jitter of 20 samples occurs

on each iteration then after one iteration 40 out of 1024 delay samples are suspect targets. Thus the probability of completing the next iteration without terminating on a noise peak is $\frac{1024 - 40}{1024} = 0.96$. The gross search from 3000 to 5000 delay samples by increments of 250 delay samples per iteration requires (5000-3000)/250 = 8 iterations. However the test cannot terminate after the first iteration hence 8 - 1 = 7 iterations could possibly cause termination of the test. After the 8 iterations required to reach the target the probability of erroneous termination of the test is $1 - 0.96^7 = 0.249$ as measured.

This large error rate was clearly unsuitable; therefore an improved algorithm for acquisition was tried.

4.1.2 "Three Largest" Detection and Acquisition of Stationary Targets by Three Observations at the Same Range

In order to reduce the probability that a target would be declared when in fact only two large coincident noise peaks had occurred the requirement for coincident range observations was raised to three.

First twin observations of largest peaks near the same range were stored and then after a third observation at the same absolute range a target was declared. This scheme had the effect of reducing the probability of noise being declared as a target by a large factor so that erroneous acquisitions became almost non-existent. However as expected the probability of a complete acquisition miss increased somewhat as compared to two observations at the same range.

To prevent discarding any useful targets which did not cross the threshold the level test, against the threshold described previously, was omitted so that all targets and noise regardless of their absolute magnitude became eligible as targets providing they satisfied the "three largest" requirement. This was done to maximize the probability of acquisition.

A long series of acquisition runs were made with different signal-to-noise ratios and different values of replica delay increment JS to try to display the minimum acquisition time for each signal-to-noise ratio; the results are shown in Fig. 39.

In addition, the average time to acquire the target correctly was calculated on the basis that a total miss would terminate the acquisition run when the complete delay range had been covered and subsequently the gross search would be repeated until a successful acquisition occurred.

In Table I the data used to plot Fig. 39 is tabulated. In the graph Fig. 39 the average time for positive acquisition, T_{AV}, and the probability of acquisition on one search, P_{ACQ}, are plotted versus signal-to-noise ratio for different values of replica delay increment JS.

The error bounds shown for P_{ACQ} in Table 1 were obtained from the outcome of the Monte Carlo trials. The probability of success in one trial was estimated by performing 100 trials and P_{ACQ} was recorded as the number of successes divided by 100. A formula for the error bounds of the Monte Carlo method for

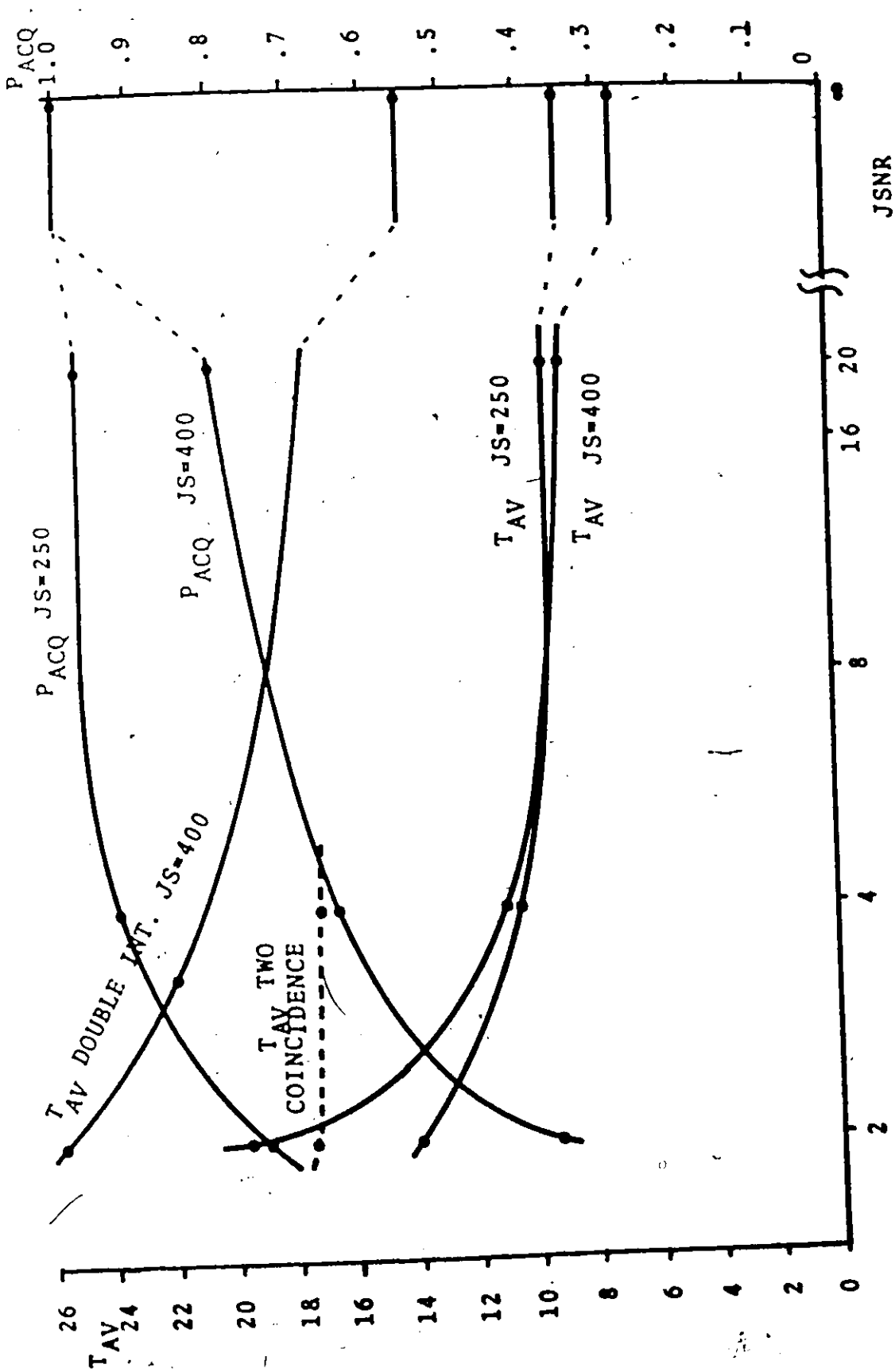

figure 39. The Average Time to Acquire the Target Correctly T_{AV} and the Probability of Acquisition per Search P_{ACQ} Versus JSNR.

TABLE 1

TABLE SHOWING T_{AV}, THE AVERAGE TIME TO POSITIVELY ACQUIRE THE TARGET, VERSUS JSNR

JSNR	JS	T_A	T_M	P_{ACQ}	P_M	P_{ERROR}	T_{AV}
TRIPLE COINCIDENCE							
2	250	9.7	12.	0.74 ±0.14	0.26	0.00	13.9 ±2.7
4	250	9.5	12.	0.93 ±0.08	0.07	0.00	10.4 ±1.0
20	250	9.3	12.	0.98 ±0.04	0.02	0.00	9.6 ±0.5
2	400	7.0	7.5	0.37 ±0.15	0.62	0.01	19.8 ±7.0
4	400	7.0	7.5	0.66 ±0.15	0.34	0.00	10.9 ±2.0
20	400	7.0	7.5	0.81 ±0.12	0.19	0.00	8.8 ±1.5
DOUBLE INTEGRATION							
2	400	14.0	15.0	0.56 ±0.22	0.44	0.00	26 ±10
SINGLE INTEGRATION TWIN COINCIDENCE							
2	250	8.8	12.0	0.72 ±0.14	0.04	0.24	17 ±3
4	250	8.4	12.0	0.76 ±0.14	0.00	0.24	17 ±3

The error bounds shown are for a 90% confidence level.

P_{ACQ} = Probability of acquisition obtained by dividing the number of successfully terminated searches by the total number of searches.

P_M = Probability of a total miss in which the total delay range is covered without any target declared.

P_{ERROR} = Probability of an erroneous target range being declared as measured in 100 trials.

T_A = The average number of iterations of the correlator required for the successful acquisitions only.

T_M = The number of iterations which cover the complete delay range. These iterations occur when a total acquisition miss occurs.

T_{AV} = The average time required for a guaranteed correct acquisition including time taken by errors and misses which require repeated searches.

JS = The replica delay increment by which the search advances at each iteration.

JSNR = The factor by which the noise is divided in the simulation. This parameter controls the noise amplitude.

estimating the probability of an event is shown in Appendix A as Equation (A.11) which is reproduced here as follows:

$$\left|\frac{K}{N} - p\right| \leq \sqrt{\frac{p\ (1-p)}{\varepsilon N}} \qquad (61)$$

where N = the number of trials

K = the number of successes in N trials

p = the true probability of the event

$1-\varepsilon$ = the confidence level

According to Equation (61) the accuracy of the Monte Carlo method improves as $\sqrt{N}$ which means that the computation time would have to become four times as long to double the accuracy (say). The values used for the confidence level in practice range between 65% and 99.7%. We shall assume a confidence level of 90% for which the error bounds are as shown in Table 1. The error bounds on T_{AV} follow from those for P_{ACQ}. The results shown are useful to indicate that P_{ACQ} increases when the replica delay increment JS decreases.

It can be seen that at signal-to-noise ratios less than JSNR = 2 the probability of acquisition on one search falls very low. As a consequence the search must be repeated until acquisition is completed. Therefore the average time for positive acquisition increases sharply below JSNR = 2. There is a trade-off between the probability of acquisition and the increment by which the replica delay increases. A search with a very small increment JS raises the probability of acquisition but takes longer to complete. At extremely low signal-to-noise ratios there may be an advantage to doubling the integration

time by adding two correlator outputs together. Some values of T_{AV} are shown for double integration but they do not provide any time saving except at very low signal-to-noise ratios.

4.2 Tracking

In the acquisition mode the decision-directed loop acquires the target. When the target has been acquired the next problem is to maintain the target in lock; this is the tracking mode. In this mode of operation the loop attempts to automatically adjust the delay of the replica to maintain coincidence between the two 1024 sample groups of the target echo and the stored replica. If the loop maintains nearly complete overlap between the two batches of samples, then the delay of the replica is a sampled estimate of the absolute delay of the target echo.

In some applications such as gun fire control it is mandatory to produce the estimate with the smallest possible mean square error. In other applications such as air traffic surveillance the absolute accuracy is less important than the reliability of tracking as measured by the mean time to unlock. Both these tracking criteria have been measured to explore the advantages of the decision-directed loop.

An optimized delay-lock discriminator was used simultaneously along side the decision-directed loop during the simulation experiments, for comparison purposes.

4.2.1 Experiments Measuring Total Square Delay Error while Tracking a Step Input of Delay

In order to measure the total performance of the decision-directed loop, both delay estimate jitter and transient error were squared and summed for a small positive step up and down. Only 20 iterations were used to measure the summed square error. For the delay input a constant for 5 iterations was followed by a positive step for 10 iterations and concluded with a negative step back to the previous delay for 5 iterations. The delay estimates of both the decision-directed loop and the delay-lock discriminator were stored and displayed. The tracking test was repeated a large number of times and the mean squared delay error was measured for both loops.

During these tests the signal-to-noise ratio was lowered successively while modifications were made to the decision-directed loop to try to maintain accurate tracking for as low a signal-to-noise ratio as possible.

One Largest Peak with No Prior Weighting

Initially the feedback algorithm involved no prior probability but merely produced the delay correction on the basis of the position of the largest correlator peak. Tracking of the square step is shown for JSNR = 1 in Fig. 35(b) for this feedback method. In the photograph the lower trace is the response of the delay-lock discriminator to a step of 20 delay samples which covers 0.45 vertical divisions on the photograph.

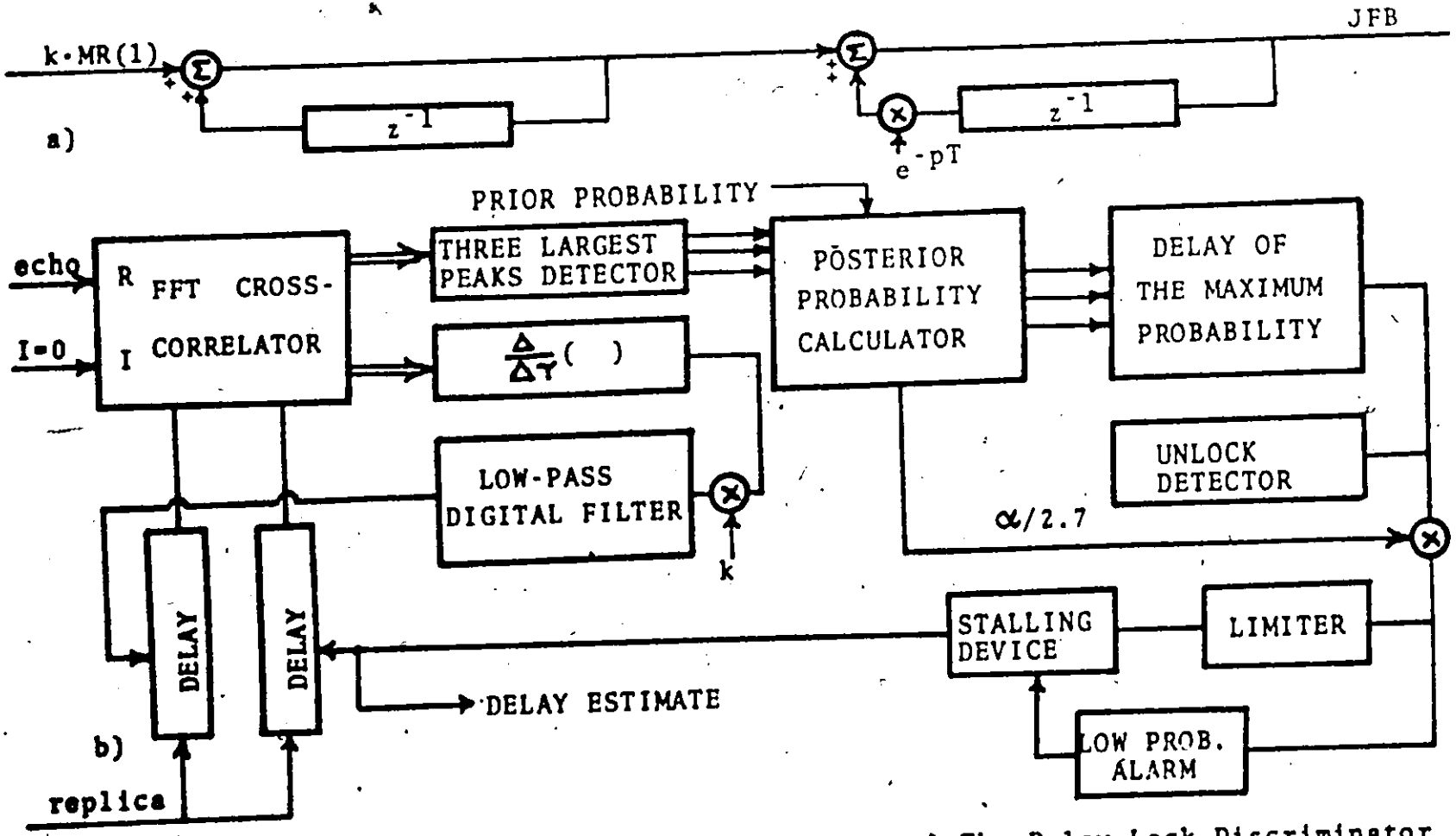

Figure 40. The Tracking Loop Test Block Diagram a) The Delay-Lock Discriminator Low-Pass Digital Filter b) The Decision-Directed Loop and the Delay-Lock Discrim-inator Combined Including Decision Error Reducing Devices.

On the same scale the upper trace shows the response of the decision-directed loop in its primitive form. It can be seen that at the sixth iteration the decision-directed loop jumps immediately to the correct new delay. However at the ninth iteration a large noise peak was picked as the target echo and lock was thereby lost. The delay-lock discriminator exhibits a slow transient response but does not lose lock.

The improvements to reduce decision errors in the decision-directed loop which are described in the next section are incorporated in the feedback path as shown in Fig. 40(b). In this case we have advanced to the calculation of posterior target delay probability at two and finally three correlator peaks. This allows the decision loop to operate at signal-to-noise ratios when sometimes as many as two noise peaks will exceed the target peak.

Three Largest Peaks with Prior Range Weighting

The final form of the decision-directed loop is shown in Fig. 40(b). It incorporates a large number of restraints into the decision feedback path. The purpose of these restraints and the advantage gained by using them will be described in the following paragraphs.

At low signal-to-noise ratios delay jitter can be reduced by reducing the delay correction feedback gain. In Fig. 41 the delay step described previously is used to test the effect of gain reductions on delay estimate jitter and transient response. In Figs. 41(a) and 41(b) for direct feedback and feedback gain equal to $\frac{1}{2}$, respectively, the

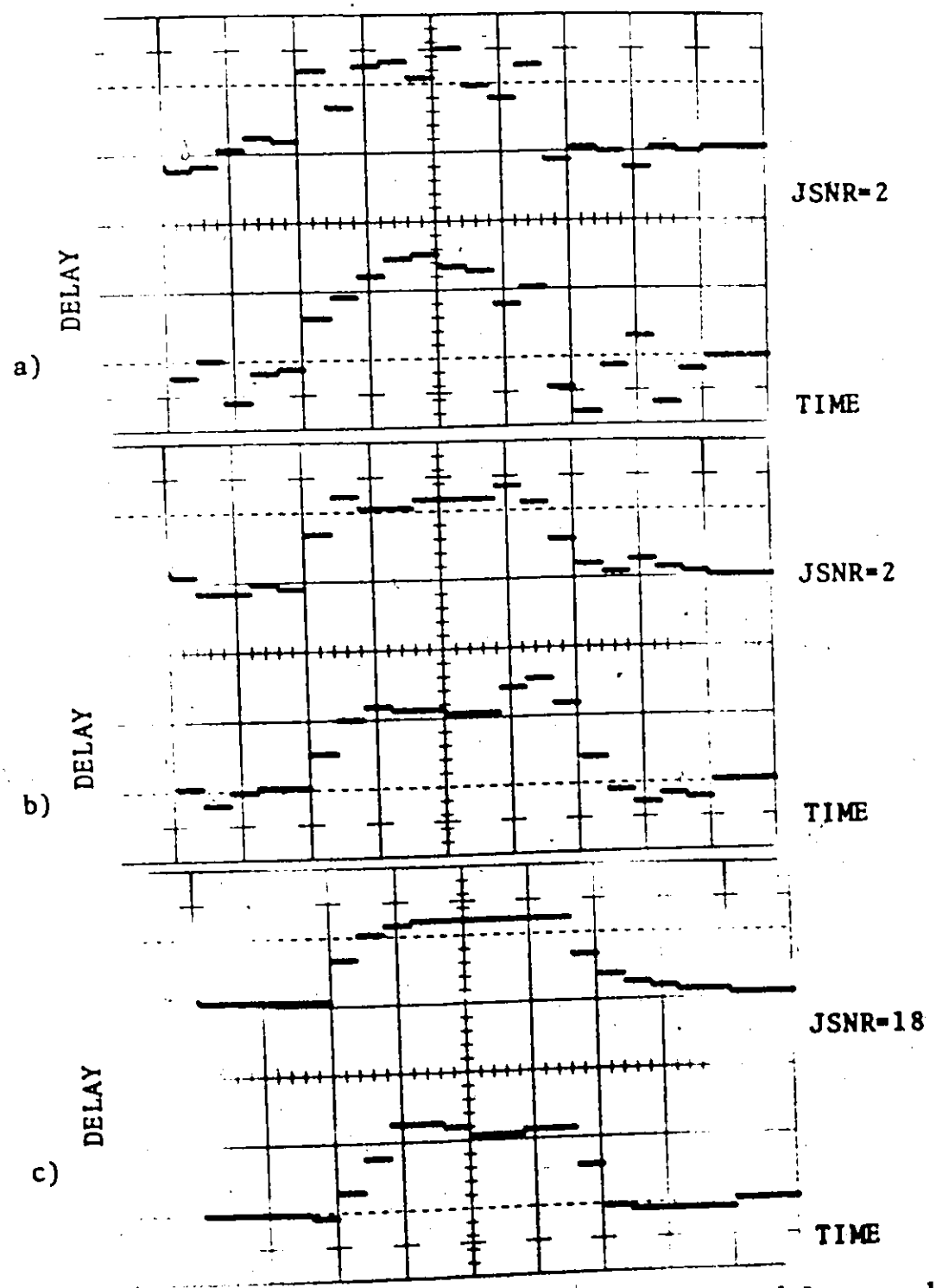

figure 41. Step Response of Decision-Directed Loop and Delay-Lock Discriminator (Upper and Lower Traces Resp.) for 20 sample Delay Input (1.2cm. vert.), a) Direct Decision Feedback, b) and c) Decision Feedback Multiplied by 1/2.

reduction in jitter for the reduced gain can be seen. This reduction in gain is beneficial at low signal-to-noise ratios but introduces a transient response at high signal-to-noise ratios, Fig. 41(c). Automatic feedback gain control which allows direct feedback at high signal-to-noise ratios and reduced feedback gain at low-signal-to-noise ratios will be described.

Decision errors which may occur at low signal-to-noise ratios are often the cause of loss of lock in the decision-directed loop. Although errors have a low probability of occurring when R is above the "threshold of intelligibility" as noted from Equation (21), they cause a large delay error when they do occur. To prevent loss of lock due to delay estimate errors a limiter is included in the feedback loop. The purpose of this limiter is to prevent any one erroneous decision from carrying the replica delay a long distance away from the true target in one iteration. The characteristic of the limiter is shown in Fig. 42. When the input delay moves slowly from sample to sample the delay correction will seldom exceed 50 samples. Therefore for true targets the limiter will not act. However for errors due to noise which would tend to unlock the decision-directed loop the limiter will prevent loss of lock. For an erroneous replica shift of 50 samples the decision-directed loop will usually return to the true target on the next iteration.

Another safety device included in the feedback loop is a "stalling device" as indicated in Fig. 40(b). This device blocks feedback of decisions which indicate a large delay

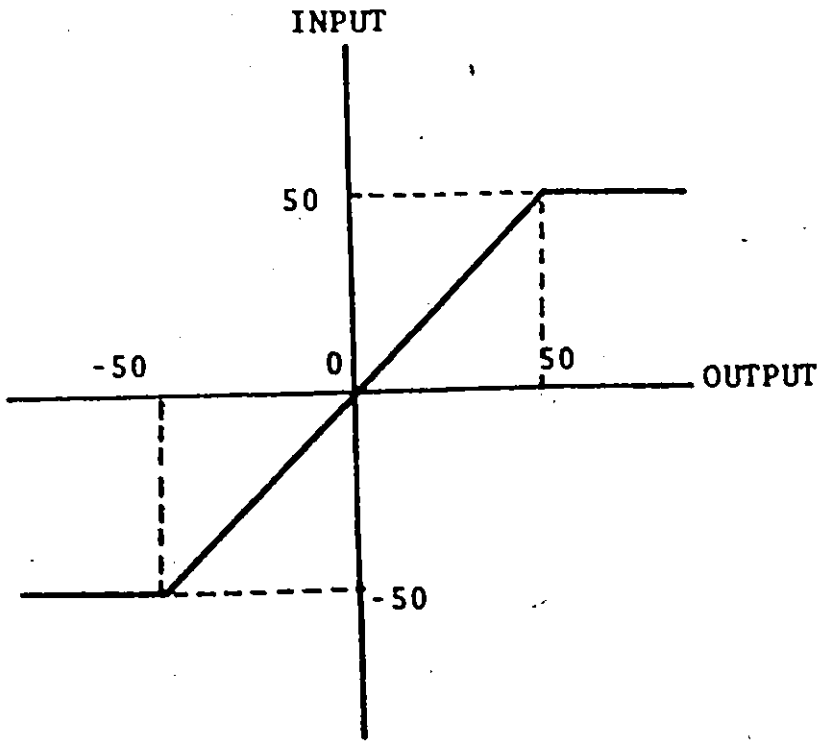

figure 42. The Input-Output Characteristic of the Decision Feedback Limiter.

correction and have a low probability of being due to the target. Large feedback corrections of a low probability are subject to a double check. When the signal-to-noise ratio is low and a large step input of delay is applied, for example, then the new target just after the step has occurred may have a low probability. Thus the first feedback correction is nulled and only a repeated decision to make the same correction will be acted upon.

The total squared error (in units of delay samples squared) is shown versus signal-to-noise ratio in Fig. 43 for a step input of 20 delay samples as described previously. The total squared error was computed for each of 10 trials using 20 iterations per trial. According to the Monte Carlo error bounds for 90% confidence level the error in a mean value is: (see Equation (A.6) of Appendix A).

$$|\bar{b}-\mu| \leq 1.645 \sqrt{\frac{\sum_{i=1}^{N} (b_i-\bar{b})^2}{N(N-1)}} \qquad (62)$$

where b_i = the outcome of trial i

$\bar{b}$ = the mean value of the outcomes of trials 1 to N

μ = the true mean value

For N = 10 and an assumed confidence level of 90% the error bounds were calculated using Equation (62) and the results are given in Table II. This table shows that the error is of the order of 10% at low signal-to-noise ratios and of the order of

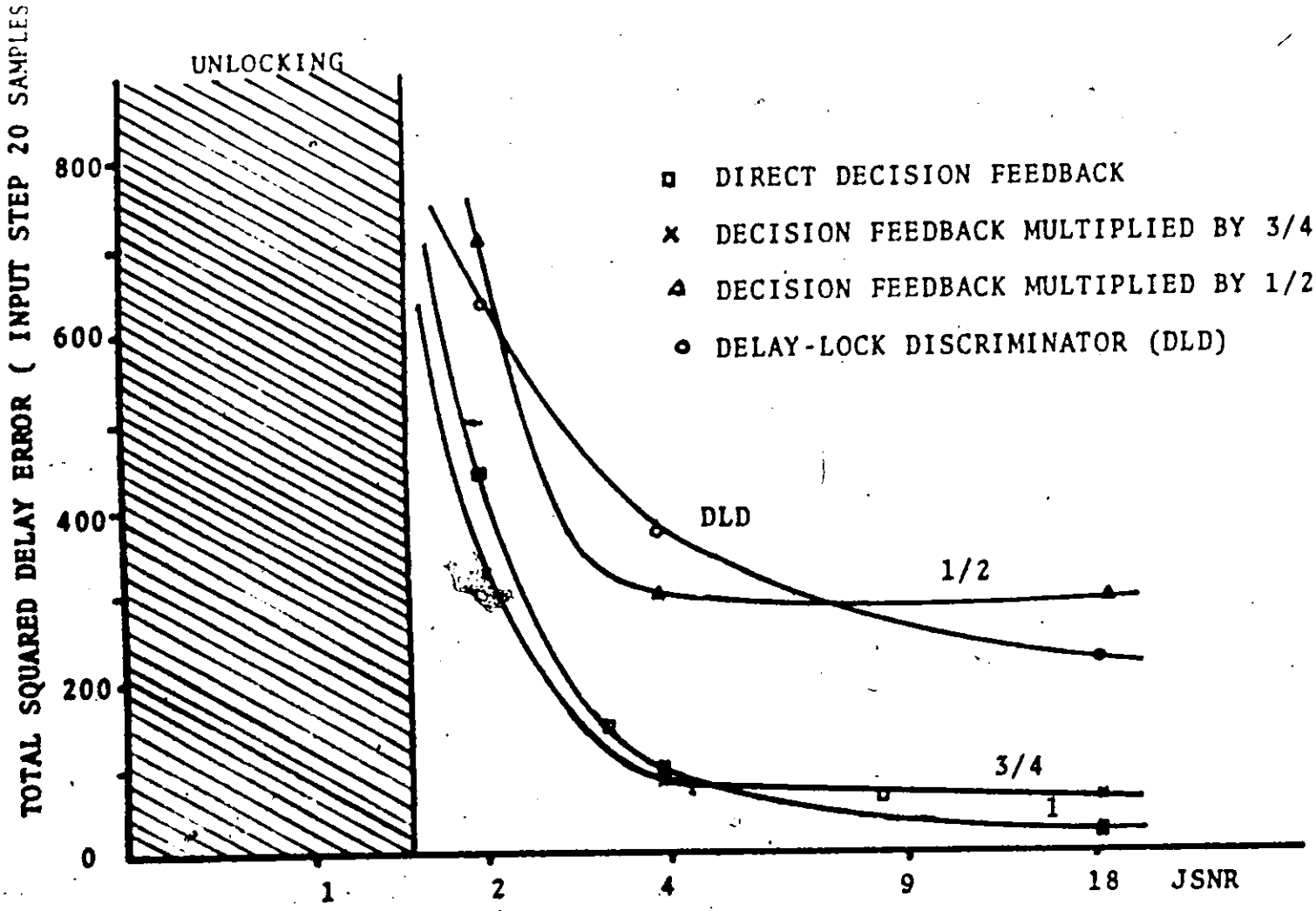

figure 43. The Total Squared Delay Error for a Step Input of 20 Delay Samples for the Decision-Directed Loop with Various Feedback Gains. The Error of the Delay-Lock Discriminator is also Shown Versus JSNR. Data in Table II.

	JSNR = 18	JSNR = 4	JSNR = 2
DIRECT DECISION FEEDBACK	17 ±5	100 ±20	420 ±45
DECISION FEEDBACK MULTIPLIED BY 1/2	283 ±5	300 ±60	700 ±75
DECISION FEEDBACK MULTIPIED BY 3/4	69 ±3	90 ±20	340 ±40
DELAY-LOCK DISCRIMINATOR	215 ±10	370 ±20	660 ±90

TABLE II. THE TOTAL SQUARED DELAY ERROR IN SAMPLES SQUARED, OF THE DECISION-DIRECTED LOOP AND THE DELAY-LOCK DISCRIMINATOR AS A FUNCTION OF JSNR. THE ERROR BOUNDS SHOWN ARE FOR A CONFIDENCE LEVEL OF 90%.

5% at high signal-to-noise ratios. The results indicate that the performance of the decision-directed loop and the delay-lock discriminator are approximately equal at low signal-to-noise ratios and that at higher signal-to-noise ratios the performance of the decision-directed loop can be improved by adjusting the feedback gain. Since the delay-lock discriminator was optimized for low signal-to-noise ratios therefore the decision-directed loop cannot exceed its performance. However at high signal-to-noise ratios the direct decision feedback is clearly superior.

The decision-directed loop offers the unique feature of providing a quantity which is dependent on the signal-to-noise ratio as illustrated in Fig. 44. The output of the "three largest peaks device" consists of the amplitude of the target and two amplitudes due to noise. A quantity, denoted by α that is dependent on the signal-to-noise ratio may be calculated with little further effort by dividing the target peak amplitude by the average of the three peak amplitudes. When the noise is negligible, α has an average value equal to three. At low signal-to-noise ratios, α has an average value equal to one, as then all three peaks have the same amplitude. Automatic feedback control was tested by using α to control the feedback gain. In this way near optimum mean squared error performance was obtained over a wide range of input signal-to-noise ratios.

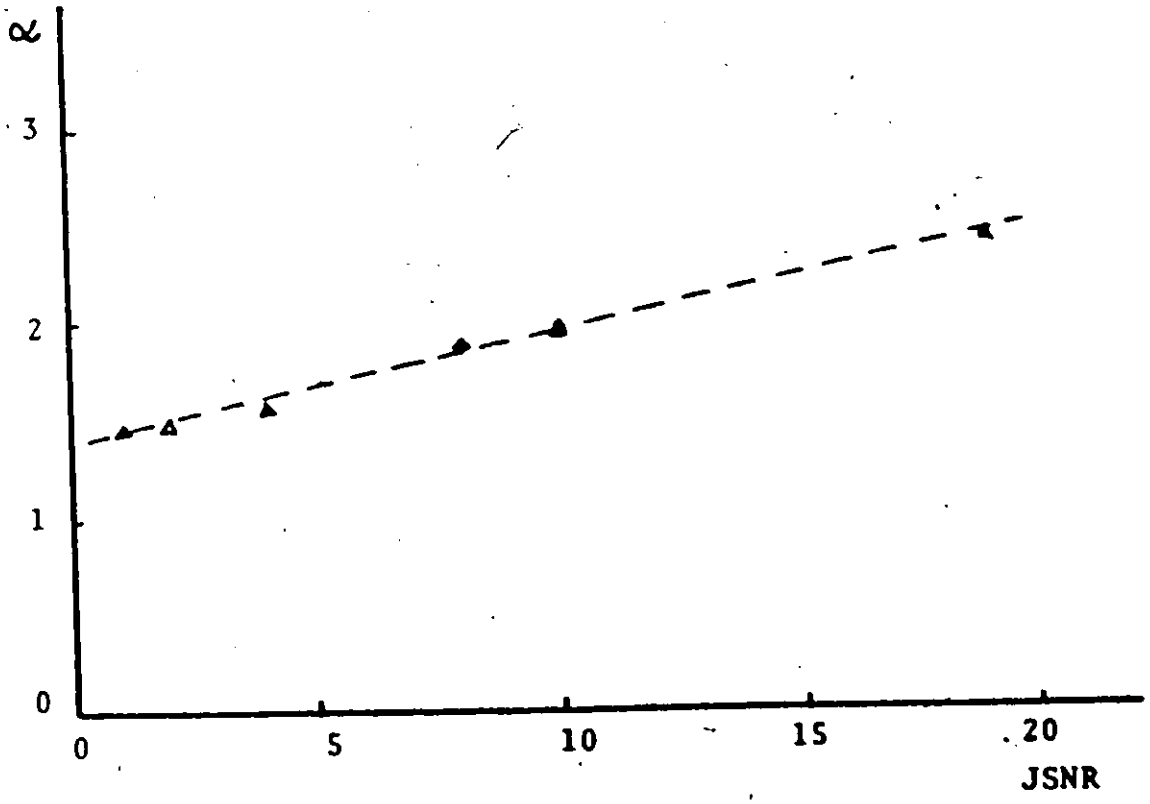

figure 44. Illustrating the Quantity α, Equal to the Target Peak Amplitude Divided by the Mean of the Three Largest Peaks, Which is Dependant on the Input Signal-to-Noise Ratio.

4.2.2 Response to Large Steps of Delay

The following tests demonstrate the wide dynamic range of the decision-directed loop. It is free of the non-linear response of the delay-lock discriminator when sudden large delay steps are applied. In Fig. 22, lower trace, the linear portion of the discriminator characteristic appears to be about 0.06 division or 15 delay samples. For steps of input delay greater than this amount the delay-lock discriminator loop gain is reduced or may even reverse in sign. To examine the nonlinear discriminator response the height of the delay step was increased from 20 to 50 units. For a step of 50 units in Figs. 45(a) and (b) for JSNR = 9 with automatic feedback gain the response of the decision-directed loop is essentially dead-beat in two iterations. For the same conditions the delay-lock discriminator exhibits a very slow initial transient response due to low feedback gain. When the signal-to-noise ratio is lowered to JSNR = 2 so that considerable delay jitter is added to the transient response as shown in Fig. 45(c) the delay-lock discriminator loses lock on the downward step of 50 units.

For a step of 100 delay samples in Figs. 46(a) and (b) the delay-lock discriminator fails to respond while the decision-directed loop, using direct feedback, is dead-beat in one iteration. For these tests the prior probability of the target range was not changed or made any wider than for the tests with the step of 20 delay samples. Thus it is shown that for large steps of delay the decision-directed loop performs better where

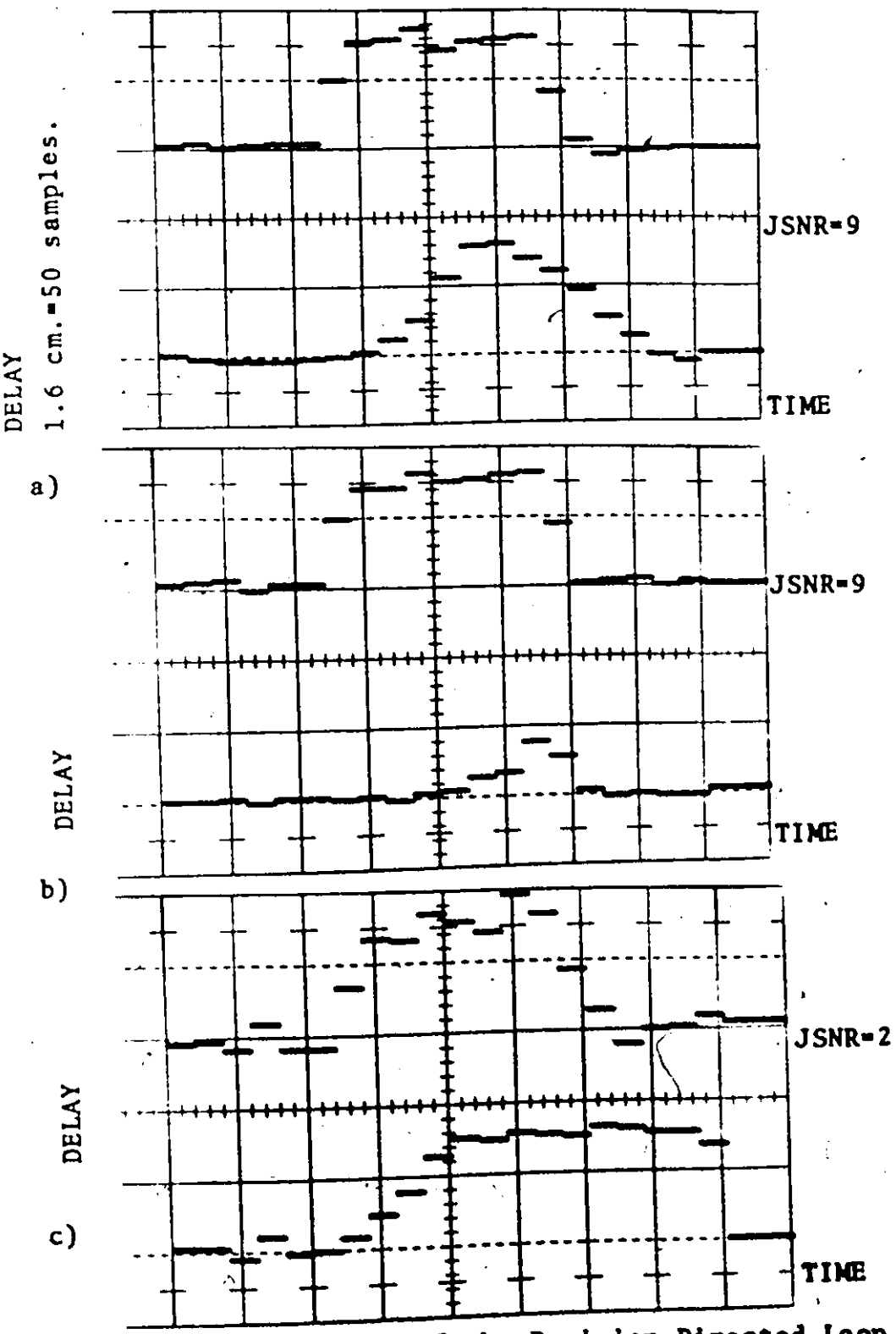

figure 45. The Response of the Decision-Directed Loop to a Large Input Delay Step of 50 Samples. The Response of the Decision-Directed Loop is the Upper Trace and the Response of the Delay-Lock Discriminator is the Lower Trace.

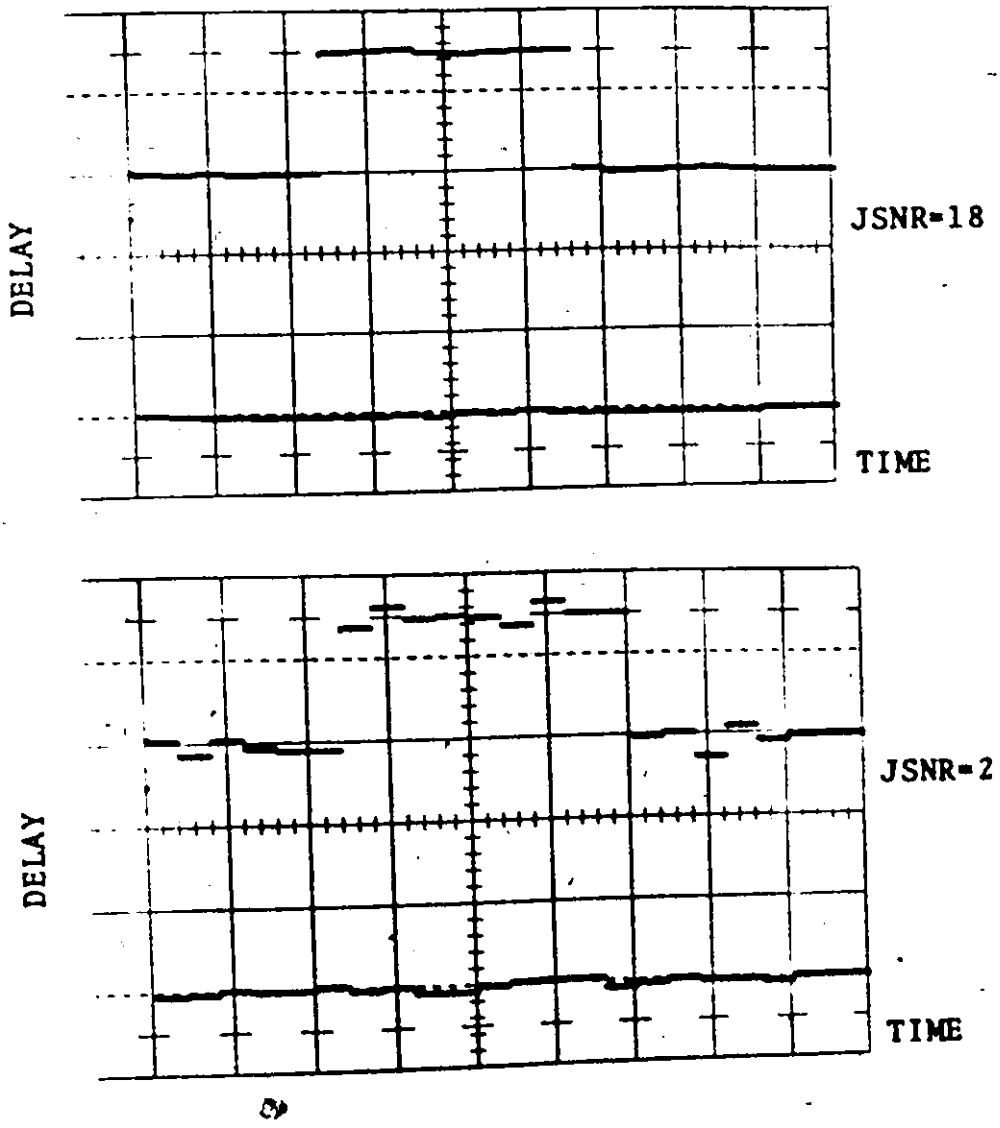

figure 46. The Response of the Decision-Directed Loop (Upper Trace) and the Delay-Lock Discriminator (Lower Trace) to a Large Input Delay Step of 100 Samples (Vertical Scale: 100 Samples = 1.5 cm.).

the delay-lock discriminator responds sluggishly or unlocks.

4.3 Detection of Unlocking

In order to automatically switch between the modes of acquisition, tracking, detection of unlocking and reacquisition it is necessary to be able to detect when the loop has lost lock. In the delay-lock discriminator, for example, the detection of unlock is difficult for some types of target motion. Suppose the target echo is very weak and executes a random walk in range. The output delay estimate of the delay-lock discriminator will execute a random walk whether the loop is in lock or not. There is no point in the circuit at which the signal can indicate the loss of lock.

The decision-directed loop, on the other hand, has a point in the circuit at which a value exists which does indicate the locked condition. This point is the output of the device measuring the maximum posterior probability. When lock is lost the output of this device decreases on the average in a marked fashion. There is however a strong statistical variation in the maximum probability output and it would not be desireable to terminate the track mode prematurely if an occasional low probability were to occur. Therefore an averaging device was connected to the output of the posterior probability device to smooth the statistical fluctuations. For this purpose an RC low-pass filter with a time constant of ten iterations was found to be satisfactory. An alarm level was established so that when the smoothed probability of a target fell below this level the state of unlock could be declared.

4.3.1 Mean Time to Unlock while Tracking a Sinusoidal Delay

A sinusoidal delay variation was chosen to test the mean times taken to unlock the decision-directed loop and the delay-lock discriminator. The sinusoidal delay had a peak-to-peak amplitude of 100 delay samples and a period of 20 iterations.

The "three largest" decision-directed loop with automatic feedback gain control with the limiter and stalling device in the feedback loop was used for this test. The delay-lock discriminator was tested simultaneously using the same loop filter as previously. With the signal-to-noise ratio set at JSNR equal to 2 both loops were run for 1000 iterations without unlocking in either loop. Next, the signal-to-noise ratio was lowered to JSNR equal to 1. Three typical tests are shown in Fig. 47 which terminate after unlock has been detected in the decision-directed loop. Occasional lack of tracking occurs when the probability of a target falls low enough to cause stalling in the decision-directed loop. The mean time to unlock was measured using 27 trials at JSNR = 1. The mean time to unlock for the decision-directed loop was 41 $\pm$ 10 iterations using the three largest peaks detector. For comparison the decision directed loop using two peaks unlocks in 20 $\pm$ 5 iterations and that using one peak unlocks in less than 8 iterations. The delay-lock discriminator mean time to unlock was 30 $\pm$ 7 iterations.

4.4 Mode Switching of the Decision-Directed Loop

The decision-directed loop has the unique capability of automatically choosing its own mode of operation depending

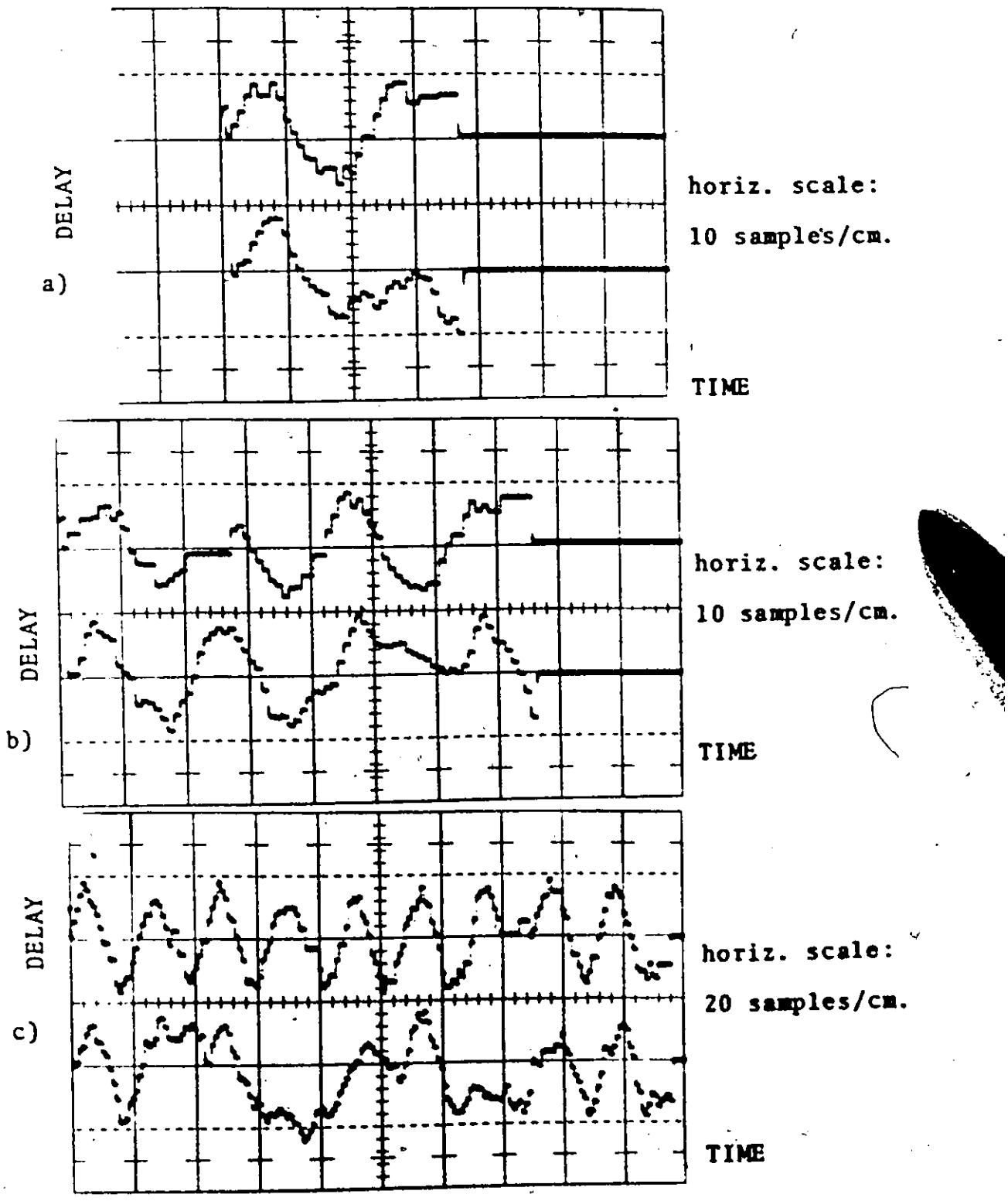

figure 47. Time to Unlock While Tracking a Sinusoidal Delay. The Upper Trace is the Decision-Directed Loop and the Lower Trace is the Delay-Lock Discriminator, JSNR=1.

on the situation in which it finds itself. Initially when the target is unknown the prior probability of delay is uniform over the whole range of possible delays. In this case the acquisition mode is chosen. The replica delay will be advanced by equal increments to cover the whole range of delay until a target appears three times at the same absolute range. If the acquisition mode fails to locate the target, the mode may be repeated using a doubling of the integration time of the correlator and/or decreasing the increment by which the replica delay advances so that each range bin is examined for a longer time. When a target is declared by the acquisition mode the estimated range of the target will be passed on to the tracking mode.

The tracking mode can apply prior weighting of the delay to assist in tracking the target peak at the correlator output. At low signal-to-noise ratios the mean time between unlocking of the loop becomes low enough that it can be measured easily. The loop may also unlock if the target were to change range suddenly. When the target is lost the probability of a true target being present at the correlator output falls to a low level and the unlock detector gives an alarm.

The task of reacquiring a target that has been lost by the tracking loop is a difficult one. The tracking loop has the advantages of prior delay probability, and near complete overlap between the incoming echo and the replica. The best scheme to use in reacquiring the lost echo is to assume that the delay of the echo is still within the range of the 1024 (say)

samples of the replica. This assumes that the highest probability of the echo delay is located near the absolute delay at which the echo was lost. The scheme is then to repeat the iterations of the correlator as fast as possible at the same replica delay and to sum the correlator outputs. If a target is still present at a constant range it will eventually show itself provided it is within the range of the replica delay. When a target appears its range can be passed along to the tracking mode again. However if the signal-to-noise ratio is low such that unlocking in the tracking mode occurs too frequently then a doubling of the integration time by summing the correlator outputs may be necessary. This, of course, requires that the target remain in approximately the same range bin for two or more iterations. It is an inescapable fact that at low signal-to-noise ratios the bandwidth of the feedback loop must necessarily be small to maintain lock and the variation in the motion of the target must be correspondingly small also, otherwise lock will be lost.

An experiment was performed to prove the ability of the decision-directed loop to manage the switching between modes. The target signal-to-noise ratio was held at JSNR = 1 and after acquisition the tracking mode was automatically started at the range indicated by the acquisition mode. The number of iterations required to acquire the target was determined and the number of iterations before lock was lost was also recorded. Subsequent

reacquisitions were much shorter in time than the first because of the smaller possible delay extent searched.

It was necessary to quadruple the correlator outputs because the correlator output ambiguity at JSNR = 1 was too large to produce a reasonable probability of positive acquisition. One iteration at JSNR = 1 produces a peak echo energy to correlator variance ratio R = 6 which is too far below the threshold of intelligibility to give useful results. Woodward's formula for the threshold requires $R_t \approx 12$. Since $R = 2E/N_o$, where E is the signal energy, adding four correlator outputs together increases the received energy E by a factor of 4 and increases the received noise energy by a factor 2 which exactly doubles the value of R. Quadrupling increases R from 6 to 12 so that the intelligibility threshold is reached.

A histogram plotting the time taken by each mode is shown in Fig. 48.

4.5 Summarising Remarks

The fast Fourier transform (FFT) has been used to perform cross-correlation in a new decision-directed delay-lock loop. FFT correlation produces a complete set of lagged products of the two 1024 sample sections of the inputs, and these extra correlator outputs allow additional information to be derived in the decision-directed loop. Three modes of operation of the loop have been demonstrated, namely acquisition, tracking, and detection of unlocking. The decision-directed loop can switch

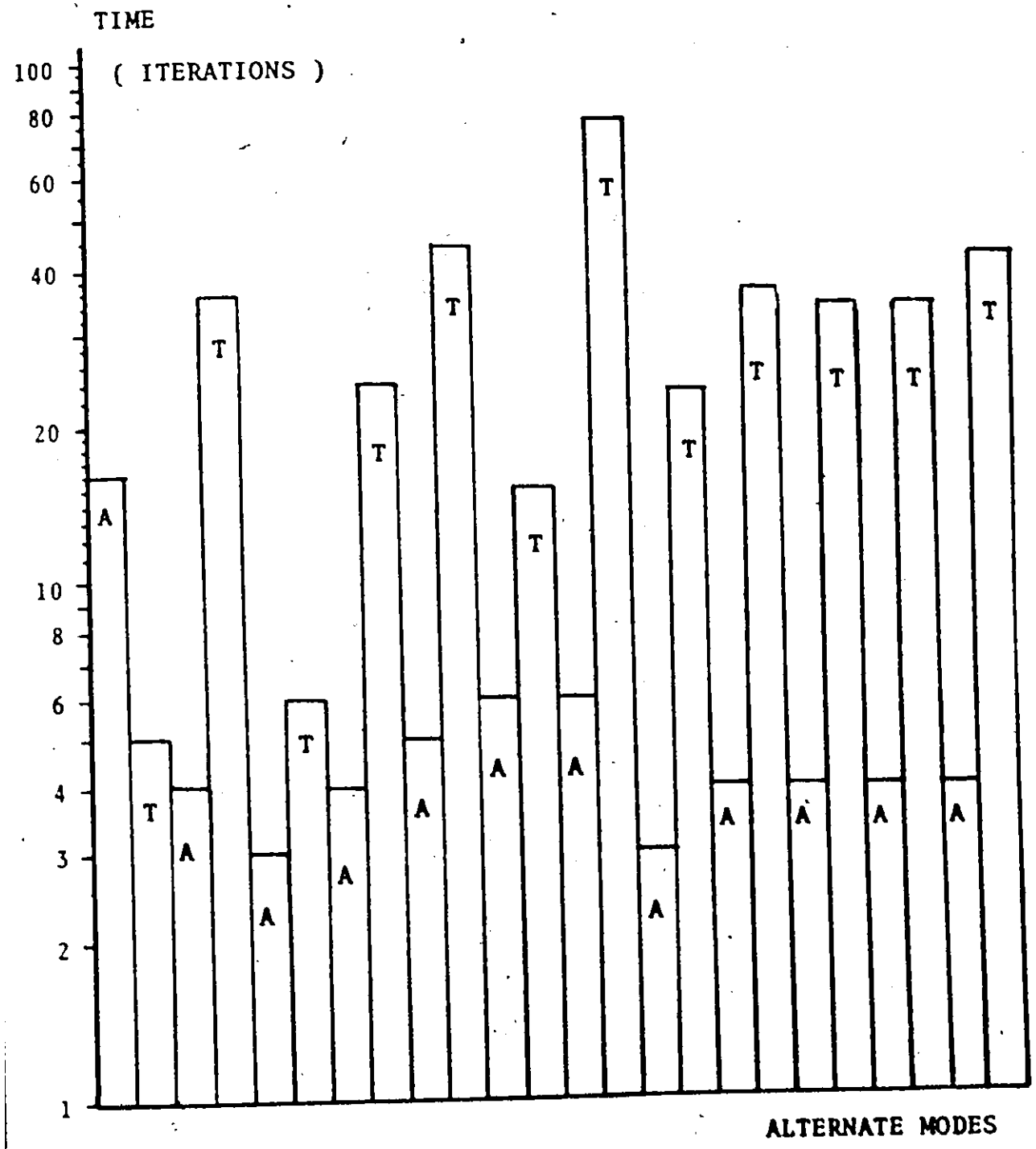

figure 48. Mode Switching of the Decision-Directed Loop. "A" is the Acquisition Mode and "T" is the Tracking Mode. The Time in Each Mode is Measured in Iterations with JSNR=1.

automatically between the modes depending on the state of the correlator output.

A delay-lock discriminator was operated simultaneously with the decision-directed loop for comparison purposes. Using a random low-pass waveform with a Gaussian power spectrum as the transmitted signal the mean square errors of the two loops while tracking a step input of delay were compared. The mean times to unlock while tracking a sinusoidal delay input at low signal-to-noise ratio were also measured. The results show good agreement with Woodward's theory of delay measurement. The decision-directed loop operates by calculating the posterior probability of target range at the correlator output. This calculation may be simplified by choosing the largest correlator output and noting the delay of the target by the position of this peak on the range axis. For only "one largest" peak per correlator output the operation of the decision-directed loop was found to be subject to occasional erroneous decisions at low signal-to-noise ratios. The target range estimation was refined by choosing two and finally three largest correlator peaks and calculating their posterior probability of being due to a target. In this way as many as two noise peaks may exceed the target peak at the correlator output before a decision error is made.

In the acquisition mode the unknown range of stationary target was detected by increasing the replica delay by a constant increment on each correlator iteration until the target

peak was observed at the same range on three correlator outputs. The minimum average time to positively acquire the target was measured as a function of signal-to-noise ratio. There is an optimum rate of replica increment for each signal-to-noise ratio; this increment is large for high signal-to-noise ratio and decreases for low signal-to-noise ratio where the probability of detection decreases. Below Woodward's "threshold of intelligence" it is necessary to increase the integration time by adding successive correlator outputs.

In the tracking mode the acquired target is locked-in using decision feedback to maintain near complete overlap between the target echo and the delayed replica. Three types of feedback gain were investigated namely direct feedback, attenuated feedback and automatic feedback. The automatic feedback allows dead-beat response to a step of delay at high signal-to-noise ratios while reducing the feedback gain and the output jitter at low signal-to-noise ratios. Using automatic feedback the decision-directed loop can attain a mean squared error performance which is better than or equal to that of the delay-lock discriminator over a wide range of signal-to-noise ratio. For small input delay steps within the linear range of the delay-lock discriminator the performance of the two loops at low signal-to-noise ratios was shown to be similar. However for large input delay steps the range of linear dynamic response for the decision-directed loop was greater.

The decision-directed loop has the unique capability of calculating a quantity dependent on the input signal-to-noise ratio by using values already existing in the loop. This quantity is calculated by comparing the signal peak at one range with the noise peaks at other ranges. Unlocking of the loop can be detected by averaging the maximum posterior probability of the target and declaring the system to be unlocked when this probability falls below a preset level. These two features allow automatic switching between the modes of acquisition, tracking, unlocking and reacquisition. The decision-directed loop requires a computer within the loop to make decisions and calculate posterior probabilities; however the advent of hard-wired FFT processors and small high-speed fixed-point computers allows the loop to operate in real-time for many applications.

A limitation of the decision-directed delay-lock loop as a tracking radar is that in a realistic situation where there would be large clutter returns from fixed and fluctuating reflectors the loop may lock on to one of these undesired returns. One way to overcome such a difficulty would be to use a delay-line canceller to diminish the effect of clutter.

Chapter 5

Moving Target Indicator Radar Systems

Moving target indicator (MTI) radar has been used since World War II to detect and track moving objects such as aircraft against a background of fixed ground reflections called clutter. To increase the radar sensitivity, higher peak transmitter power and longer pulses are used to provide greater target illumination. The range resolution of long pulses can be restored by modulating the pulses and using a matched filter in the receiver to compress the long pulse into a short autocorrelation function with high resolution. However the performance of these pulse-compression MTI radars often fall short of the designer's expectations. System oscillator instabilities and compression sidelobes are two known sources of degradation [35]. In addition, in fluctuating clutter the spectral spreading of the clutter return caused by nonlinearities in the radar may degrade the canceller performance [36, 37, 61]. In this thesis we shall indicate another cause of degradation which is peculiar to pulse-compression systems.

In land based air traffic control and surveillance MTI radar the clutter power reflected from geographic features and weather systems is often many orders of magnitude above the power of echoes from aircraft. Yet the circuits of the radar processor are restricted by state of the art of design to a dynamic range comparable with that of the total return. Limiters are often used at intermediate frequencies to control the dynamic range of the

received echoes; however, their effect on system performance is not completely clear from the available literature [1, 43-49].

A typical coherent MTI radar system is shown in block diagram form in Fig. 49. This system may be either a pulsed radar or a coded pulse-compression radar depending on the complexity of the pulsed modulation.

In Fig. 49, TR is the transmit receive diplexer. The coherence is maintained by the stable local oscillator (STALO) and the coherent oscillator (COHO). The STALO translates the COHO frequency to the radio frequency (RF), and translates the received RF down to the intermediate frequency (IF).

The limiter is used at IF to reduce the dynamic range of the return. Fast automatic gain control or logarithmic IF amplifiers are two other methods used to control the dynamic range. We shall study the effect of the IF envelope soft limiter. A single delay-line canceller is shown in Fig. 49 although higher order cancellers may be used. In the canceller the delay T, where T is the period of the transmitted pulses, allows subtraction of successive returns so that objects which return exactly the same echo from pulse to pulse do not appear at the output. Moving objects such as aircraft will return an echo with a different phase from pulse to pulse and thus will produce an output unless they are at a "blind speed". At these speeds the phase of the returning echo is shifted a multiple of 360 degrees by the movement of the target. This results in signals which arrive at the video canceller shown in Fig. 49, with the same phase at each

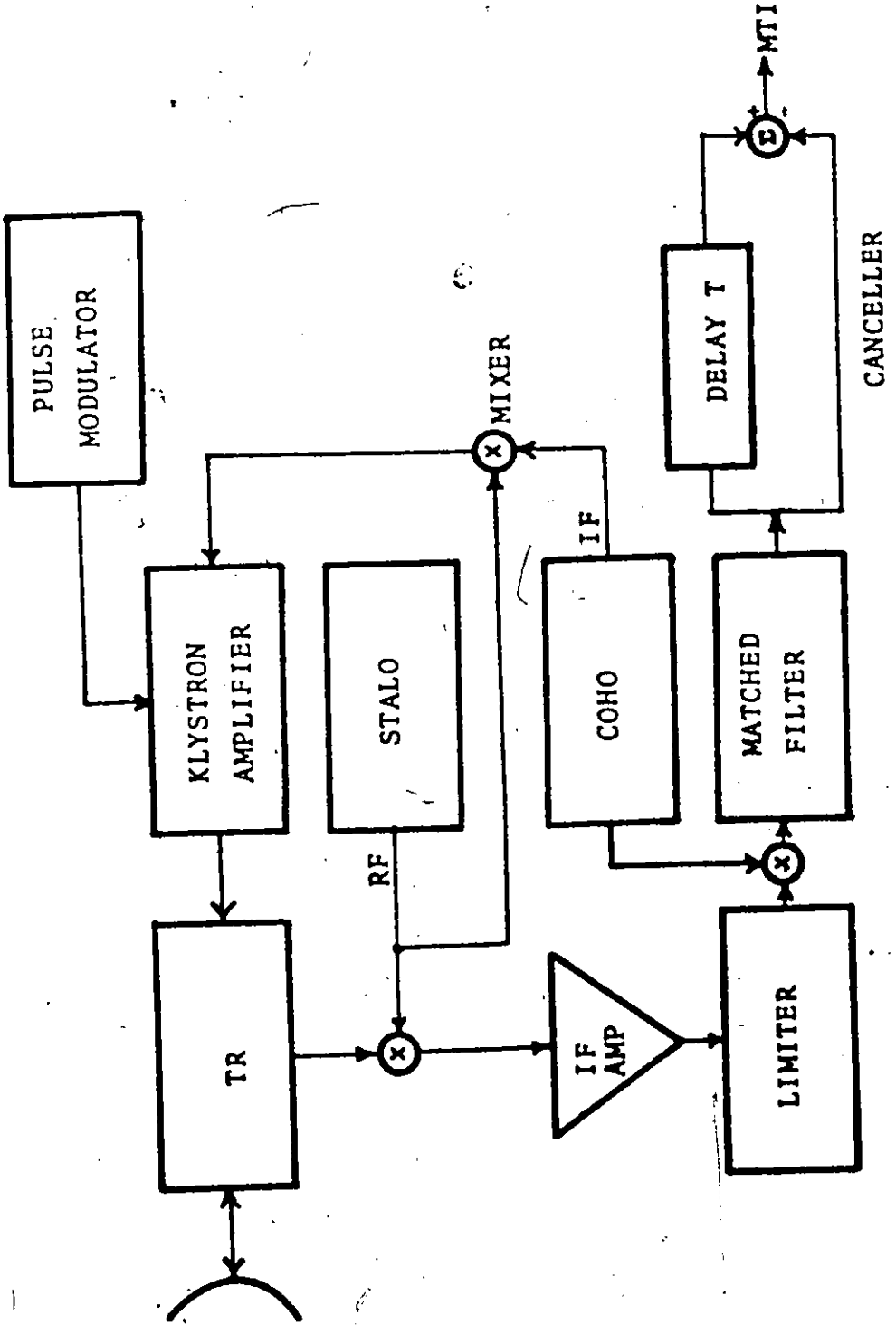

Figure 49. Phase-Coherent Moving Target Indicator Radar System.

pulse repetition. This situation is called a "blind phase" for coherent radar with video cancelling.

5.1. Pulse-Compression

Typical large time-bandwidth product waveforms suitable for pulse-compression are: linear frequency modulation (FM), non-linear FM, coherent frequency steps and pseudo-noise (PN) phase modulation, for example using M sequences. Frequency and phase modulation appear attractive for pulse-compression as the phase of the return is preserved in the limiter. A typical phase modulation is shown in Fig. 50(a).

The autocorrelation of this envelope is shown in Fig. 50(b). This 13 element code may be modulated onto an RF pulse by biphase modulation. Biphase modulation is accomplished by sending out two RF phases either 0 or 180 degrees. The phase of the RF pulse is reversed periodically according to the sign of the code element therefore the term phase reversal coding is also used. The Barker 13 code shown in Fig. 50(a) is also called a perfect word because its autocorrelation function for any shift of one element other than zero delay, is either 0 or 1/N where N is the number of code elements. No Barker codes are known to exist for N greater than 13.

The radar return from a moving point target contains a delay due to the two way propagation time of the transmitted electromagnetic energy, and contains a frequency shift, called Doppler due to the radial velocity of the target. These two

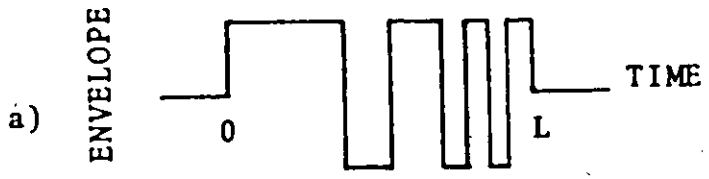

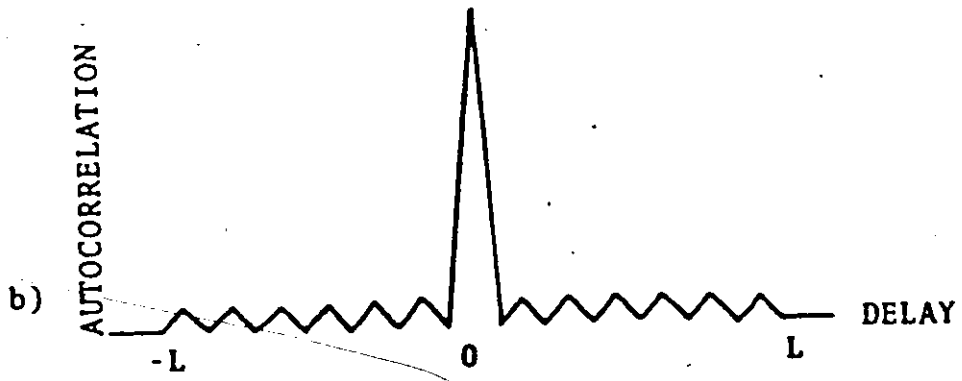

figure 50. A Phase Modulation Envelope for Pulse-Compression a) Barker 13 Biphase Code of Length L b) The Barker 13 Autocorrelation Function.

parameters, delay and Doppler, are defined by:

$$\tau = \frac{2r}{c} \tag{63}$$

$$f_d = \frac{2\dot{r}f_o}{c} = \frac{2v_r}{\lambda} \tag{64}$$

where τ is the delay, r is the radial distance from the radar to the target, $\dot{r} = dr/dt = v_r$ the radial target velocity, c is the velocity of light, f_o is the radar carrier frequency of wavelength λ and f_d is the Doppler shift.

When the target has constant velocity the output energy of the matched filter is given by the ambiguity function [38] defined by:

$$\psi(\tau, f_d) = \left[\int_{-\infty}^{\infty} u(t)\, u^*(t+\tau) \exp\{-j2\pi f_d t\} dt \right]^2 \tag{65}$$

where $u(t) \exp\{-j2\pi f_d t\}$ is the pre-envelope [39] of the transmitted signal and $u^*(t)$ is the complex conjugate of the complex envelope of the signal. When f_d is zero Equation (65) reduces to the square of the autocorrelation function of the signal. Fig. 50(b), showing the autocorrelation function of the Barker 13 code is therefore a section of the ambiguity diagram equal to $\sqrt{\psi(\tau,0)}$.

The effect of clutter which obscures the desired target may be reduced in two ways which the ambiguity function Equation (65) suggests. The first method is increasing the compression ratio of the signal. The range resolution for a constant length

coded pulse, goes up proportionally to the number of independent elements in the code. A higher number of elements requires a wider system bandwidth. The compression ratio is also equal to $T_p\beta$ where T_p is the pulse duration and β is the signal bandwidth. A "cell" is the smallest unit which can be resolved. By increasing the range resolution the size of the range cell is made smaller so that the contribution from clutter within one cell becomes less.

The second method of combating the effect of clutter is to try to find a waveform to transmit with a suitable ambiguity function. The system response to clutter with a different delay and Doppler than the target is minimized if the surface of the ambiguity function is low while the response to the desired target is large. However, suitable signals may not always exist or be convenient to transmit in many cases.

Signals with desireable properties on the range axis have undesireable properties on the Doppler axis [40]. The Barker 13 code, for example, has uniformly low sidelobes on the range axis but has very large responses for clutter with large Doppler frequency. Although pulse-compression promises to reduce the effects of clutter it brings additional problems. Pulse-compression MTI radar in particular requires a receiving system with a wide dynamic range. Two circuits in the receiver which may have a narrow dynamic range are the matched filter and the delay-line canceller.

One implementation of a matched filter for the Barker 13

code uses a tapped delay-line with the taps spaced according to the elements of the Barker 13 code. The art of delay circuit design often limits the dynamic range of delay lines to 50 db. Recent results for surface-wave delay devices show a dynamic range of 80 db with spurious responses due to cross talk and multiple transit effects 50 db below the input level [41]. Clutter returns from land and weather systems have a strong time-varying amplitude characteristic. The radar cross-section of geographic features such as mountains or forests may be many orders of magnitude greater than the cross-section of the target. These reflectors of varying strength lie at different ranges and their echoes return at different times giving rise to a time-varying clutter component in the received signal. The total dynamic range of this return signal may be as large as 70 db although intelligent use of sensitivity-time-control (S.T.C.) may reduce this further. If in simple MTI circuits the dynamic range of the pulse-compression or MTI circuit is less than the dynamic range of the return some limiting of the return will undoubtedly occur, either by design or by chance.

Linear-limiting amplifiers [42] are sometimes desireable in pulse-compression MTI to reduce the residues of the canceller to the noise level on the MTI display. Adjustable limiting amplifiers may be used both preceding the compression network and preceding the MTI canceller to control the false alarm rate at the display [60].

From these considerations we conclude that many pulse-compression MTI radars would include limiters.

5.2 Review of Literature on the Effect of Limiters

Limiters and logarithmic amplifiers used at the intermediate frequency are two circuits which are used to reduce the dynamic range of the return. We shall be concerned principally with the effect of a linear-limiting amplifier in pulse-compression systems. By a linear-limiting amplifier we mean a circuit which is linear up to a certain input level A and which saturates completely for any input levels exceeding the level A.

The earlier literature [43-49] details the effect on signal-to-noise ratio of a hard limiter in a narrow-band system. These studies are reviewed for completeness but are not directly applicable to the case of pulse-compression.

Strictly speaking the objective in radar signal processing is to increase signal detectability. This detectability is determined by the input SNR to the detector. Thus SNR is a basic measure of detectability. However the SNR may vary widely depending at which point in the system it is measured and what the noise bandwidth is at that point. The best possible measurement of the SNR is made by passing the noisy signal through a matched filter so that all the energy in the signal is reduced to one dimension or sample. After matched filtering the SNR depends only on $R = 2E/N_o$ which was discussed in Chapter 3. Therefore in what follows we shall use the SNR after a matched filter.

Davenport [43] has rigorously analyzed the effect of a band-pass limiter on a sinusoid buried in narrow-band Gaussian

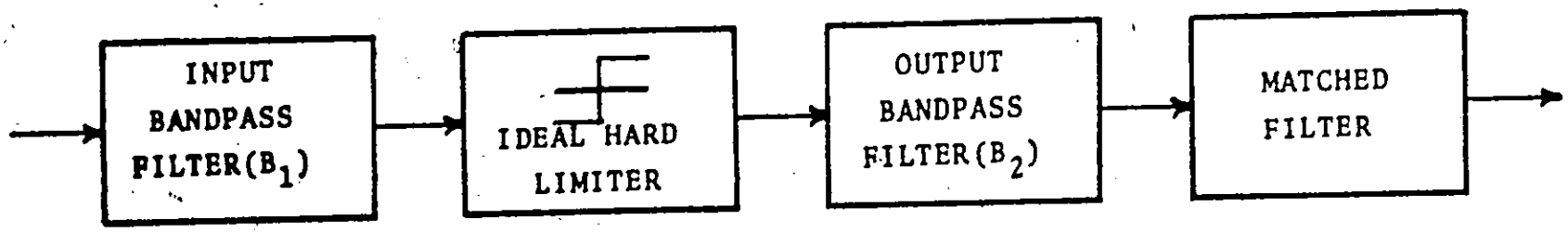

figure 51. The Band-Pass Hard-Limiter Mathematical Model. The Input is a Sinusoid plus Narrow-Band Gaussian Noise.

noise centered on the carrier frequency of the sinusoid. A block diagram of the system is shown in Fig. 51. The filter with bandwidth B_2 was assumed to be a narrow rectangular pass-band centered at the carrier frequency. As the input signal-to-noise ratio (SNR) approaches zero the output SNR approaches $\pi/4$ times the input SNR for a maximum loss of 1.0 db compared to a linear system.

Manasse, Price and Lerner [44] showed that when the bandwidth of the Gaussian noise was made wider than the bandwidth of the sinusoidal signal the loss in signal energy with respect to the noise could be reduced to zero. A number of different wideband noise spectra were examined and values of $A = \frac{(E/N_o)_{IN}}{(E/N_o)_{OUT}}$ from 1.059 to 1.12 were calculated yielding a SNR loss of approximately 0.5 db. For signal and noise of equal bandwidth the loss in SNR was 0.6 db.

Cahn [45] has generalized these studies of narrow-band signals in band-pass limiters by considering the concept of antisymmetric sidebands. If the desired signal was small compared to the noise then the sine wave may be considered to be a modulation of the noise carrier. Since the ideal band-pass limiter suppresses amplitude information produced by symmetrical sidebands only, the phase information produced by anti-symmetrical sidebands is retained. Using this concept Cahn shows the loss in signal-to-noise energy as a function of signal-to-noise bandwidth which is reproduced here as Fig. 52. The 1 db loss of Davenport is approached in Fig. 52 as the noise bandwidth decreases, while the 0.6 db loss of Manasse, et al is shown for

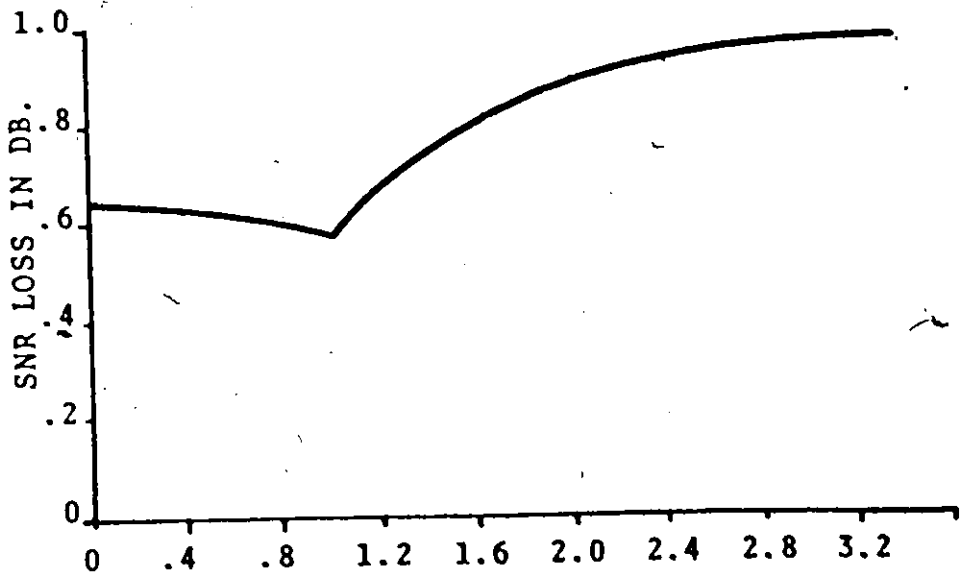

figure 52. Signal-To-Noise Ratio (SNR) Loss Due to a Hard Limiter [Cahn [45]].

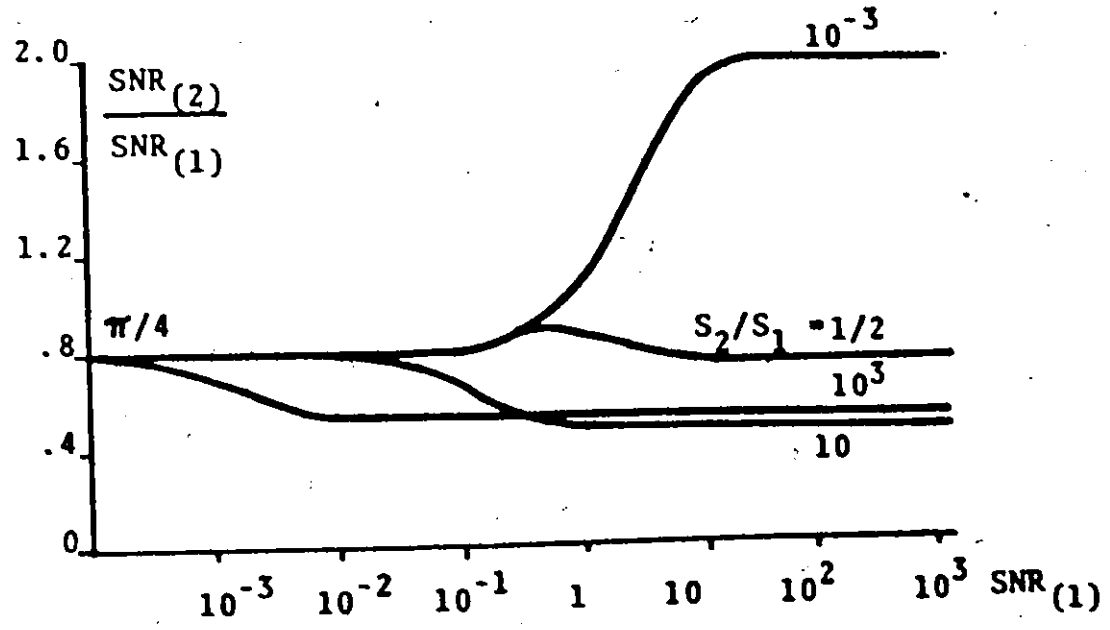

figure 53. The Ratio of the SNR of the Desired Signal ($SNR_{(2)}$) to the SNR of the Interfering Signal ($SNR_{(1)}$) for the Hard Band-Pass Limiter. S_2/S_1 is their Energy Ratio. [Jones[46]].

signal and noise of equal bandwidth.

Jones [46] considers two sinusoids and narrow-band Gaussian noise which are passed through an ideal band-pass limiter. In this case there is an interference between the desired signal (one sinusoid) and the interference (the other). This loss is indicated for the smaller signal in Fig. 53. For very low input SNR the curves of Jones agree with the $\pi/4$ ratio between output and input energy as calculated by Davenport. At high input SNR, a SNR gain by a factor of two is shown for the strong signal and a decrease by the factor 1/2 is shown in Fig. 53 for the weak signal. The factor 1/2 implies a loss in SNR for the weak signal of 3 db when the strong signal captures the limiter.

This capture effect is well known in FM theory [47]. From Fig. 53 we can see at high SNR the larger signal predominates over the smaller signal so that the signal-to-signal power ratio at the output is 1/4 of the input ratio.

Although Jones claims that these results have application to pulse-compression radar where two close together echoing reflectors produce substantial pulse overlaps, it must be stated that his results apply only for constant amplitude continuous waves of different frequency.

Lyons [48] has studied the effect of a hard-limiting satellite repeater on the signal to interference ratio of narrowband signals. Many sinusoidal signals are considered to enter the repeater and they suppress the power of the desired signal. The suppression factor of the desired signal is indicated

for various combinations of interferring signals.

The only work which applies specifically to pulse-compression systems is that of Bogotch and Cook [1]. In their limiter tests the bandwidth of the filters B_1 and B_2 in Fig. 51 were equal to the frequency deviation of the chirp signal used. They considered the partial time coincidence of two returns where the IF limiter was set to limit at or below the root-mean-square (RMS) noise level. The weaker desired signal was divided into two regions coincident and non-coincident with the strong interferring return. In the coincident part the interferring signal suppressed both the desired signal and the noise. The action of the matched filter on the attenuated section of length T_p of the noise, was to spread the noise attenuation over an interval $2\ T_p$ wide. The noise trough and four degrees of overlap of the desired return are shown in Fig. 54.

Bogotch and Cook found that the amplitude of the desired signal was reduced in a linear manner with overlap. This is shown in Fig. 55.

The noise was approximated by m samples over the interval T_p of the signal duration. They state that at the edge of the noise trough at the output of the matched filter the RMS noise builds up as $\sqrt{m}$ which leads to the conclusion that the mean square noise builds up as m, the number of noise samples in the clear.

From these two statements about the desired signal and the noise in the noise trough a loss in SNR for the desired signal is implicit. However Bogotch and Cook measured the

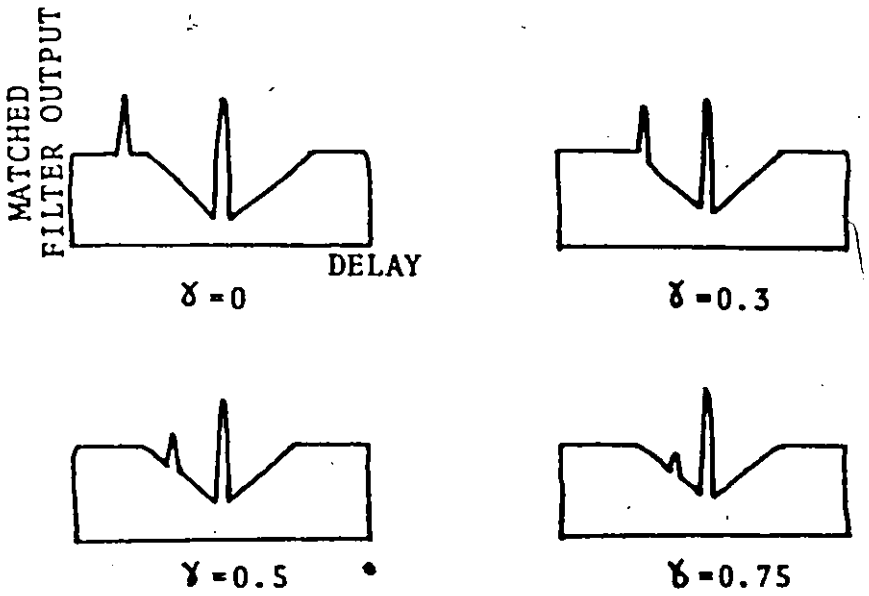

figure 54. Matched Filter Outputs Illustrating Weak Signal Suppression for Different Overlap Factors γ, as a Small Target Moves into a Large Interference. [Bogotch and Cook [1]].

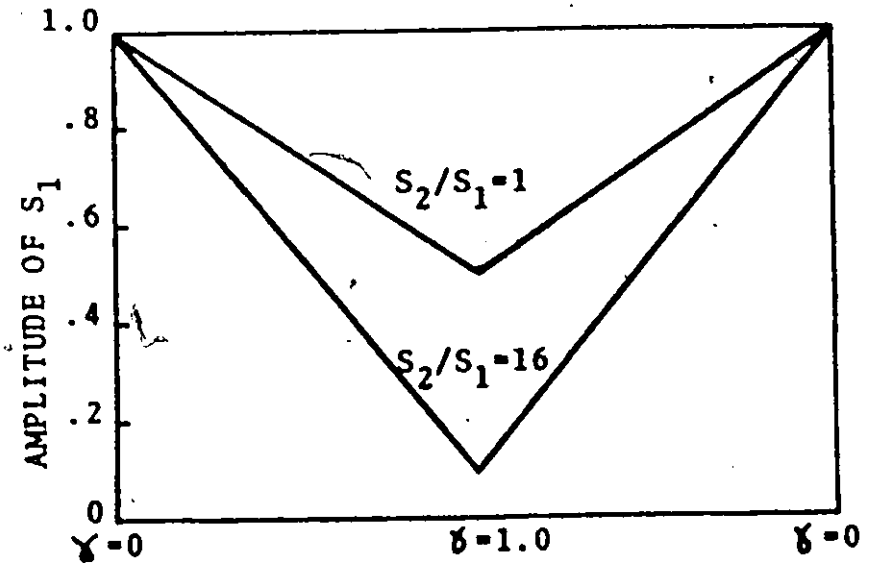

figure 55. The Amplitude of the Weaker Signal† Versus Overlap Factor γ, as a Smaller Signal Moves Into A Large Interfering Signal. S_2/S_1 is the Ratio of the Interference to Weak Signal Energy. [Bogotch and Cook [1]] †(after matched filtering)

probability of detection after a fixed threshold following the matched filter. Because of the variable signal and noise attenuation of the captured limiter this fixed threshold becomes an effectively variable threshold which depends on the strength of the interferring signal. In the noise trough this fixed threshold is equivalent to a higher threshold and consequently the probability of detection and the probability of false alarm fall drastically. The probability of detection is shown versus interference energy and limiter level. They showed that to achieve a given probability of detection an increase in SNR of 1-2 db above a linear system was required for limiting of 0 and 40 db below the RMS noise.

Zeoli [37] has considered a two channel coherent digital signal processor where the video limiting is that of the analog-to-digital converters, occurring separately in each channel. Intermediate frequency (IF) limiting and video limiting are compared and it was found that when the input is a narrow-band random signal, video limiting gives about 1 db greater SNR loss compared to IF limiting.

An excellent summary of limiter effects and an extensive bibliography is available in a recent book by Nathanson [49]. However results which apply specifically to pulse-compression radar in a clutter environment are not available. From Davenport one might conclude that the signal-to-noise ratio loss is small. For narrowband signals and noise this is the case. Jones deals with the interference problem of two sinusoids in noise. When one sinusoid is much larger than the desired signal and the noise,

the desired signal suffers 3 db signal-to-noise ratio loss in a hard-limiter. However the case of wideband pulse-compression signals must be treated differently from the work of Jones. Particularly when strong clutter captures the system limiting IF amplifier and attenuates a partially overlapping desired return, large signal-to-noise ratio losses will be shown in this thesis, much larger than might be obtained by extrapolating previous work.

Chapter 6

Formulation of the Problem of Envelope Limiting in Pulse-Compression MTI Radar Systems

This chapter details the formulation of the theory and the simulation of the effect of an envelope limiter in pulse-compression moving target indicator (MTI) radar. The limiter is linear up to a threshold A and saturates for inputs greater than A. In the theoretical analysis the clutter is idealised to be fixed and to have a much larger amplitude than the target return and the limiter threshold A. An equation for the signal-to-noise ratio is developed which applies when the strong clutter captures the system's IF envelope limiter and attenuates a partially overlapping desired target return. A computer simulation is developed to confirm the theory and to provide new results on this difficult nonlinear problem. Several cases are examined with different clutter types and different transmit signals. The results of these simulations are the subject of the next chapter.

6.1 Theory of Envelope Limiting in Pulse-Compression MTI Radar

The pulse-compression MTI radar is represented by the block schematic shown in Fig. 56. The returning echo, clutter and thermal noise components enter a wide band-pass filter followed by a linear-limiting amplifier which is linear up to a threshold A and limits above A. The limited signals plus noise

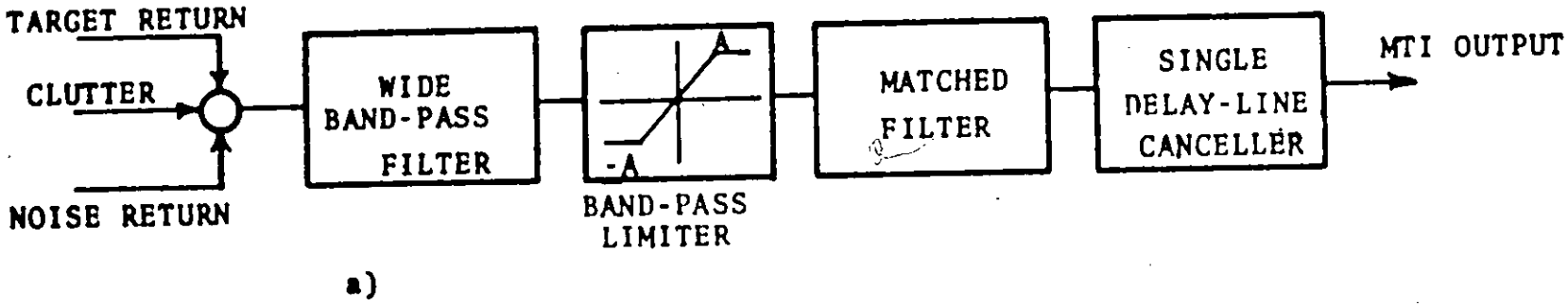

a)

b)

figure 56. Block Diagram [illegible] the Mathematical Model a) Block Diagram Including b) The Single Delay-Line Canceller

are matched filtered by convolution with the time-reversed transmitted pulse and the successive differences in this compressed output are taken by the single delay-line canceller. The intention is to calculate the MTI output target-to-noise energy ratio and compare it with the target-to-noise energy ratio without limiting.

The threshold A of the envelope limiter is chosen such that the target return plus noise will normally remain within the linear region. Thus when the clutter return is negligible the limiter has no effect. However a strong clutter return is assumed to exceed the limiter threshold A by a considerable amount. If the clutter exceeds A by a large amount then the clutter captures the limiter and the circuit behaves linearly with respect to the target and noise returns and they are attenuated. This attenuation is strongly time-varying and depends on the instantaneous amplitude and phase of the capturing clutter.

It is assumed that all the signals are band-pass functions with an arbitrary carrier frequency $\omega/2\pi$. We may describe the target return clutter, and noise returns by their complex envelopes r(t), c(t) and n(t) respectively.

Thus $r(t)\, e^{j\omega t}$, etc., are pre-envelope functions [39] and we may write:

$$\text{target return} = \text{Re}\{\, r(t)\, e^{j\omega t + j\alpha'}\} \tag{66}$$

$$\text{clutter return} = \text{Re}\{\, c(t)\, e^{j\omega t}\} \tag{67}$$

$$\text{noise} = \text{Re}\{\, n(t)\, e^{j\omega t}\} \tag{68}$$

where the angle α' is a measure of the arrival time of the target return with reference to the clutter return. We may graphically illustrate the effect of the envelope limiter on the sum of the three pre-envelope signals as shown in Fig. 57. Suitable zonal filtering after the limiter is normally available in the circuit, for example, in the matched filter. The limiter output may be written as a bandpass function equal to Re $\{y(t)\, e^{j\omega t}\}$ with $y(t)$ defined as follows:

a) when $\quad |c(t) + r(t)\, e^{j\alpha'} + n(t)| \lesssim A,$ (69)

$$y(t) = c(t) + r(t)\, e^{j\alpha'} + n(t)$$

b) when $\quad |c(t) + r(t)\, e^{j\alpha'} + n(t)| > A$

$$y(t) = A\, \frac{c(t) + r(t)\, e^{j\alpha'} + n(t)}{|c(t) + r(t)\, e^{j\alpha'} + n(t)|} \tag{70}$$

$$= A \cdot \frac{c(t)}{|c(t)|} \cdot \frac{1 + z(t)}{|1 + z(t)|}$$

where a new auxiliary function $z(t)$ is introduced:

$$z(t) = \frac{r(t)\, e^{j\alpha'} + n(t)}{c(t)} \tag{71}$$

Regardless whether or not capture of the limiter by clutter occurs, the following condition is satisfied:

$$|r(t)\, e^{j\alpha'} + n(t)| \ll A \tag{72}$$

and when clutter occurs, $|c(t)| > A$. The right hand side of Equation (70) may be interpreted as the product of three terms: A, a unit vector with a phase angle equal to that of c(t), and a unit vector with a phase angle equal to that of $1 + z(t)$. We may approximate $\frac{1 + z(t)}{|1 + z(t)|}$ by the imaginary part of z(t) as shown in Fig. 58. From Equation (71) and with inspection of Fig. 57 we can see that z(t) is the portion of y(t) that is due to the target plus noise after passing through the captured limiter. We see that y(t) is approximately made up of the limited clutter and the projections of target and noise perpendicular to that clutter. Thus we rewrite Equation (70) as follows:

$$y(t) \doteq A \frac{c(t)}{|c(t)|} [1 + j \text{ Im } (z(t))] \tag{73}$$

Equation (73) together with Equation (71) indicates that in the captured region where $|c(t)| >> A$, the limiter output y(t) is approximately a linear function of r(t) and n(t), with a time-varying attenuation provided by the factor 1/c(t), unless c(t) is constant.

The signal $y(t)\, e^{j\omega t}$ as defined by Equation (73) is next passed through a filter matched to r(t) and then through a single delay-line canceller. Since both the matched filter and the delay-line canceller are time-invariant linear circuits, the order in which they are connected can be reversed without changing the output. This will be done to simplify the theory.

In a fixed clutter situation the clutter repeats after a time T_R equal to the pulse repetition period. The target return repeats except for a phase shift of say, 2θ due to Doppler.

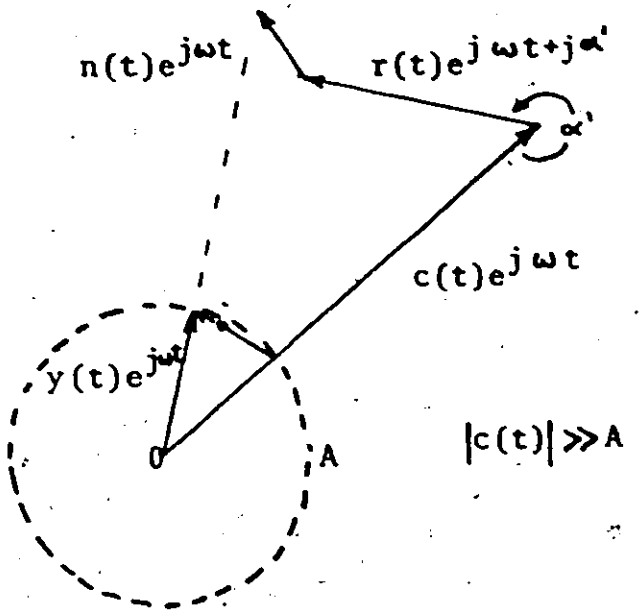

figure 57. Envelope Limiting of the Clutter, Signal, and Noise Returns.

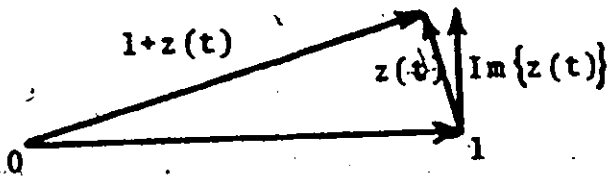

figure 58. The Approximation of the Phase of $\frac{1+z(t)}{|1+z(t)|}$ by $\mathrm{Im}\{z(t)\}$.

The random variables $n(t)$ and $n(t + T_R)$, corresponding to the values of the noise components on two successive pulses, are independently selected from one ensemble which is assumed to be sufficiently wide-band and Gaussian. Thus we may write,

$$c(t + T_R) = c(t) \tag{74}$$

$$r(t + T_R) = r(t)\, e^{j2\beta} \tag{75}$$

$$n(t + T_R) - n(t) = j\sqrt{2}\, n_1(t) \tag{76}$$

From Equations (74), (75) and (76) the assumptions regarding the statistics of signal and noise can be seen. The clutter return on any two successive pulses is identical and the target echo is identical in amplitude but changes phase by 2β. The complex noise envelope $n(t)$ is assumed to be independent from pulse to pulse and hence in Equation (76) the two noises have been replaced by one noise with the same energy. On the right hand side of Equation (76) the 90 degree phase shift of the term j is introduced for convenience. This can be done without altering the statistics of the noise because the noise has uniformly distributed phase. The intention is to subtract the two successive returns and then perform matched filtering.

From Equations (71), (73) - (76) one can form the return difference called $\Delta(t)$:

$$\Delta(t) = y(t + T_R) - y(t) \tag{77}$$

$$= Aj \frac{c(t)}{|c(t)|} \operatorname{Im}\left(\frac{r(t+T_R)e^{j\alpha'} - r(t)e^{j\alpha'} + n(t+T_R) - n(t)}{c(t)} \right)$$

$$= Aj \frac{c(t)}{|c(t)|} \text{Im} \left\{ \frac{r(t)e^{j(\alpha'+\beta)} \cdot 2j\sin\beta + j\sqrt{2}n_1(t)}{c(t)} \right\}$$

For convenience we will drop the subscript from $n_1(t)$ and write $\alpha = \alpha' + \beta$ so that:

$$\Delta(t) = Aj \frac{c(t)}{|c(t)|} \left[2 \sin\beta \, \text{Re} \left\{ \frac{r(t)e^{j\alpha}}{c(t)} \right\} + \sqrt{2} \, \text{Re} \left\{ \frac{n(t)}{c(t)} \right\} \right] \tag{78}$$

The matched filter operates linearly on $\Delta(t)$ to compress the signal and it forms the cross-correlation $\rho_{\Delta r}(\tau)$ which in this theory is the single delay-line canceller MTI output. After both cancelling and matched filtering we obtain:

$$\rho_{\Delta r}(\tau) = \int_{-\infty}^{\infty} \Delta(t) \, r^* (t + \tau) \, dt \tag{79}$$

where the asterisk denotes complex conjugation.

The compression operation reduces the long time sequence to a short autocorrelation function and the position and height of the central peak indicates the range and strength, respectively, of the target. In distributed fixed clutter the distortion introduced by the limiter and the additive contribution of the many sidelobes of the clutter tend to reduce the peak to sidelobe ratio in the MTI output even when complete cancellation of fixed clutter occurs. It is meaningless to consider clutter levels so high that the distorted compressed target output has

higher sidelobes than the central peak. Care was taken in the simulation to maintain clutter levels below this extreme case. Since we are interested principally in the main peak of the compressed output we need only consider $\tau = 0$ in Equation (79).* Let the peak value of the compressed output be $P(\alpha)$ for a given arrival angle α.

$$P(\alpha) = \rho_{\Delta r}(0) = \int_{-\infty}^{\infty} \Delta(t)\ r^*(t)\ dt \tag{80}$$

Substituting Equation (78) into (80) we get:

$$P(\alpha) = A \int_{-\infty}^{\infty} j \frac{c(t)}{|c(t)|} \left[2 \sin\beta\ \mathrm{Re}\left\{\frac{r(t)}{c(t)}\ e^{j\alpha}\right\} + \sqrt{2}\ \mathrm{Re}\left\{\frac{n(t)}{c(t)}\right\}\right] r^*(t)\ dt \tag{81}$$

The noise term in Equation (81) is needed only to calculate the variance of $P(\alpha)$. We may therefore rewrite Equation (81) with $\sqrt{2}\ \mathrm{Re}\left\{\frac{n(t)}{c(t)}\right\}$ replaced by another noise term $\frac{n(t)}{c(t)}$ having the same variance so that Equation (81) simplifies to:

$$P(\alpha) = 2jA \sin\beta \int_{-\infty}^{\infty} \frac{c(t)}{|c(t)|}\ r^*(t)\ \mathrm{Re}\left\{\frac{r(t)}{c(t)}\ e^{j\alpha}\right\} dt + jA \int_{-\infty}^{\infty} \frac{n(t)}{|c(t)|}\ r^*(t)\ dt \tag{82}$$

* The sidelobes are neglected in this step. In practice they may degrade the output SNR.

However:

$$\mathrm{Re}\left\{\frac{r(t)}{c(t)}\ e^{j\alpha}\right\} = \frac{1}{2}\ \left[\frac{r(t)}{c(t)}\ e^{j\alpha} + \frac{r^*(t)}{c^*(t)}\ e^{-j\alpha}\right]$$

$$= \frac{r(t)}{2\ c(t)}\ e^{j\alpha}\ \left[1 + e^{-2j(\phi(t)\ +\ \alpha)}\right] \tag{83}$$

where $\phi(t)$ is the angle of $\frac{r(t)}{c(t)}$.

Substituting Equation (83) into (82):

$$P(\alpha) = je^{j\alpha}\ \sin\beta \int_{-\infty}^{\infty} \frac{A}{|c(t)|}\ \left[1 + e^{-2j(\phi(t)\ +\ \alpha)}\right]\ |r(t)|^2 dt$$

$$+\ jA \int_{-\infty}^{\infty} \frac{n(t)}{|c(t)|}\ r^*(t)\ dt\ ,\quad |c(t)| >> A \tag{84}$$

This equation applies only for the captured region where the clutter exceeds the limit level A.

Another relation is needed to describe the target output in the clear region where $|c(t)| < A$. For this case the difference between two successive returns is, from Equations (69) and (74) - (76),

$$\Delta(t) = j\ 2e^{j\alpha}\ r(t)\ \sin\beta + j\ \sqrt{2}\ n(t) \tag{85}$$

The corresponding MTI peak output after matched filtering is:

$$P(\alpha) = j2e^{j\alpha}\ \sin\beta \int_{-\infty}^{\infty} |r(t)|^2\ dt + j\ \sqrt{2} \int_{-\infty}^{\infty} n(t)\ r^*(t)\ dt \tag{86}$$

The notable similarity of Equations (84) and (86) which apply to the captured and clear regions respectively, reemphasizes the fact that the strong clutter linearizes the captured-limiter with respect to the target return and noise components. It also suggests that the equations are amenable to being combined into one general equation by introducing two appropriate time-varying attenuation factors.

Define $g(t,\alpha)$ and $h(t)$ as follows:

$$g(t,\alpha) = \begin{cases} \frac{A}{2|c(t)|}\left[1 + e^{-2j(\phi(t)+\alpha)}\right], & |c(t)| >> A \\ 1 & |c(t)| \leq A \end{cases} \tag{87}$$

$$h(t) \begin{cases} \frac{A}{\sqrt{2}|c(t)|} & |c(t)| >> A \\ 1 & |c(t)| \leq A \end{cases} \tag{88}$$

Then Equation (84) for the case of the captured-limiter and Equation (86) for the case of the target in a clear clutter free region, may be combined into one equation as follows:

$$P(\alpha) = j\, 2\, e^{j\alpha} \sin\beta \int_{-\infty}^{\infty} g(t,\alpha)\ |r(t)|^2\, dt + j\sqrt{2} \int_{-\infty}^{\infty} n(t)\, h(t)\, r^*(t)\, dt \tag{89}$$

Equation (89) is valid if during the interval for which $|r(t)| \neq 0$ the target is either in the clear or in the captured region. The approximation of Equation (73) requires $|c(t)| >> A$ in the captured region. Therefore Equation (89) is valid only for weak or very strong clutter and is only approximate where $|c(t)| \doteq A$. However where discrete sources of clutter generate either no clutter component or a very strong clutter component then Equation (89) helps to give insight into the effect of the time-varying attenuation caused by the clutter-captured limiter.

6.1.1 The Mean and Variance of the Target Output P (α)

The mean of P(α) is the average target amplitude. The variance of P(α) is equal to the energy of the noise component of P(α). P(α) is a random variable defined by Equation (89). Assuming that the Gaussian noise component n(t) is zero mean we may take the expected value of P(α) as:

$$\bar{P} = E\{P(\alpha)\} = j\ 2\ e^{j\alpha} \sin\beta \int_{-\infty}^{\infty} g(t,\alpha)\ |r(t)|^2\ dt \qquad (90)$$

This mean value* in time is still a function of the time of arrival angle α and the Doppler angle β. Subtracting Equation (90) from (89),

$$P(\alpha) - \bar{P} = \sqrt{2}\ j \int_{-\infty}^{\infty} n(t)\ h(t)\ r^{a}(t)\ dt \qquad (91)$$

* P(α) is conditioned on $|c(t)|$ through $g(t,\alpha)$.

The variance of the complex P(α) is given by [59]:

$$V = E\{|P(\alpha) - \bar{P}|^2\} \tag{92}$$

$$= 2\int_{-\infty}^{\infty}\int_{-\infty}^{\infty} E\{n(t)\, n^*(t+\tau)\}\, h(t)\, h^*(t+\tau)\, r(t)\, r^*(t+\tau)\, d\tau\, dt$$

Define $x = t + \tau$ and $R_N(\tau) = E\{n(t)\, n^*(t+\tau)\}$ so that:

$$V = 2\int_{-\infty}^{\infty}\int_{-\infty}^{\infty} R_N(t-x)\, h(t)\, h^*(x)\, r(t)\, r^*(x)\, dx\, dt \tag{93}$$

There are two special cases to consider depending on the bandwidth of the noise,

a) If the noise component n(t) is white, $R_N(t-x) = N_o\, \delta(t-x)$, where $\delta(t-x)$ is a unit impulse located at $t = x$. Thus Equation (93) reduces to:

$$V = 2\, N_o \int_{-\infty}^{\infty} |h(t)|^2\, |r(t)|^2\, dt \tag{94}$$

b) If n(t) is first band-pass filtered, the evaluation of V is a bit more tedious. As an example consider a Barker 13 code of length L in infinite clutter. Assume r(t) is real and zero outside the interval from 0 to L, and that the clutter suppresses a portion of the target return from T to L in Fig. 59.

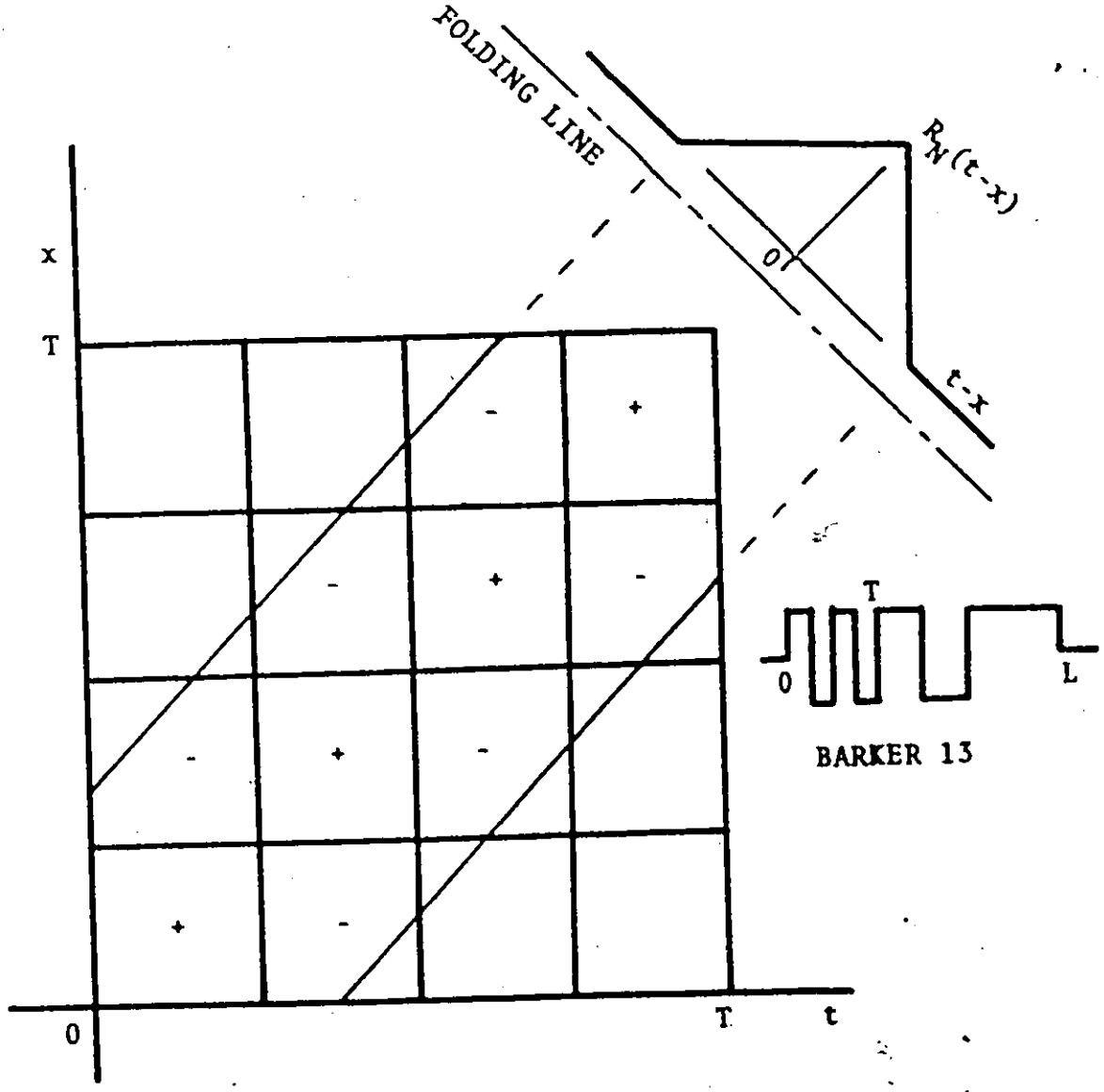

figure 59. The Calculation of V_{INF} by Equation (95). The First Four Bits of the Barker 13 are in the Clear and the Remainder of the Barker 13 is Attenuated by Infinite Amplitude Clutter.

Then from Equation (93) we get:

$$V_{INF} = 2 \int_0^T \int_0^T R_N(t-x)\ r(t)\ r(x)\ dx\ dt \qquad (95)$$

Assume that the code r(x) is made up of + 1's and -1's and that R_N is triangular and zero for t-x greater than the subpulse length. Fig. 59 shows a graphical evaluation method for V_{INF} for T equal to four subpulses. Values of V_{INF} calculated in this way will be used later to confirm simulation results.

In Fig. 59 the code is written as a sequence of plus and minus intervals along two dimensions. The autocorrelation function of the noise is visualized as a "roof" which passes down the diagonal of the two dimensional plane. Equation (95) then can be interpreted as the volume under the noise autocorrelation function. In calculating the total volume the sign of the checkerboard pattern of pluses and minuses on the plane of the code must be considered.

6.1.2 The Output Target SNR Equation

Having calculated the mean and variance of the target peak P (α) at the output of the pulse-compression MTI circuit we may write the target signal-to-noise energy ratio (SNR) denoted as λ and defined by:

$$\lambda = \frac{\bar{P}^2}{V} \frac{\left[j\ 2\ e^{j\alpha} \sin\beta \int g(t,\alpha)\ |r(t)|^2\ dt\right]^2}{2 \iint R_N(t-x)\ h(t)\ h^*(x)\ r(t)\ r^*(x)\ dx\ dt} \qquad (96)$$

λ is a function of α, β and in particular of $|c(t)|^{-1}$ through $g(t,\alpha)$ and $h(t)$ as defined in Equations (87) and (88).

When $c(t) < A$ in the clutter free region, $g(t,\alpha) = h(t) = 1$; the corresponding maximum value of λ is useful as a reference since it represents the SNR of a linear system without any limiter. Any degradation from this maximum value of λ is attributed to the limiter.

The application of the SNR equation for the cluttered region where $|c(t)| >> A$ will be left to the next chapter on results. Several different cases will be examined and the simulation and theory compared. These cases will include single strong clutter reflectors, distributed clutter reflectors and clusters of clutter reflectors.

6.2 Digital Computer Simulation

The difficulty of analyzing the behaviour of nonlinear systems suggests that a computer simulation of the system may be useful to support derived results and to provide new data. In this section we shall use digital computer simulation to study the SNR in a clutter-captured limiter under various conditions.

In order to make the computer simulation meaningful and as close to the mathematical analysis as possible, complex numbers were used in the simulation and signals were thus represented in pre-envelope form. This requires a two channel video simulation in which in-phase and quadrature components can be recognized and displayed by two digital-to-analog converters

and a dual-beam oscilloscope.

A 16 bit fixed-point computer (CDC 1700) with oscilloscope display was used to average and display the data. Integer numbers occupying one 16 bit computer memory word were used to represent one sample of one channel of the signal. These integer samples were considered to span the integers from - 32,767 to 32,767. Thus one complex sample with a real or in-phase component and an imaginary or quadrature component uses two computer words. A complex low-pass envelope such as n(t) was represented by an array of 1024 complex samples spanning 2048 16 bit computer words. A transmit signal such as a Barker 13 phase reveral coded pulse was represented by, say, 78 complex samples with a magnitude of $\pm$ 8000 so that each subpulse of the code is represented by six complex samples spanning 12 computer words. For the purpose of cross-correlation with 1024 complex echo samples the transmit signal was augmented with zeros to fill a 1024 complex sample array. Convolution and correlation were performed between two integer arrays of 1024 complex samples by using a fast Fourier transform (FFT) subroutine. Conditional array scaling [22] was included in the FFT to prevent numerical overflow at intermediate steps of the computation. The forward FFT converts an integer array of say 1024 complex time values into an equal length array of complex frequency components. The use of an inverse FFT reverses this operation. Thus cross-correlation can be performed on two time sequences or arrays, of equal length, by applying a forward FFT on each input array.

Then at each discrete frequency the product of the two resultant spectra is calculated. These products must also be scaled down to prevent exceeding the available bit length. Thus an array of discrete frequency cross-power components results, the inverse FFT of which is the circular cross-correlation of the two input time sequences†.

Three kinds of clutter were simulated to test the effect of the clutter-captured limiter on the target signal-to-noise ratio. The clutter types considered were: single clutter, i.e., produced by one strong point scatterer, distributed clutter produced by a field of scatterers; and clusters of clutter produced by groups of scatterers clustered at some particular ranges. These clutter types were considered for both fixed and fluctuating scatterers.

A universal method was used to generate the simulated clutter signal. This method was applicable to each of the clutter types and could be used for any transmit waveform. A range space array composed of 1024 complex sample range bins was filled with zeros and a complex impulse represented by two adjacent computer words was placed at each location in range where a reflector was simulated. The magnitude and phase of each impluse would determine the amplitude and phase of the corresponding clutter return. Thus we may write:

---

† See Chapter 2, section 2.5, this thesis.

$$c(t) = r(t) * \sum_{K}^{K} A_K \, \delta(t+\tau_K) = \sum_{K}^{K} A_K \, r(t+\tau_K) \qquad (97)$$

where τ_K is the range of the reflector and the asterisk denotes convolution. Since the time sequences are sampled we must replace c(t) by $C(\ell t) = C(\ell)$ where ℓ is an integer so that Equation (97) becomes:

$$C(\ell) = r(\ell) * \sum_{K}^{K} A_K \, \delta(\ell+k) = \sum_{K}^{K} A_K \, r(\ell+k) \qquad (98)$$

where $0 \leq \ell \leq N$ with N = 1024 and k locates the reflector.

Provided that there are no reflectors in some range of length equal to the length of the transmit signal, then the clutter signal $C(\ell)$ defined in Equation (98) will be zero for some ℓ and no aliasing of the clutter signals, due to the circular convolution used, will be encountered. The range for which $C(\ell) = 0$ is free of clutter, and in this region the linear-limiting amplifier does not saturate.

The target was included in the range space of the clutter reflectors. For each simulated transmitter pulse the convolution of Equation (98) was performed and the summation of echos was the clutter plus target for that transmitter pulse. A second convolution with an altered target phase produced the effect of fixed clutter and a moving target. By altering the clutter reflectors by a small amount on each transmit pulse fluctuating clutter could also be simulated. A block diagram of the video simulation is shown in Fig. 60.

The envelope limiter was simulated on the computer by testing the magnitude of each complex input sample against a

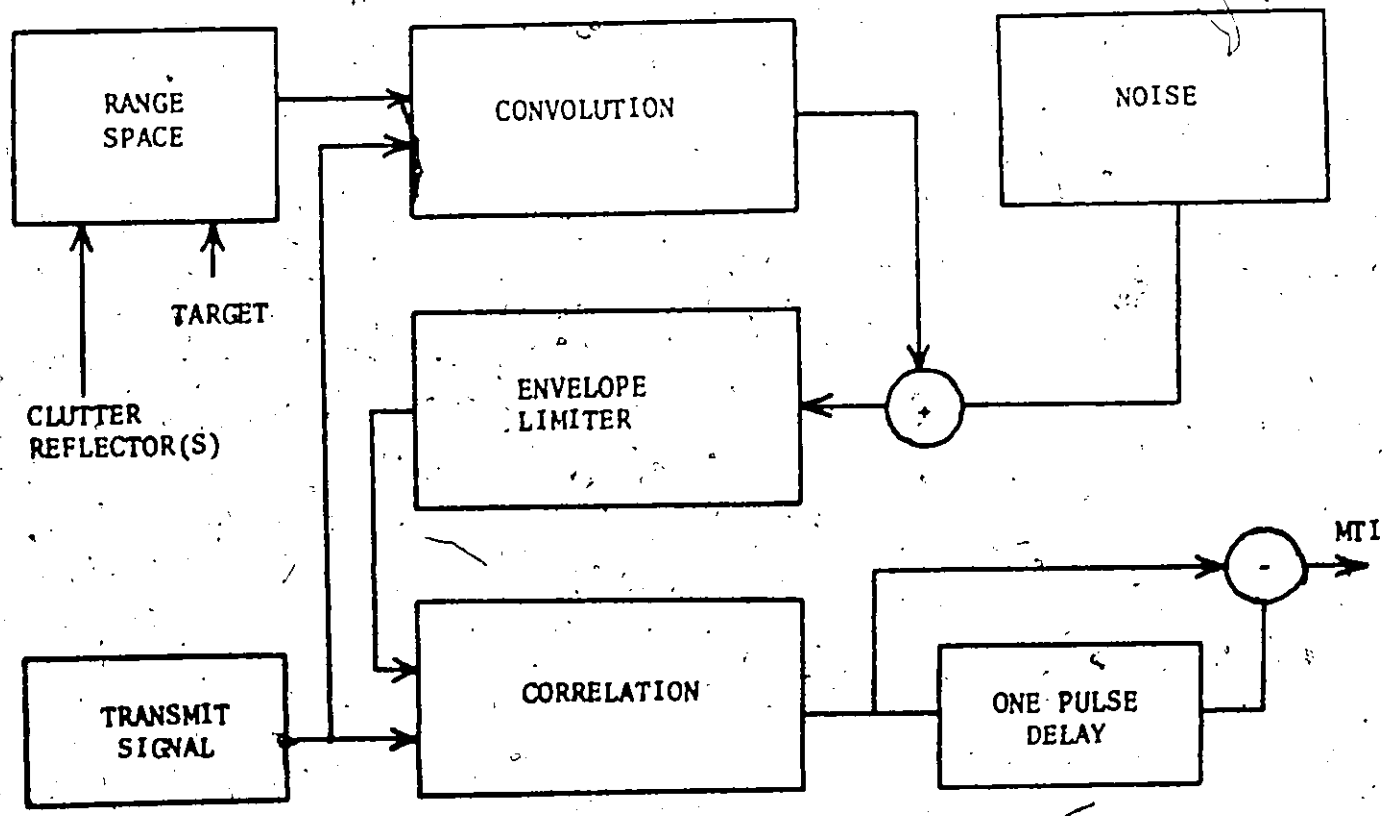

figure 60. MTI COMPUTER SIMULATION BLOCK DIAGRAM

threshold A. If the magnitude was less than A the two computer words holding the complex sample were not altered. If the magnitude of the complex sample was greater than A then each word holding the complex sample components was divided by that magnitude and multiplied by A so that the output magnitude was equal to A.

This scaling could be performed using a floating point package which gave the required accuracy, but limiting 1024 complex points by floating point methods required two seconds of computer time. Instead a fixed-point method using double-precision integers was used to give the required accuracy but take only 0.2 seconds for 1024 complex input points.

White Gaussian noise was obtained by analog-to-digital conversion to 14 bit accuracy of the noise output of a random analog noise generator. This method of generating noise was fast and convenient and had the advantage over computer generated sequences that the sequence never repeated. However computer generated sequences do have the advantage that experiments can be repeated with identical signals using different system parameters.

Band-limited colored wide-band Gaussian noise was obtained by adding white noise samples together in groups of 6 samples. By sliding the elements of the group one sample down the sequence at a time, a sliding sum with a triangular auto-correlation function was produced. By making the width of this autocorrelation function the same as the width of the auto-correlation function of the transmit signal, the colored noise

could be made to have the same bandwidth as the signal. Henceforth the word "colored" as applied to noise will indicate noise with the same spectrum as the signal.

Before envelope limiting the noise was added to the clutter plus target signals. The limit level was set to limit the clutter strongly but not to limit the target plus noise alone. This implies a limit level in integer form of about 1000 and a clutter level of 6,500 with target plus noise below 1000; thus clutter is 16 db into limiting.

The matched filtering was executed similarly to the convolution, using two forward FFT's and one inverse FFT on their spectral product with the transmitter signal first time-reversed. This reversal makes cross-correlation identical to convolution with the time-reversed transmitter signal. The output of the matched filter had in-phase and quadrature components which were stored for coherent MTI cancellation. After coherent subtraction of two successive matched filter outputs the in-phase and quadrature channels were combined by squaring and adding them, and taking the square root.

6.3 Simulated Experiments

The following is a list and detailed account of a series of simulations which were made with different transmit signals and clutter types to determine the effect of a clutter-captured limiter on the target signal-to-noise ratio at the MTI output. Both a) fixed reflectors and b) fluctuating reflectors are considered as sources of clutter.

a) Fixed Clutter

i) A comparison between the Barker 13 phase-reversed code and an uncoded pulse of the same length in strong single clutter.

ii) A 63 bit random code in white noise and strong clutter.

iii) Barker 13 in distributed clutter.

iv) Barker 13 in clusters of clutter.

b) Fluctuating Clutter

v) Barker 13 in strong single clutter.

vi) Barker 13 in clusters of clutter.

6.3.1 Details of the Simulated Experiments

Since strong clutter captures the envelope limiter and attenuates both signal and noise in a linear fashion it was possible and convenient to measure their energies separately and to obtain the resultant signal-to-noise ratio at the MTI output by division of those energies.

To obtain the noise energy versus range both in the clear and in clutter a large number of MTI outputs with no target were squared and summed using independent noise in each channel for each transmitter pulse.

The target was moved from outside the clutter through those ranges at which clutter was located and the largest peak of the MTI output was tracked and its amplitude was plotted.

i) A Comparison between the Barker 13 Phase-Reversal Code and an Uncoded Pulse of the same Length in Strong Single Fixed Clutter

The uncoded pulse and the Barker 13 coded pulse were made 78 complex samples long and were augmented by zeros to fill

an array of 1024 complex samples. The transmitter signal array is shown for each of these signals along with their compressed output from the matched filter, in Fig. 61. For a strong single fixed clutter the range array consisted of zeros except for two complex samples, one the clutter reflector and the other the target. The clutter reflector was made strong and fixed by using a large constant value for the integer sample, i.e., 6,500 in integer form. The target reflector was made 13 times smaller and was represented by a constant, i.e., 500 with an adjustable range and phase.

After convolution of the transmitter pulse and the reflector array a clutter signal and target echo were generated as 78 sample long replicas of the transmit pulse spaced apart by the same number of samples as the two reflectors. By placing the reflectors less than 78 samples apart the clutter return could be made to overlap the target return.

Colored noise with the same spectrum as the signal was added to the target plus clutter by generating two independent sequences and adding them to the real and imaginary or in-phase and quadrature parts of the signals. For the uncoded pulse 78 samples long a random low-pass noise was generated by taking a sliding sum of 78 elements of a white noise sequence. For the Barker 13 pulse 78 samples long, the subpulses were 6 samples long and therefore the white noise was colored by adding the samples in groups of six. To measure the output noise 160 trials of the noise output were averaged.

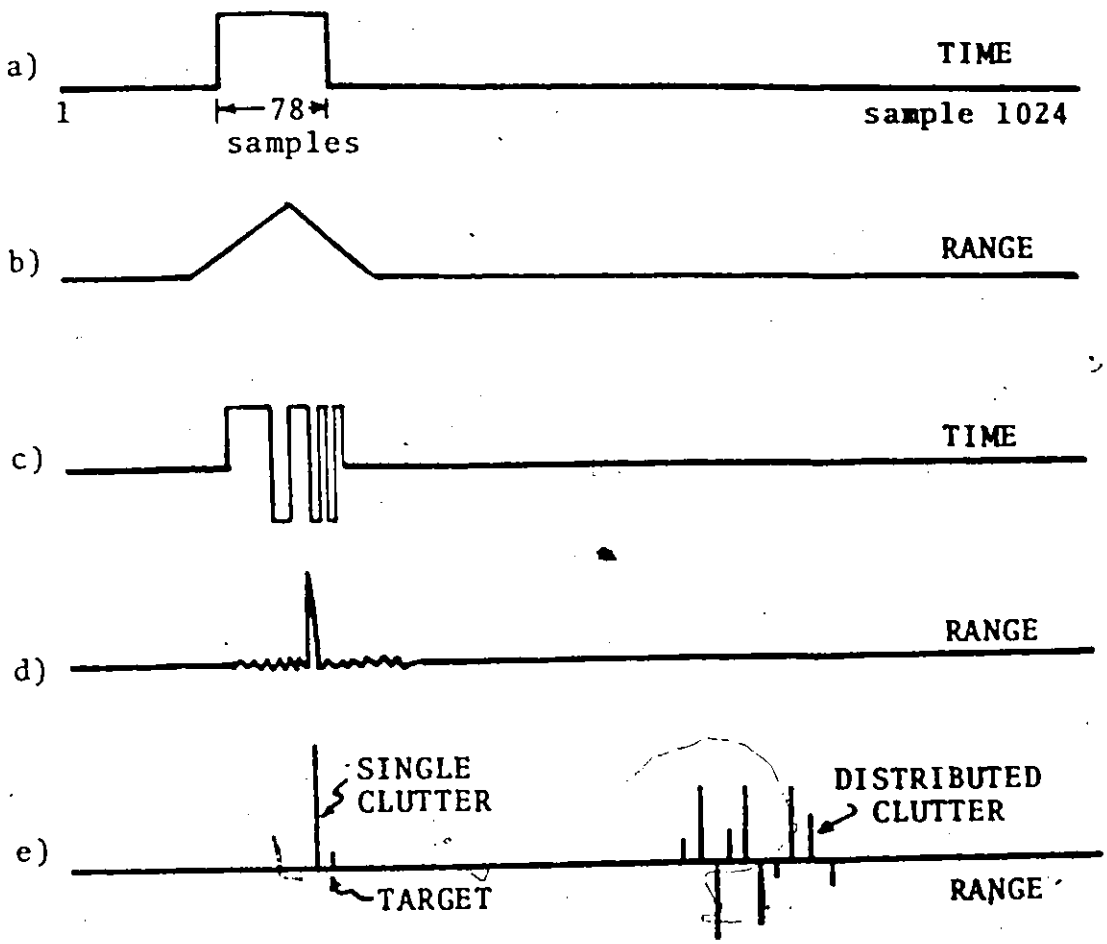

figure 61. The Computer Arrays a) The Uncoded Pulse, b) The Autocorrelation Function of the Uncoded Pulse, c) The Barker 13 Coded Pulse,d) The Barker 13 Autocorrelation Function, e) The Range Space Containing the Clutter Reflectors and the Target.

The Barker 13 was also tested in single fixed clutter using white additive noise.

ii) A 63 Bit Random Code in White Noise and Strong Single Fixed Clutter

A 63 bit random plus and minus sequence was generated by choosing a 63 element sequence of white noise and replacing each positive element by + 5000 and each negative element by - 5000. Two complex samples were used to represent each bit so that the resulting phase-reversal sequence had a length of 126 complex samples. Thirty different random sequences were tested for uniformly low sidelobe structure after matched filtering before settling on one sequence with the lowest sidelobes.

The previous Barker 13 code was replaced by the new 63 bit code and the noise input to the limiter was made to be white. Both 13 to one and 26 to 1 clutter amplitude to target amplitude ratios were tested using 160 transmitter pulses.

iii) Barker 13 in Distributed Fixed Clutter

For this test the transmitter pulse was restored to the Barker 13 and the colored noise with the same bandwidth as the signal was employed.

A new clutter situation was simulated by replacing the single reflector by a series of sixty complex reflectors spaced six samples apart and chosen from a distribution with uniformly distributed phase and Rayleigh distributed amplitude.

This type of fixed distributed clutter was easily generated by choosing the real parts of the reflectors from a

zero-mean Gaussian random sequence and choosing the imaginary parts from another independent Gaussian sequence. In some cases constant amplitude signals could be used and the same result would eventually be obtained by the central limit theorem. However in our simulation, Gaussian distributed numbers could be obtained easily from an analog-to-digital converter connected to a Gaussian random noise generator.

The clutter signal produced by these reflectors was zero over part of the 1024 samples to prevent aliasing of the returns and to allow the SNR in the clear to be measured.

iv Barker 13 in Clusters of Fixed Clutter

The evenly distributed reflectors of the distributed fixed clutter were modified to group the strong amplitudes at particular ranges. This was accomplished by weighting the clutter reflectors by a cosine squared function of range with a period of 100 samples so that strong clusters of clutter appeared along the range axis with a spacing of 100 samples between the clusters. Colored additive noise was used as before.

v Barker 13 in Strong Single Fluctuating Clutter

Fluctuating clutter is simulated by allowing the amplitude and phase of the clutter reflector to vary by a small amount. This is accomplished by modulating the real and imaginary parts of the clutter reflector by two independent slowly varying low-pass random waveforms with a Gaussian power spectrum and approximately a Gaussian probability density function. Barlow [50] has measured the power spectrum of clutter under varying weather

conditions and has found his experimentally measured power spectrum G(f) fits a Gaussian curve where the bandwidth of the spectrum varies with weather and carrier frequency according to the equation:

$$G(f) = \exp\ (-\ a\ f^2/f_o^{\ 2}) \tag{99}$$

where "a" is a parameter depending on the environment and f_o is the radar carrier frequency.

In an environment of heavy wooded hills with a 20 mph wind blowing Barlow finds the parameter $a = 2.3 \times 10^{17}$ in Equation (99). Assuming a carrier frequency $f_o = 1.36$ GHz we find Equation (99) becomes:

$$G(f) = \exp\ (-\ f^2/8) \tag{100}$$

By choosing samples from Fourier-transformed white Gaussian noise and weighting them by the square root of Equation (100) we obtain the sampled frequency weights of Equation (101), shown in Fig. 62:

$$W(k\Delta F) = W(k) = [EXP\ (-\ k^2/8)]^{1/2} \tag{101}$$

where it is implicit that the frequency is sampled at intervals ΔF where ΔF is equal to one Hz. The corresponding slowly varying time sequence was obtained by performing the inverse FFT on a spectrum augmented by zeros to fill an array of 1024 complex samples. A typical time sequence is shown in Fig. 63. Two such real sequences are required to modulate one complex reflector.

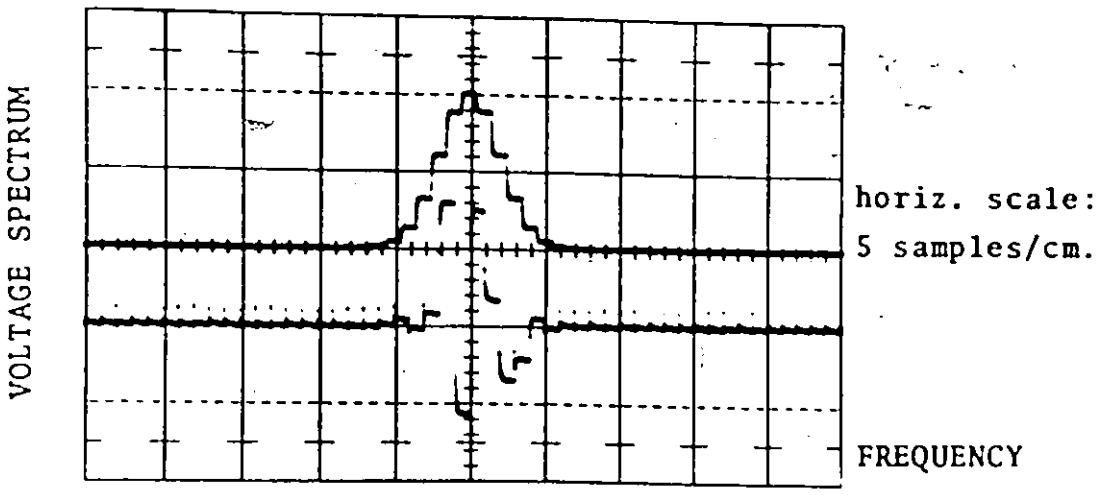

figure 62. The Spectrum of the Fluctuating Component of the Clutter Reflectors. Upper Trace: the Weighting W(k) Equation (101). Lower Trace: a Typical Spectrum Obtained by Weighting White Noise.

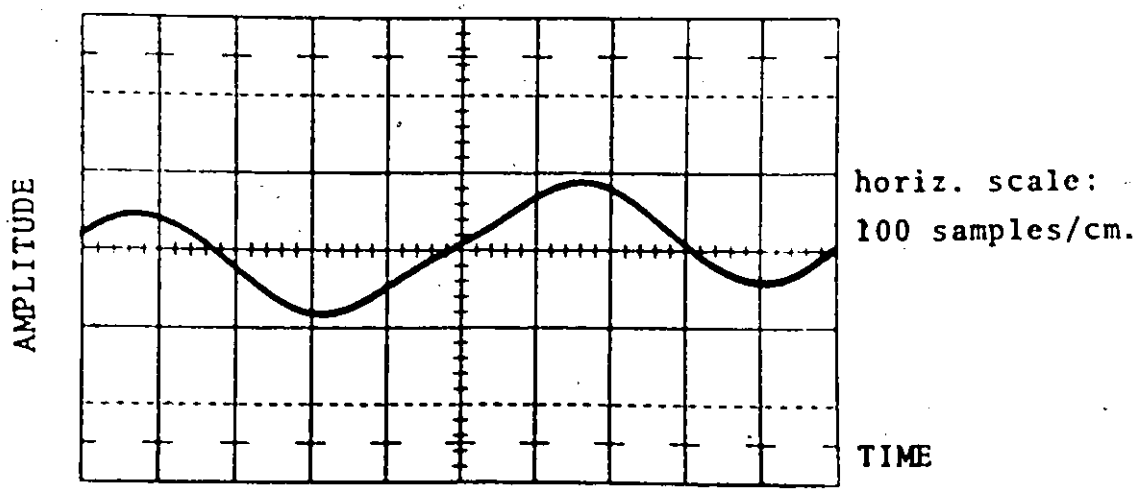

figure 63. A Typical Slowly Varying Component which Modulates the Clutter Reflectors.

The time series which modulates the reflector was stored on a computer disk storage and one element per transmitter pulse was called up to add to each component of the reflector. The modulation index for the clutter was approximately 10%.

This modulation index was chosen to allow the results for fixed clutter to be compared with the results for fluctuating clutter. In the case of fluctuating clutter two additional components of residual clutter are added to the radar receiver noise which reaches the MTI display. The obvious component is that due to the clutter spectrum which passes through the canceller. Another component of the residue is due to the broadening of the clutter spectrum by the limiter [36]. Although for fixed clutter the distortion caused by the limiter does not pass the canceller, for fluctuating clutter any distortions of the clutter return which do not repeat exactly from pulse to pulse will pass through the canceller.

To keep the residue at the MTI display small a low value of the modulation index was used. This was done merely to demonstrate that the residual clutter contribution to the signal-to-noise plus residual clutter limiter loss was additive to the loss due to the time-varying gain fluctuations of the clutter-captured limiter. The 10% modulation level for the fixed clutter was chosen to produce a small additional contribution of residual clutter to be added to the compressed noise of the radar receiver. Too large an index of modulation would tend to swamp the effect we are looking for in residual clutter.

vi Barker 13 in Clusters of Fluctuating Clutter

The clusters of reflectors from the previous case of clusters of fixed reflectors were retained but each reflector was modulated by a slowly varying time sequence with the power spectrum of Equation (100). In this case there were 60 complex reflectors with 120 components to be varied. For each component a 1024 element time sequence was stored on a computer disk storage. Thus $120 \times 1024 \approx 120{,}000$ words of disk storage were used. To facilitate picking up the variations for the reflectors at each transmitter pulse the sequences were weighted for the strength of their component which they would modulate and then the sequences were reordered to place the m^{th} element of each sequence in the same disk location so that after the $m\text{-}1^{th}$ transmitter pulse all the clutter variations for the m^{th} pulse could be retrieved from the disk in one operation.

In this way up to 1024 transmitter pulses could be simulated without interruption. A target was simulated to "fly" from a clear region into the edge of the clutter and also through the clutter itself. The main peak of the target MTI output was tracked with no noise and the target amplitude was recorded.

Chapter 7

Results

The purpose of these simulations was to determine the signal-to-noise ratio loss in a pulse-compression MTI radar with an envelope limiter captured by fixed clutter. In addition some fluctuating reflectors were simulated. The experiments with different types of clutter and different transmit signals and noise will be discussed in the same order as they were presented in the chapter on formulation. Where possible the results will be related to the equation for the SNR at the output of a pulse-compression MTI radar as developed in the previous chapter.

7.1 Results for Fixed Clutter

i) A Comparison between the Barker 13 Phase-Reversal Code and an Uncoded Pulse of the same Length in Strong Single Fixed Clutter

The target amplitude as the range of the target passed through the range of the clutter was reduced as shown in Fig. 64(a). This target output reduction was due to the clutter capturing the limiter and attenuating a portion of the desired echo which overlapped the clutter return. This time-, and hence range-dependent target attenuation $g(t,a)$ affects the mean value of the target output according to Equation (90) which is repeated here for convenience.

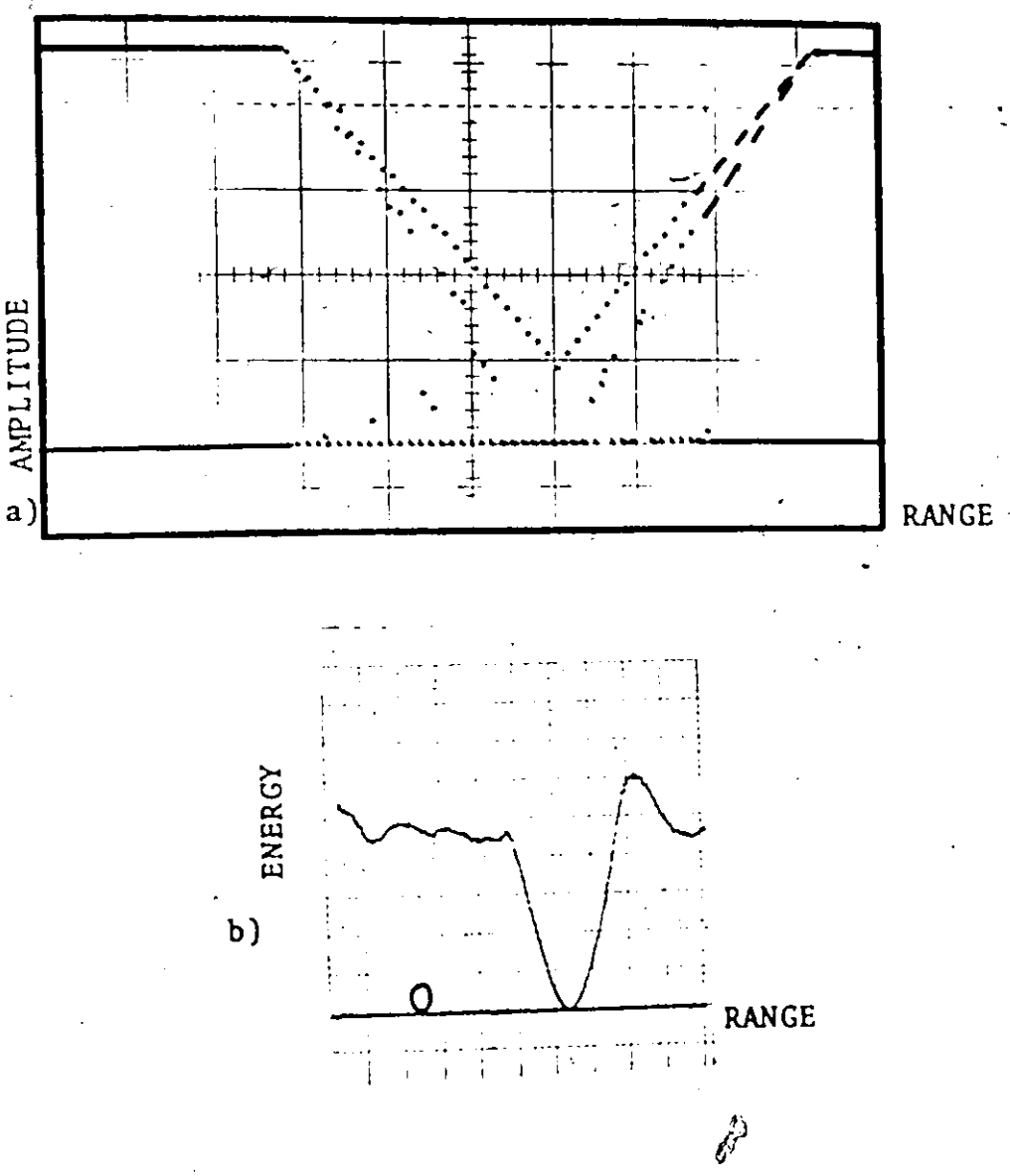

figure 64. Target Amplitude and Energy Versus Range in Strong Single Fixed Clutter. a) Target Amplitude for In Phase and In Quadrature to the Clutter. The Pulse Length is 3.2 cm. Horizontally. b) Target Energy. The Pulse Length is 1.6 Div. Horizontally.

$$\bar{P} = 2j\, e^{j\alpha} \sin\beta \int_{-\infty}^{\infty} g(t,\alpha)\, |r(t)|^2\, dt \qquad (102)$$

The term $j\, e^{j\alpha} \sin$ is a complex constant if we assume as constant the arrival angle α and the angle due to Doppler β, of the target. This constant determines in which channel the compressed target will appear, either in-phase or in-quadrature. In fact up until the two channels are combined at the MTI output the angle of the compressed target return is preserved. However we shall treat the target angle as unnecessary information. The decrease in the mean target output with overlap is due to the target attenuation factor $g(t,\alpha)$ in Equation (102). The integral of Equation (102) has the effect of averaging $g(t,\alpha)$ over the non-zero portion of $r(t)$. Recall $|r(t)|$ is constant since we are considering a constant envelope phase-reversal signal. Hence we may lump the constants in Equation (102) to obtain:

$$\bar{P} = k \int g(t,\alpha)\, dt \Big|_{r(t)\neq 0} \qquad (103)$$

The mean target output is proportional to the mean value of $g(t,\alpha)$ over the transmitter pulse. But $g(t,\alpha)$ is a function of $|c(t)|$ and α through Equation (87) which is repeated here.

$$g(t,\alpha) = \begin{cases} \dfrac{A}{2|c(t)|}\left[1 + e^{-2j(\phi(t)+\alpha)}\right] & |c(t)| > A \\ 1 & |c(t)| < A \end{cases} \qquad (104)$$

where $\phi(t)$ is the angle of $\frac{r(t)}{c(t)}$, which is the phase angle of the echo with respect to the clutter. In Fig. 64(a) there are two target amplitudes shown for $\phi(t) = 0$ and $\phi(t) = \pi/2$, both for $\alpha = 0$. The lower amplitude applies when $\phi(t) = 0$ and the target phase angle is the same as the clutter phase angle.

The variation of $\bar{P}$ with range is seen to be a linear function which agrees with the averaging of $g(t,\alpha)$ in Equation (103). With the target return partially overlapping the clutter return, $g(t,\alpha)$ is equal to one in the clear and a very small value in the clutter. Therefore the target energy decreases as a parabola as shown in Fig. 64(b), for both the uncoded pulse and the Barker 13 coded pulse.

The narrow-band noise which accompanies the uncoded pulse is coherent over the pulse length and therefore behaves the same as the target echo. The narrow-band noise energy was obtained by summing a large number of noise energy matched filter output traces in the presence of strong single fixed clutter. The resultant energy curve was a parabola when the signal and noise bandwidth were equal.

The wide-band noise in the case of the Barker 13 code behaves differently. For a white noise input to the limiter the noise variance V as given by Equation (94) is proportional to the mean squared value of the noise attenuation factor h(t), Equation (88). In strong single fixed clutter the noise energy V is therefore proportional to the length of noise free from overlap with the clutter, see Fig. 65.

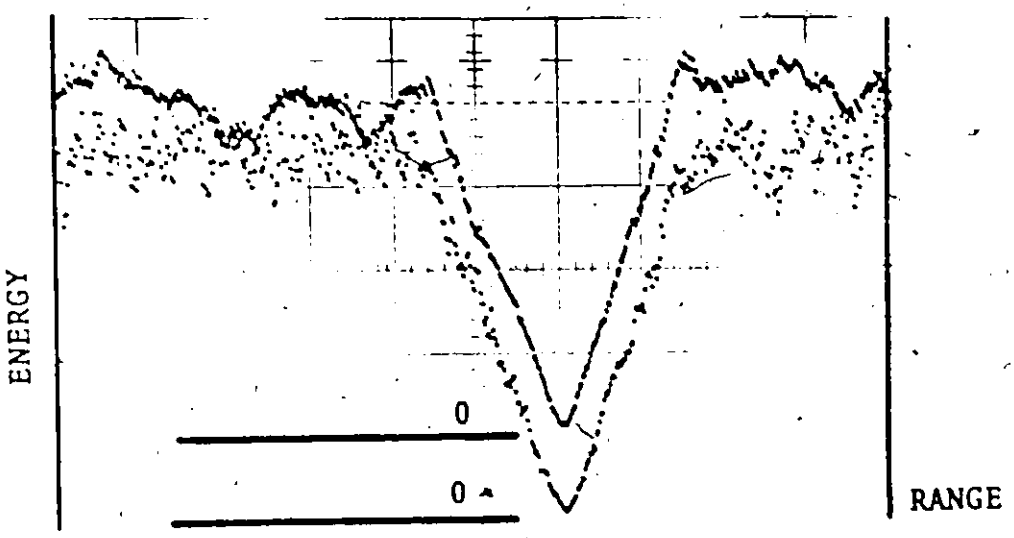

figure 65. Noise Energy Versus Range for White Input Noise to an Envelope Limiter MTI System Captured by Strong Single Clutter.Two Typical Noise Energy Averages are Spaced Vertically One Division Apart. The Pulse Length is 1.6 Divisions Horizontally.

For colored noise with the same bandwidth as the Barker 13 coded pulse the noise variance is more complex. Referring to Equation (93) we see that evaluation of a double integral is required. This is simplified assuming infinite amplitude clutter in Equation (95). A method of visualizing Equation (95) is shown in Fig. 59. The profile of V versus range for infinite clutter is shown in Fig. 66 as calculated from Equation (95).

The measured value of V for the Barker 13 code is shown in Fig. 67. The colored noise is wide-band and is correlated only over the subpulse length. The noise energy is asymmetrical in single clutter as a consequence of the asymmetric code. Although the clutter exceeds the limiter level A by only a factor of ten or less, there is good resemblance between the theory for infinite clutter, Fig. 66, and the measured value of V, Fig. 67.

The shape of the noise energy versus range curve is entirely due to the interaction of the noise attenuation h(t) and the Barker 13 matched filter. In Fig. 68 a noise energy curve is shown which was obtained by matched filtering of colored noise with an attenuated section of a length equal to one pulse length. This curve also shows the asymmetry of the noise.

Dividing V by $\bar{P}^2$ the noise to target energy ratio λ was obtained. For white additive noise with a 13:1 ratio between clutter and target amplitude the increase in noise-to-signal

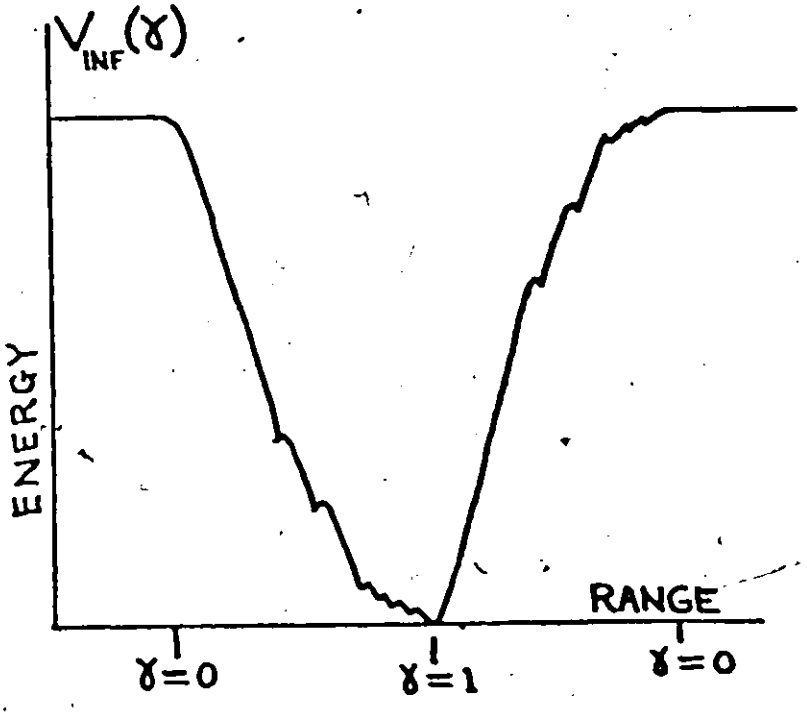

figure 66. Calculated Noise Variance V_{INF} Versus Overlap γ, Barker 13 Coded Pulse with Colored Noise.

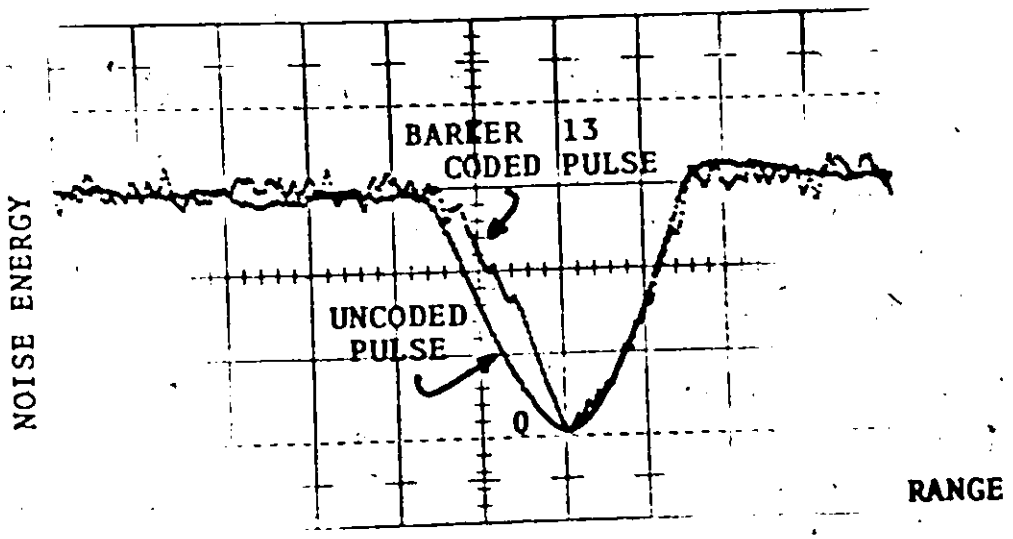

figure 67. Noise Energy Versus Range for an Uncoded Pulse in Narrowband Noise and a Barker 13 Coded Pulse in Colored Noise. Attenuation is Caused by a Strong Fixed Clutter. Pulse Length 1.6 cm. Horizontally.

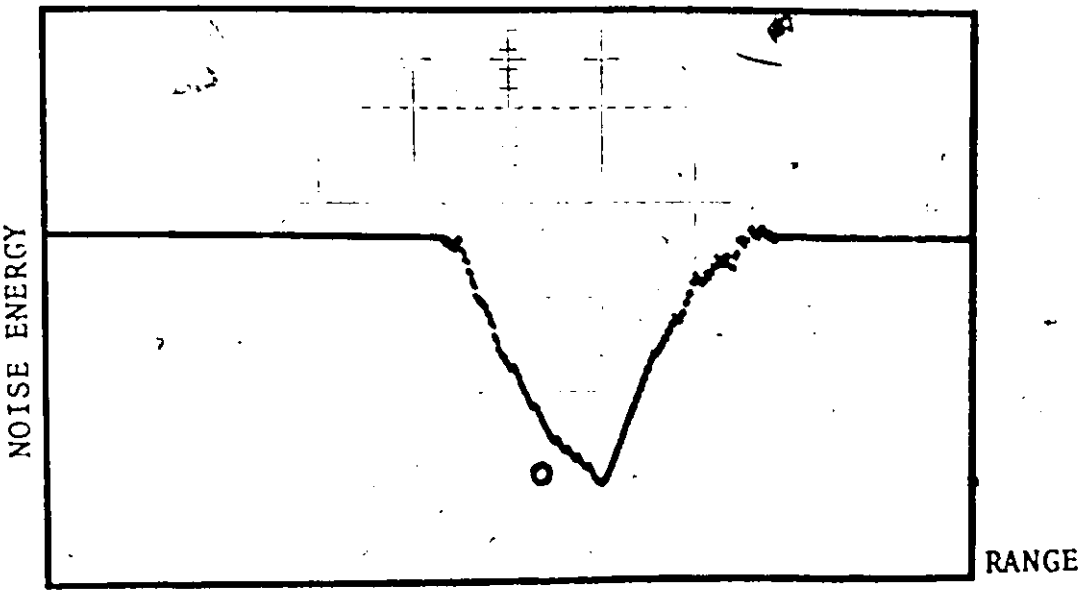

figure 68. Simulation of Noise Energy in Single Clutter by Barker 13 Matched Filtering of Colored Noise With a Section the Length of the Pulse Attenuated by a Factor of 16. Pulse Length 1.6 cm. Horizontally.

ratio is shown in Fig. 69(a). For the case of the Barker 13 coded pulse with additive noise of the same bandwidth as the signal, the noise-to-signal ratio is shown in Fig. 69(b). Theoretical points calculated from the SNR equation for λ, Equation (90) are included for comparison.

At one particular range the SNR loss reaches 5 db for a 13 to one clutter-to-target amplitude ratio. Since for an uncoded pulse in narrow-band noise there is no SNR loss caused by the clutter captured limiter while for the coded pulse in wide-band noise a SNR loss occurs, the uncoded pulse appears to be superior in heavy clutter. This conclusion is misleading however since if both the uncoded and the coded pulse have the same pulse length then the coded pulse will have superior subclutter range resolution and the greater resolution of the pulse-compression system will allow targets to be tracked inside the clutter-captured area. During the simulation a target was moved slowly into the clutter and the returns from equal length pulses, one Barker 13 biphase coded and the other uncoded, were observed. When both returns were partially overlapped by a strong single fixed clutter the range indicated by the central peak of the output of the pulse compression system was able to follow the target into the clutter while the MTI output for the uncoded pulse did not enter the clutter, nor indicate the range of the target as clearly as the pulse-compression system. This is a consequence of the smaller range cell size for the pulse-compression system. The ability of the pulse-compression system to separate targets whose returns

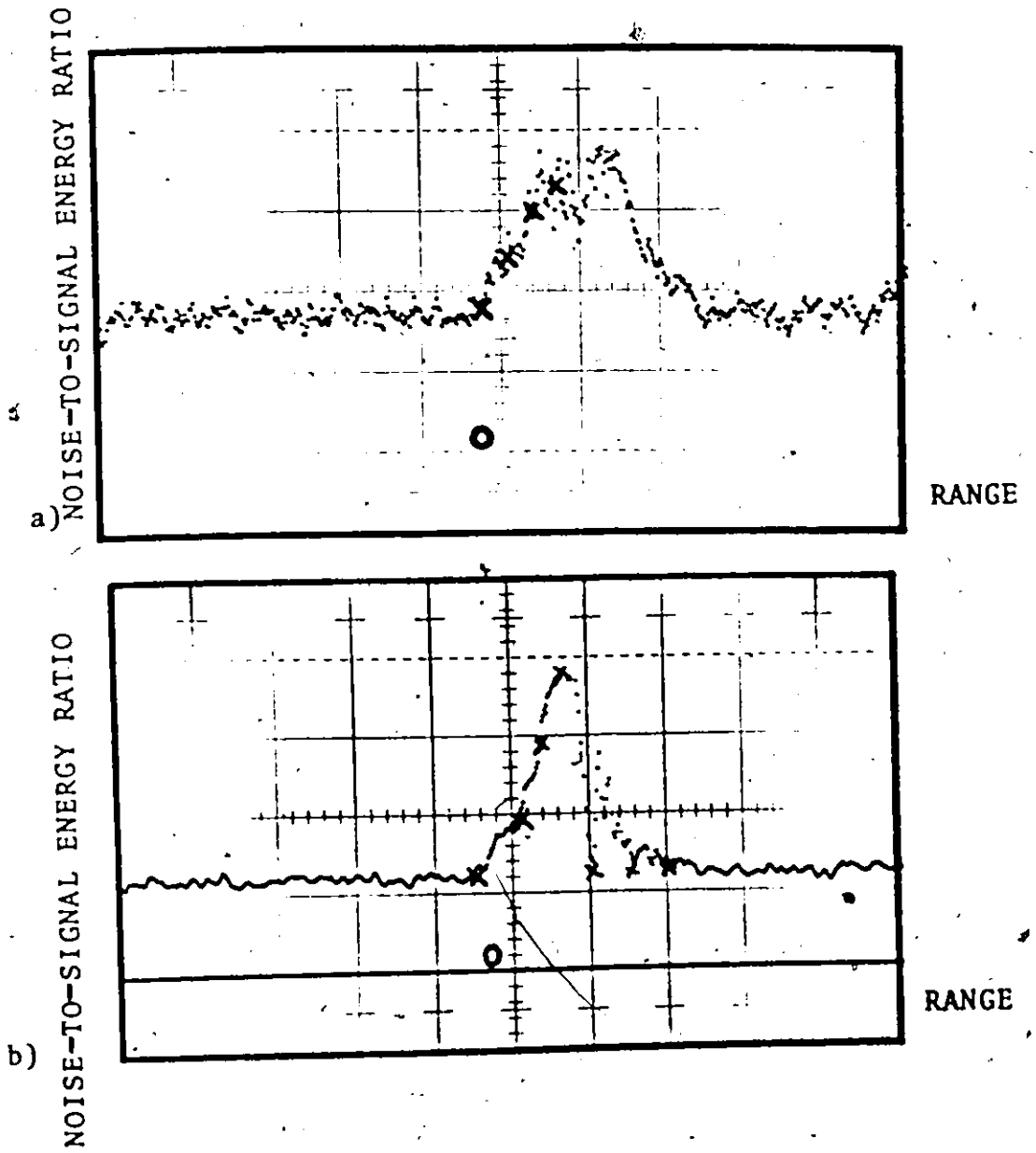

figure 69. Noise-to-Signal Energy Ratio $1/\lambda$ (LINEAR SCALE) for Barker 13 Coded Pulse in Single Clutter, a) With White Input Noise, b) With Colored Input Noise. Pulse Length 1.6 cm. Horizontally. The Crosses are Theoretical Points Calculated from Equation (96).

partially overlap is useful in this case.

ii) A 63 Bit Code in Strong Single Fixed Clutter with White Additive Noise

For the 63 bit code the target amplitude as a function of range was again proportional to the fractional length of the code which was not overlapped by clutter.

The white noise after matched filtering had a noise energy which was also directly proportional to the fractional non-overlapped length.

Two clutter to target amplitude ratios were tested, 13:1 and 26:1. The 13:1 case gives a noise-to-signal energy ratio (not shown) which is very similar to the case of the Barker 13 code in white noise. Other codes with white noise could be expected to give similar results.

The 26:1 case requires some caution in interpretation. With large attenuation of one section of the code by the clutter-captured limiter, at the MTI output the peak-to-sidelobe ratio of the compressed output deteriorates to such a degree that, with this severe clutter interference, some instances in which the sidelobes become as large as the central peak do occur, see Fig. 70(a). However the majority of the largest target peaks do give the correct target range. With this understanding the noise-to-signal energy ratio is given in Fig. 70(b).

For 13:1 clutter-to-target amplitude up to 3 db loss in SNR occurs and for 26:1 clutter-to-target amplitude up to 6.4 db loss was measured. These large losses occur at one

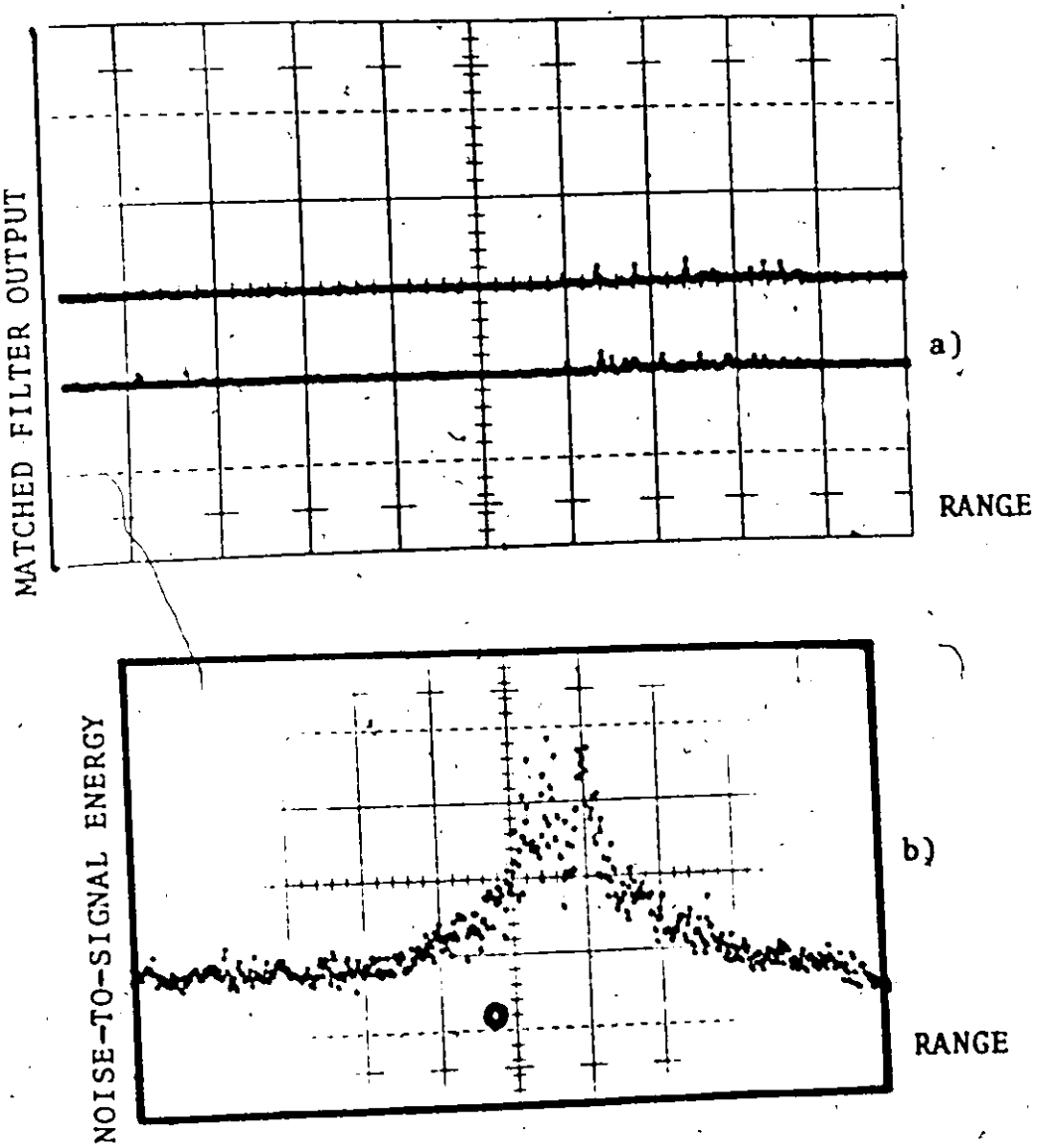

figure 70. 63 Bit Coded Pulse in Strong Single Clutter, a) Two Matched Filter Outputs Distorted by Partially Overlapping Clutter Showing Deterioration in Peak-to-Sidelobe Ratio, b) Noise-to-Signal Energy Ratio for White Input Noise with Clutter of 26 Times the Target Amplitude. Pulse Length 2.0 cm. Horizontally.

particular range where the clutter almost completely overlaps the target return.

iii) Barker 13 in Distributed Fixed Clutter

For this case the clutter return was simulated by the convolution of a Barker 13 code and a field of sixty complex scatterers. The resulting clutter return c(t) was approximately five times larger than the target echo in amplitude and covered a range about four times the length of the code. In this case the theory is very complex but two useful simplifications can be made.

If $|c(t)| >> A$ and c(t) shows rapid phase variations such as when the clutter is due to the superposition of a large number of randomly distributed phase returns from, say rain, then we may apply the principle of stationary phase [51] to $g(t,\alpha)$ and neglect the contribution of $e^{-2j(\phi(t)+\alpha)}$ from Equation (87) to the integral for $\bar{P}$ in Equation (90). Then in the cluttered region where $|c(t)| >> A$ we have:

$$g(t,\alpha) = g(t) = \frac{A}{2|c(t)|} = \frac{1}{\sqrt{2}} h(t) \qquad (105)$$

From the SNR equation for λ, Equation (96) this corresponds to a loss in SNR of 3 db. On the other hand if the phase angle $\phi(t)$ between the clutter and the target is constant modulo π, which may occur when a phase-reversal code is transmitted, and if the phase of c(t) is constant such as when the

clutter is generated by a single strong reflector, we may regard $\phi(t)$ as essentially constant and redefine α to absorb $\phi(t)$ thus:

$$g(t,\alpha) = \frac{A}{2|c(t)|}\left[1 + e^{-2j\alpha}\right] \qquad (106)$$

Now α is the target return phase angle with respect to the clutter and unless the target is at a blind phase, α will change from pulse to pulse. We may treat α as a uniformly distributed stray parameter and substitute Equation (106) into Equation (90). Evaluating the expected value of $|\bar{p}|^2$ we find that the result is equivalent to replacing the $g(t,\alpha)$ by another function $g_{eq}(t)$ which is independent of α and defined in the clutter region by:

$$g_{eq}(t) = \frac{A}{\sqrt{2}|c(t)|} = h(t) \qquad (107)$$

Since $|c(t)|$ is assumed to be constant $h(t)$ is also constant. This indicates that in this case there is no loss incurred in the SNR, since both signal and noise are attenuated by the same constant.

With these two cases in mind we may examine the target and noise amplitudes as they encounter evenly distribued clutter, Fig. 71. The noise represented by the seemingly solid line was obtained by summing the MTI noise output energy for 160 pulses. The largest target peaks were plotted at the range

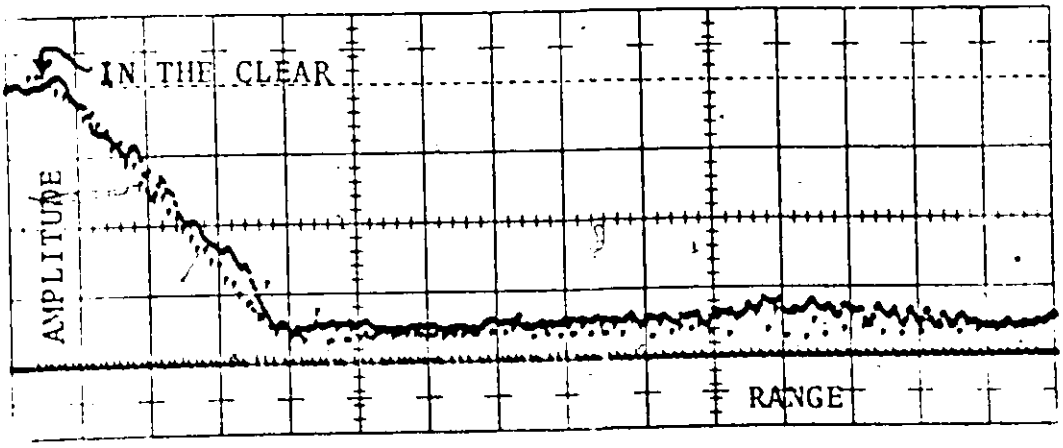

figure 71. Barker 13 Coded Pulse with Colored Input Noise Enters Distributed Clutter Showing the Amplitude of the Noise (Solid Curve) and the Amplitude of the Target (Dots of Lower Trace). The Pulse Length is 3.2 cm. Horizontally.

where they occurred as a simulated target flew from the clear region into the distribution clutter. In the clear in Fig. 71 the signal and noise appear equal. As the clutter is entered a range is encountered where the target echo is almost completely overlapped by clutter; at this range the SNR loss is 2 db. Inside the clutter the target amplitude varies rapidly due to the varying phase angle between the target and the clutter.

Inside the clutter the SNR loss is 3 db which is in agreement with Equation (105) for the case of rapidly varying phase.

iv) Barker 13 in Clusters of Fixed Clutter

For this case the clutter reflectors were grouped into a cosine squared amplitude pattern with a range between clusters slightly longer than that of the coded pulse. A Barker 13 code was used and colored noise with the same bandwidth as the signal was added to the clutter. In this case the clutter amplitude was strongly time-varying.

It has already been determined that the target signal amplitude $\bar{P}$ varies as the mean value of $g(t,\alpha)$ as shown by Equation (103). The target gain factor $g(t,\alpha)$ is averaged over a time duration equal to the pulse length, at a time corresponding to the range of interest.

The noise contribution at the range of interest may also be evaluated from Equation (93) which simplifies for the case of white noise to Equation (94) which is repeated here for

clarity.

$$V = 2 N_o \int_{-\infty}^{\infty} |h(t)|^2 \; |r(t)|^2 \, dt \qquad (108)$$

From Equation (108) the noise amplitude is proportional to the RMS of the noise gain factor h(t). For long codes and wide-band colored noise it is still essentially true that the noise amplitude is proportional to the RMS of h(t).

For clutter which varies strongly in amplitude with range (i.e., time) both g(t,α) and h(t) will be time-varying functions. Therefore the target-to-noise energy ratio (SNR) varies with range and the SNR is proportional to the square of the ratio of the mean value of g(t,α) to the RMS value of h(t).

If g(t) = h(t) as in Equation (107) then the ratio of the mean to RMS of g(t) is always less than or equal to one.

As an example consider a Barker 13 phase-reversal code in white noise with strong clutter capturing the limiter to a time-varying degree so that three subpulses of the code are in the clear and the others are reduced to zero. Then g(t) = h(t) = 1 over the first three bits and g(t) = h(t) = 0 elsewhere. For this example the mean value of h(t) is 3/13 and the RMS is $\sqrt{3}/13$ and a 5 db SNR loss occurs.

In the experiment simulated with clusters of clutter the noise amplitude and target amplitude as functions of range

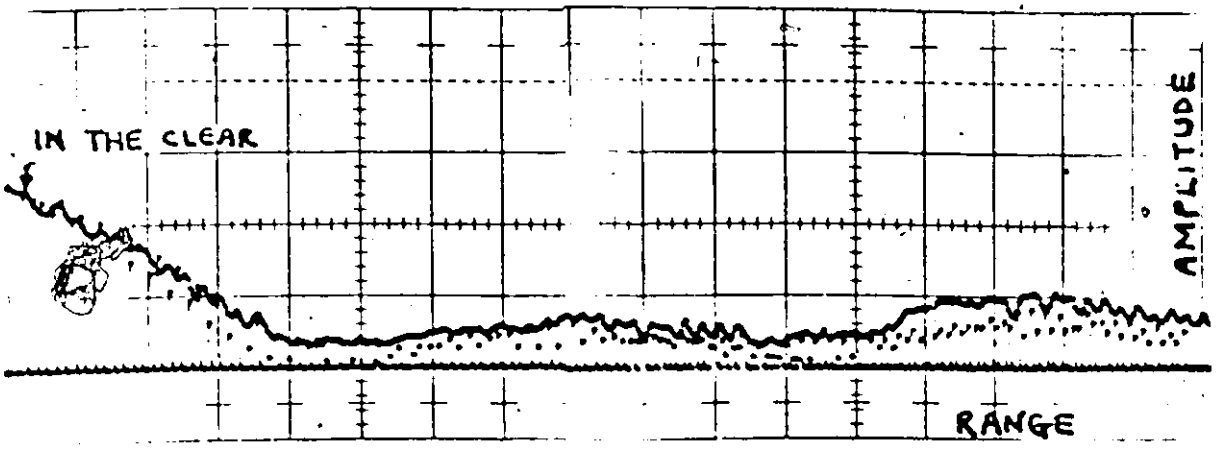

b)

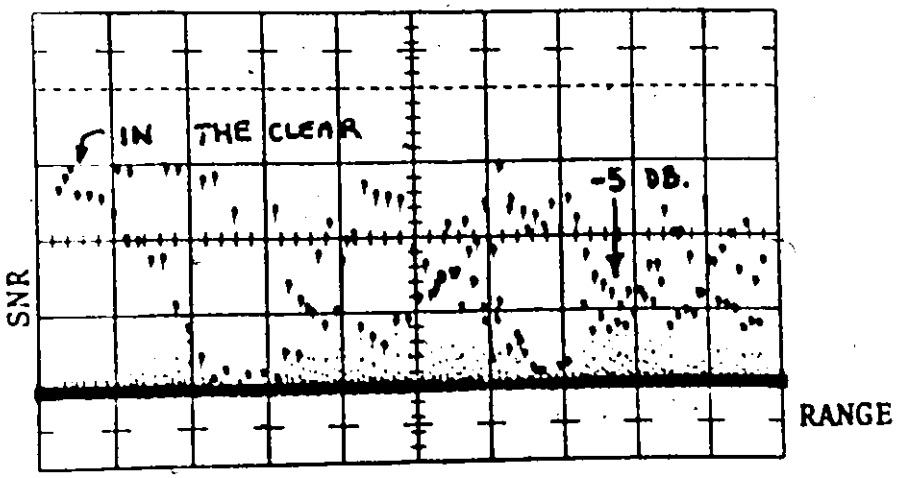

figure 72. Barker 13 in Clusters of Fixed Clutter with Colored Input Noise a) Noise (Upper Trace) and Target Amplitude (Lower Trace). The Pulse Length is 3.2 cm. Horizontally. b) Signal to Noise Energy Ratio (SNR) on a Linear Vertical Scale Obtained From the Data of Fig. 72(a). The Pulse Length is 1.6 cm. Horizontally.

are shown in Fig. 72(a). The corresponding SNR is shown in Fig. 72(b). The SNR is seen to fall from its maximum value as the clutter is entered and two separate loss curves appear as the target alters its phase by $\pi/2$. The SNR never exceeds its "in the clear" value and at one particular range shows a SNR loss of 5 db for both in-phase and in-quadrature to the clutter.

7.2 Results for Fluctuating Clutter

The spectrum of clutter from fixed reflectors is an impulse at zero frequency. This type of clutter was used initially in the simulated experiments because it had the convenient property that all the clutter at the MTI output could be removed by a single delay-line canceller. A single delay-line canceller has the block diagram shown in Fig. 73. We shall consider the video signal to be complex therefore a phase-coherent canceller was simulated.

The frequency response of a phase-coherent canceller is given by Equation (109).

$$H(j\omega) = 1 - e^{-j\omega T} \tag{109}$$

where T is the time of the delay-line. The magnitude of the frequency response is shown in Fig. 74 along with the spectrum of fixed clutter $G_1(f)$.

When an additional Gaussian clutter spectrum component was simulated by modulating the amplitude and phase of the clutter reflectors a new clutter

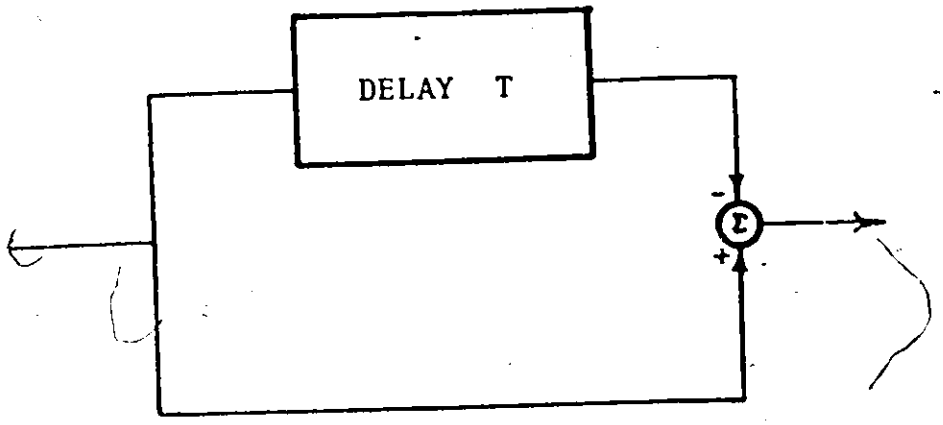

figure 73. Single Delay-Line Canceller.

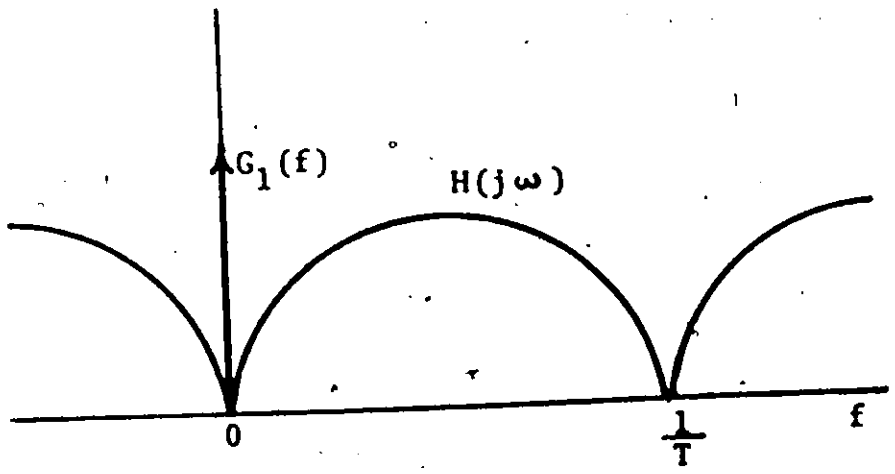

figure 74. The Spectrum of Fixed Clutter and the Transfer Function of a Single Delay-Line Canceller.

spectrum $G_2(f)$ resulted and a clutter residue remained after the canceller, (see Fig. 75). To a certain degree the residual clutter can be reduced by employing delay-line cancellers of a higher order, (see Fig. 76).

The purpose of this investigation was not to explore the possibilities of high order cancellers but was to test the SNR losses due to a clutter-captured limiter in pulse-compression MTI radar under realistic conditions. It can be argued that the fixed clutter with a clutter power spectrum of zero bandwidth is not realistic. Therefore a few of the most important simulations made with fixed clutter were repeated with a fluctuating clutter-component with a Gaussian power spectrum.

v) Barker 13 in Strong Single Fluctuating Clutter

The Barker 13 coded pulse was used with colored noise of the same bandwidth and the limiter was captured by the single fixed clutter. The profile of the noise energy versus range is shown in Fig. 77. This noise trough is asymmetrical also, as is the noise trough for the Barker 13 with stationary clutter. Comparing Fig. 67 for fixed single clutter and Fig. 77 for fluctuating clutter we can see two principal differences. The first difference is that the asymmetry of the two curves is reversed right to left. This is easily explained by the fact that the Barker 13 code was simulated in the reverse time-order to see the effect on the asymmetry. As expected the asymmetry was reversed. This shows that the asymmetry of the noise trough is a property of the code and was not due to any

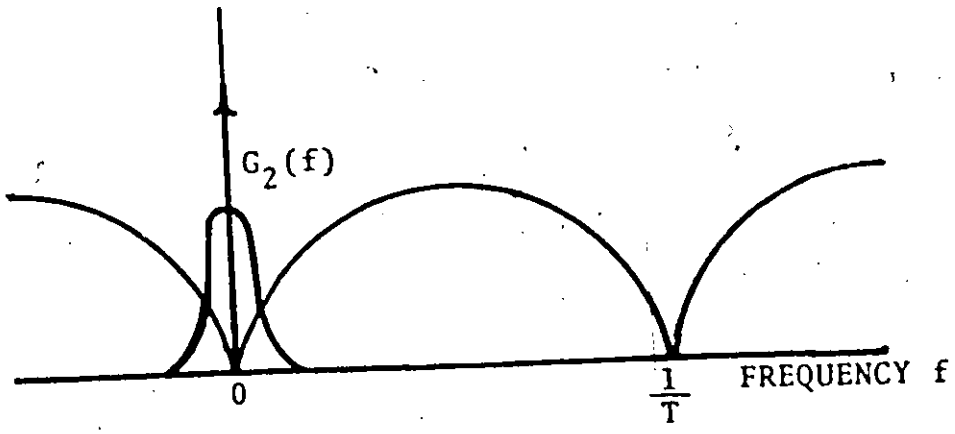

figure 75. The Clutter Power Spectrum $G_2(f)$ Generated by Fluctuating Reflectors and the Transfer Function of a Single Delay-Line Canceller.

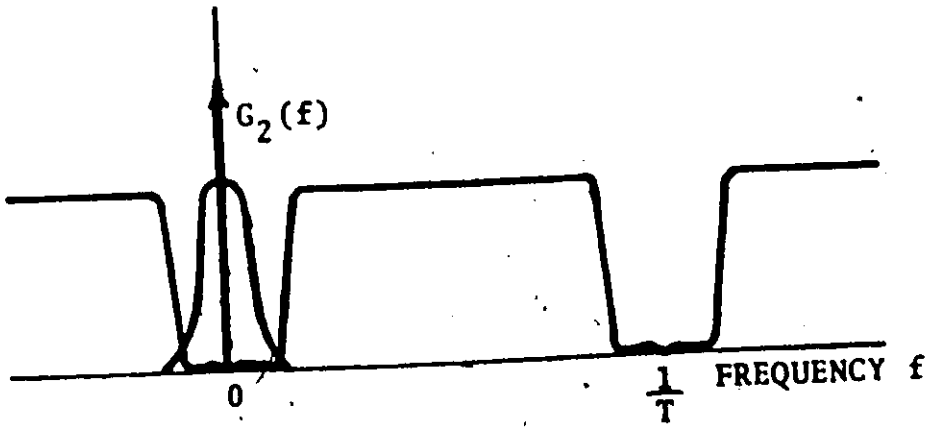

figure 76. The Clutter Power Spectrum $G_2(f)$ Generated by Fluctuating Reflectors and the Transfer Function of a High-Order Delay-Line Canceller.

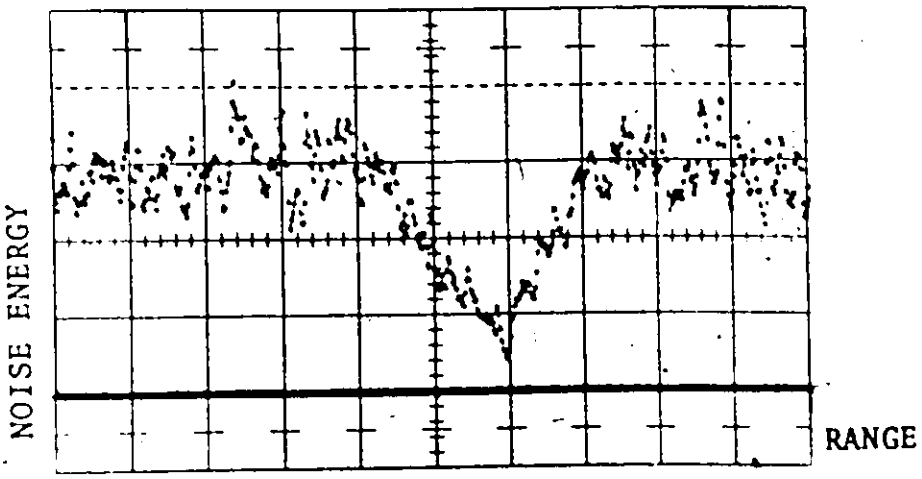

figure 77. Noise Energy Versus Range for a Single Strong Fluctuating Clutter Reflector. Barker 13 Coded Pulse with Colored Input Noise of the Same Bandwidth as the Coded Pulse. The Pulse Length is 1.6 cm. Horizontally.

systematic error.

The second principal difference for fluctuating clutter is that the trough is partially filled in at the bottom by residual clutter. Where the noise energy falls almost to zero (i.e., 2%) at the location of the clutter reflector in Fig. 67 for the fixed case, the noise plus residual clutter energy of Fig. 77 falls only to about 16% of the in the clear value. Also the noise plus residual clutter energy is slightly higher along the sides of the trough for the case of the fluctuating reflector. The target energy is the same as that of the fixed clutter case. Our conclusion therefore is that the noise plus residual clutter profile versus range is identical to that for a fixed reflector except for the addition of residual clutter to the noise energy. Thus the two effects which reduce sub-clutter visibility, namely residual clutter, and deterioration in SNR due to the envelope limiter, can be treated separately.

vi) Barker 13 in Clusters of Fluctuating Clutter

The Barker 13 coded pulse was used with colored noise of the same bandwidth and the limiter was captured by clusters of fluctuating clutter. Each clutter reflector used for the case of fixed clutter was modulated separately by a slowly varying time sequence with a Gaussian power spectrum given by Equation (101). The modulation index of each reflector was the same and was approximately 10% although the change in clutter amplitude on a pulse-to-pulse basis was very small, i.e., less than 1/2%.

In Fig. 78(a) we see the noise plus residual clutter amplitude and the target amplitude for the case of fluctuating clutter. The principal difference from Fig. 72(a) the case of fixed clutter is the additional amplitude of the noise plus residual clutter which is entirely due to the additive component of residual clutter. Recall that the clutter was about 15 times larger than the target, hence unless the cancellation is complete the residual clutter can be very large, in fact at one range it becomes almost as large as the "in the clear" value.

Since the reflectors used in both the fixed and fluctuating cases were the same, the difference between Fig. 72(a) for fixed reflectors and Fig. 78(a) for fluctuating reflectors must be due to the addition of residual clutter.

In Fig. 78(b) the signal-to-noise plus residual clutter energy ratio is shown. Comparing Fig. 72(b) for fixed clutter with Fig. 78(b) for fluctuating clutter a large additional degradation is seen due to residual clutter.

7.3 Summarising Remarks

The loss in SNR due to a linear-limiting IF amplifier has been studied for pulse-compression MTI radar. The limiter considered is linear below a threshold A and clips the envelope of any input which exceeds A. The clutter is assumed to exceed the level A by a large amount while the signal plus thermal noise are normally much less than A in magnitude. The principal results apply to the case of fixed clutter producing coherent

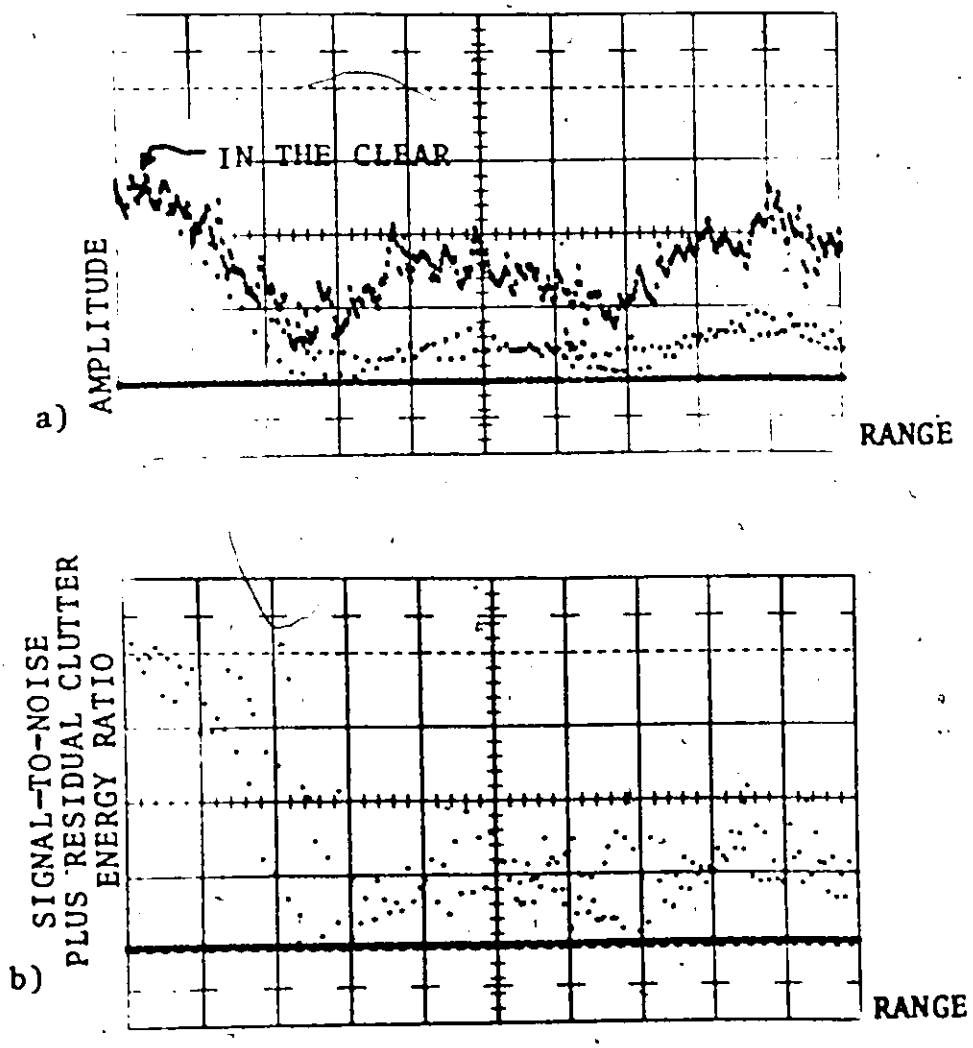

figure 78. Barker 13 Coded Pulse with Colored Input Noise in Clusters of Fluctuating Clutter Reflectors a) Amplitude of Noise Plus Residual Clutter (Upper Trace) and Amplitude of Target (Lower Trace),b) Signal Energy to Noise Plus Residual Clutter Energy Ratio. The " In the Clear" Value is on the Left. The Pulse Length is 1.6 cm. Horizontally in Parts a) and b) and Both Vertical Scales are Linear.

echoes which are completely cancelled in the output by a single delay-line canceller.

Bogotch and Cook were aware of the SNR loss in the captured limiter and after the matched filter, but they measured only the probability of detection at a fixed threshold following the matched filter. This fixed threshold was equivalent to a higher effective threshold in the interference region. Consequently they showed a large drop in the probability of detection and the probability of false alarm in this region.

In our work we have measured the SNR of the desired signal regardless of the drop in noise level due to the clutter-captured limiter. The purpose was to show that the SNR was reduced by a large amount indicating that merely lowering the threshold, or equivalently, increasing the gain in the clutter-captured areas, would not restore the performance to that of a linear system. If sub-clutter visibility is necessary the best available technology must be used to increase the linear dynamic range of the pulse-compression MTI radar.

The measurements presented in this thesis were made using realistic fixed clutter with the same frequency as the transmitted signal; Bogotch and Cook used a continuous wave pulse of a different frequency. Where they limit at or below the RMS noise level we have limited only above the input noise level; thus spectral spreading of the noise was minimized. We have also considered distributed clutter, clusters of clutter, and fluctuating clutter in our simulation. Good agreement between

the mathematical theory and the results of the simulation was shown.

7.3.1 Fixed Clutter

For a narrow-band uncoded pulse the clutter-captured limiter causes the signal and noise energies near a single strong clutter source to both fall parabolically with range and hence the SNR is unchanged. However the uncoded pulse does not provide subclutter visibility. For this purpose for example, the phase-reversal coded pulse provides superior resolution.

The wide-band noise in a pulse-compression system behaves differently from narrow-band noise in a clutter-captured limiter after matched filtering. For a Barker 13 coded pulse with white additive noise the signal and noise energies near a strong single clutter are not reduced at the same rate. After matched filtering the white noise energy is reduced in a linear fashion when approaching a single clutter while the signal energy falls parabolically. Thus inside the clutter where the target echo is partially overlapped by the clutter the SNR deteriorates. The loss in SNR caused by the clutter-captured limiter depends on the clutter-to-target amplitude ratio. For a 13:1 clutter-to-target ratio we have measured 3.3 db SNR loss at one particular range for the Barker 13 code in white noise.

When the wideband noise in the pulse compression sytem is colored and has the same bandwidth as the Barker 13 transmitted pulse the SNR loss is asymmetrical about a strong single clutter. This result is due to the effect of the Barker 13 matched filter on the limiter attenuated noise. For 13:1 clutter-to-target amplitude we have measured up to 5 db SNR loss.

The same type of SNR loss occurs for longer pulse-compression codes. We have measured a 6.4 db SNR loss for a 63 bit phase-reversal code in white noise using a 26:1 clutter-to-target amplitude ratio.

In uniformly distributed clutter the effect of the rapidly varying phase of the clutter causes a 3 db SNR loss. This has been demonstrated for a Barker 13 code with colored noise in a field of sixty distributed clutter reflectors.

In clusters of unevenly distributed clutter the time-varying capture effect of the clutter-captured limiter causes large SNR losses after matched filtering. For a pulse-compression signal the target amplitude at the MTI output is proportional to the mean value of the time-varying limiter attenuation. The noise however is proportional to the RMS value of this attenuation. For a time-varying magnitude the mean is always less than or equal to RMS. We have measured a 5 db SNR loss in clusters of clutter for a Barker 13 code with colored noise.

The SNR losses due to an IF envelope limiter captured by fixed clutter have been summarised in Table III. The error bounds shown were obtained from the variance of the computer simulation results.

The loss is quoted using the particular degree of target and clutter overlap which produces the largest loss. These losses are strongly dependent on the clutter-to-target amplitude ratio and the amount by which the clutter exceeds the limiter threshold. As the clutter-to-target amplitude increases the distortion of the compressed code also increases until the sidelobes of the compressed code exceed the central peak of the compressed code in amplitude. At this level of clutter the range of the target cannot be determined and the detection of the target fails. The 26 to one clutter-to-target amplitude ratio shown for the 63 bit random code is very near to this limit of tolerable distortion and therefore SNR losses exceeding the 6.4 db loss shown would be meaningless.

The large SNR losses due to limiting in pulse-compression systems shown in this thesis do not apply to narrow-band uncoded radar. For these narrow-band cases the work of Davenport [43], Cahn [45] and Jones [46] applies.

7.3.2 Fluctuating Clutter

In high powered land based pulse-compression surveillance radar the clutter return from land and weather reflectors will often exceed the noise level in the receiver combined with any

TABLE III

MAXIMUM SNR LOSS FOR PULSE COMPRESSION WITH IF LIMITER CAPTURED BY FIXED CLUTTER

CLUTTER TYPE	CODE	LIMITING[1]	CLUTTER/TARGET AMPLITUDE RATIO	INPUT NOISE	SNR LOSS[3]	FIG.
SINGLE STRONG	BARKER 13	16 db	13	COLORED[2]	5 ±0.2 db	69(b)
SINGLE STRONG	BARKER 13	16 db	13	WHITE	3.3 ±0.2db	69(a)
SINGLE STRONG	63 BIT RANDOM	20 db	26	WHITE	6.4 ±1 db	70(b)
EVENLY DISTRIBUTED	BARKER 13	12 db	5	COLORED	3 db	71
DISTRIBUTED IN CLUSTERS	BARKER 13	12 db	15	COLORED	5 db	72(b)

1 VOLTAGE RATIO OF CLUTTER TO LIMIT LEVEL

2 COLORED NOISE HAS THE SAME BANDWIDTH AS THE SIGNAL.

3. THE ERROR BOUNDS ARE FOR A 90% CONFIDENCE LEVEL.

noise received from the clutter area by the antenna. Particularly in moving target indicator (MTI) radar with single delay-line cancellers the residual clutter at the MTI output may exceed the noise output. In this case the output signal-to-noise ratio is no longer a realistic measure of performance; in its place the signal-to-noise plus residual clutter ratio determines subclutter visibility.

The signal-to-noise plus residual clutter ratio was measured for a system with a phase-coherent single delay-line canceller. Fluctuating clutter reflectors with a Gaussian clutter power spectrum component were simulated for both a single reflector and clusters of reflectors. For these two cases the limiter loss caused by the pulse compression action of the matched filter on the noise, appears in addition to the signal-to-noise plus residual clutter ratio loss due only to the residual clutter.

In a realistic situation the residual clutter may be due to antenna scanning, clutter fluctuations and also spectral spreading of the clutter by the nonlinearities of the system. For scanning and clutter fluctuations the work of Grissetti, Santa and Kirkpatrick [52] is relevant, while Grasso and Guarguaglini [36] discuss spectral spreading in coherent MTI. Since the residual clutter and the received noise add in mean square to form the denominator of the signal-to-noise plus residual clutter ratio the two contributions namely residue and noise may be studied separately. The contribution of

incoherent noise in pulse-compression systems has been studied in this thesis. In some systems with high residual clutter the limiter loss due to noise may be masked by the residual clutter. Pulse-compression is often suggested as an aid in providing subclutter visibility. The results of this chapter [53] indicate a new source of SNR loss in pulse-compression MTI radar due to thermal noise in a clutter-captured limiter. Similar results have recently been shown for a logarithmic IF limiter [54].

Chapter 8

Conclusions

Pulse-compression techniques for range tracking and surveillance radar have been studied using computer simulation. A fast fixed-point computer (CDC 1700) with an oscilloscope display was used in an interactive fashion to carry out the simulations. The fast Fourier transform was an integral part of each simulation and was used to perform convolution and cross-correlation. The real and imaginary inputs of the fast Fourier transform were used to advantage in two ways:

1) For the tracking studies two delay-lock loops using real signals were simulated to run simultaneously side by side for comparison purposes.
2) For the moving target indicator radar studies complex pre-envelope signals were used to simulate band-pass signals in a mathematically meaningful way.

The computer simulations were necessary to investigate the behaviour of complex nonlinear systems containing decision devices and memoryless nonlinearities.

8.1 Contributions

The important contributions to knowledge included in this thesis may be summarized as follows:

1) The covariance of the output of an FFT cross-correlator has been studied to show that a "largest of" decision is an optimum decision technique for white input noise.
2) A new decision-directed delay-lock loop using FFT cross-correlation has been developed, incorporating the use of different algorithms for acquisition, tracking, detection of unlocking and switching between modes.
3) A new source of signal-to-noise ratio loss in pulse-compression moving target indicator radar systems due to thermal noise in a clutter-captured limiter has been demonstrated [53]. The results were shown to be in good agreement with mathematical theory.

8.2 - Suggestions for Future Work

The following areas of research in radar may be suggested for further study.

1) The use of moving target indicator techniques for tracking a target in fixed clutter using a decision-directed loop suggests itself from the studies reported in this thesis.
2) The signal-to-noise ratio loss in a linear-limiting amplifier may be eliminated by smoothing the effective gain fluctuations of the clutter-captured limiter. A study of fast automatic gain control with a variable time constant for smoothing may be appropriate for pulse-compression radar.
3) The residual clutter produced by spectral spreading, fluctuating scatterers, and antenna scanning warrants further study.

Appendix A

The Error of the Monte Carlo Method

The Monte Carlo method is the method of random trials from which a statistical parameter such as probability or mean value is found. The error of the Monte Carlo method is determined by the number of independent trials and their variance [55]. Usually the variance of the parameter being estimated is not known "a priori". As a rule this variance is found by investigating the variance of the quantities being simulated. In other words, in complicated computational problems the error is estimated from the results of the simulation.

Suppose that a parameter b has an estimated mean value $\bar{b}$ equal to:

$$\bar{b} = \frac{b_1 + b_2 + \ldots + b_N}{N} \qquad (A.1)$$

where the outcomes of individual trials are $b_1, b_2, \ldots, b_N$.

An unbiased estimate of the variance of b is:

$$\hat{V}_b = \frac{(b_1-\bar{b})^2 + (b_2-\bar{b})^2 + \ldots + (b_N-\bar{b})^2}{(N-1)} \qquad (A.2)$$

The variable $\bar{b}$ has a probability distribution which is unknown, with, say, mean μ and standard deviation σ. A theorem called Chebyshev inequality [56] allows the error $|\bar{b} - \mu|$ to be bounded as follows:

$$P(|\bar{b}-\mu| > h\,\sigma) \leq \frac{1}{h^2} \qquad (A.3)$$

where P(.) stands for "probability of". This shows that the probability that $\bar{b}$ assumes a value differing from μ by more than $h\sigma$ is less than $1/h^2$. The utility of Chebyshev inequality is that it holds for any probability distribution.

Closer bounds on the error can be obtained through assumptions about the distribution of $\bar{b}$ obtained from the Central Limit Theorem [57]. For N, the number of trials, greater than about ten, the distribution of $\bar{b}$ is approximately a normal distribution regardless of the distribution of the variables b_i. Thus we may write:

$$P[|\bar{b} - \mu| < \beta\sigma] \doteq \frac{1}{2\pi} \int_{-\beta}^{\beta} \exp\left(-x^2/2\right) dx \qquad (A.4)$$

For a "confidence level" equal to 90% we find $\beta = 1.645$. Other confidence levels give different values for β, e.g., for 95% confidence $\beta = 2$, and for 99.7% confidence $\beta = 3$. Because of the low value of N, say N = 10 to N = 160 trials used in this thesis, the normal curve for the distribution of $\bar{b}$ is only approximate on the tails of the normal distribution. In this case the use of the 99.7% confidence level is not justifiable. Therefore we will use the 90% confidence level and substitute $\beta = 1.645$ into Equation (A.4) to obtain the following Monte Carlo error formula:

$$|\bar{b} - \mu| < 1.645\,\sigma \qquad (A.5)$$

By obtaining an unbiased estimate of the variance σ^2 from $\hat{V}_b$ in Equation (A.2) we may write the Monte Carlo error bounds as:

$$|\bar{b} - \mu| < 1.645 \sqrt{\frac{\hat{V}_b}{N}} = 1.645 \sqrt{\frac{\sum_{i=1}^{N} (b_i - \bar{b})^2}{N(N-1)}} \qquad (A.6)$$

The formula above is useful to calculate the Monte Carlo error bounds in mean values. A slightly different formula is used to estimate the error in measuring probabilities.

Let d_i be a variable equal to unity if an event occurs and equal to zero if the event does not occur. For example an "event" might be a successful acquisition run or loss of lock in a loop. Let p be the probability of the event. In N trials let K be the number of events detected. Then the expectation of K/N is:

$$E\left\{\frac{K}{N}\right\} = \frac{1}{N} \sum_{i=1}^{N} E\{d_i\} = \frac{Np}{N} = p \qquad (A.7)$$

The variance of d_i is:

$$E\{d_i^2\} = 0\,(1-p) + 1(p) - p^2 = p(1-p) \qquad (A.8)$$

The variance of K/N can be calculated from the variance of d_i; thus:

$$E\{(\frac{K}{N})^2\} = \frac{1}{N^2}\sum_{i=1}^{N} E\{d_i^2\} = \frac{p(1-p)}{N} \qquad (A.9)$$

From the Law of Large Numbers there exists a number of trials N such that with probability $1-\epsilon$ the estimate K/N differs from the probability p by less than Δ, which is written:

$$|\frac{K}{N} - p| \leq \Delta \qquad \text{with confidence } (1-\epsilon) \qquad (A.10)$$

The inequality may be estimated by use of the Chebyshev inequality as:

$$|\frac{K}{N} - p| \leq \sqrt{\frac{p(1-p)}{\epsilon N}} \qquad (A.11)$$

The inequality in (A.11) is proved in Feller [56].

The principal conclusion drawn from Equations (A.6) and (A.11) is that the accuracy of Monte Carlo trials increases as $\sqrt{N}$ so that an increase in accuracy by one order of magnitude requires an increase in the number of trials N of two orders.

BIBLIOGRAPHY

1. Bogotch, S., and C. E. Cook, The effect of limiting on the detectability of partially-time-coincident pulse compression signals, IEEE Trans., Vol. MIL-9, No. 1, January 1965, pp. 17-24.

2. North, D. O., An analysis of the factors which determine signal noise discrimination in pulsed carrier system, (reprinted in) Proc. IEEE, Vol. 51, No. 7, July 1963, pp. 1016-1027.

3. Viterbi, A. J., On coded phase-coherent communications, IRE Trans. Vol. SET-7, No. 1, March 1961, pp. 3-14.

4. Jaffe, R., and E. Rechtin, Design and performance of phase lock circuits capable of near-optimum performance over a wide range of input signal and noise levels, IRE Trans., Vol. IT-1, March 1955, pp. 66-76.

5. Viterbi, A. J., Optimum detection and signal selection for partially coherent binary communication, IEEE Trans., Vol. IT-11, No. 2, April 1965, pp. 239-246.

6. Gupta, S. C., On optimum digital phase-lock loops, IEEE Trans., Vol. COM-16, No. 2, April 1968, pp. 340-344.

7. Kuo, B., Analysis and Synthesis of Sampled Data Control Systems, Englewood Cliffs, N. J., Prentice-Hall, 1963.

8. Spilker, J. J. Jr., and D. T. Magill, The delay-lock discriminator an optimum tracking device, Proc. IRE, Vol. 49, No. 10, September 1961, pp. 1403-1416.

9. Middleton, D., An Introduction to Statistical Communication Theory, McGraw-Hill Book Company, New York, 1960, (see p. 141).

10. Viterbi, A. J., Phase-lock loop dynamics in the presence of noise by Fokker-Planck techniques, Proc. IEEE, Vol. 51, December 1963, pp. 1737-1753.

11. Haykin, S. S., and C. Thorsteinson, A quantized delay-lock discriminator, Proc. IEEE, Vol. 56, No. 6, June 1968, pp. 1092-1093.

12. Spilker, J. J. Jr., Delay-lock tracking of binary signals, IEEE Trans., Vol. SET-9, March 1963, pp. 1-8.

13. Nathanson, F. E., Radar Design Principles, McGraw-Hill Book Company, New York, 1969, (see p. 458).

14. Gill, W. J., A comparison of binary delay-lock tracking-loop implementations, IEEE Trans. Vol. AES-2, No. 4, July 1966, pp. 415-424.

15. Viterbi, A. J., Principles of Coherent Communication, McGraw-Hill Book Company, New York, 1966.

16. Ward, R. B., Application of delay-lock radar techniques to deep space tasks, IEEE Trans. Vol. SET-10, June 1964, pp. 49-65.

17. Ward, R. B., and F. L. Strubel, Precision earth-to-satellite range measuements using delay-lock techniques, IEEE Trans. Vol. IM-19, No. 2, May 1970, pp. 118-124.

18. Huff, R. J., and K. L. Reinhard, A delay-lock loop for tracking pulsed-envelope signals, IEEE Trans., Vol. AES-7, No. 3., May 1971, pp. 478-485.

19. Cooley, J. W., P. A. W. Lewis, and P. D. Welch, The fast Fourier transform algorithm and its applications, IBM Research Paper RC-1743, February 1967.

20. Bergland, G. D., Fast Fourier transform hardware implementations a survey, IEEE Trans. Audio and Electroacoustics, Vol. AU-17, No. 2, June 1969, pp. 109-119.

21. Bergland, G. D., A guided tour of the fast Fourier transform, IEEE Spectrum, Vol. 6, No. 7, July 1969, pp. 41-52.

22. Glisson, T. H., C. I. Black and A. P. Sage, The digital computation of discrete spectra using the fast Fourier transform, IEEE Trans. Vol. AU-18, No. 3, September 1970, pp. 271- 287.

23. See Cooley, Lewis and Welch [19], section 4.4, p. 52.

24. Van Trees, H. L., Detection Estimation and Modulation Theory, Part I, John Wiley and Sons Inc., New York, 1968, (p. 258).

25. Bode, H. W., and C. Shannon, A simplified derivation of linear least-square smoothing and prediction theory, Proc. IRE, Vol. 38, April 1950, pp. 417-425.

26. Woodward, P. M., Probability and Information Theory with Applications to Radar, Pergamon Press Ltd., London, McGraw-Hill Book Company, New York, 1953.

27. Woodward, P. M., and I. L. Davies, Phil. Mag., Vol. 41, p. 1001.

28. McMaster University Data Processing and Computing Center documentation: MILIS 41, p. 12.02.

29. Abramowitz, M., and I. A. Stegun, Handbook of Mathematical Functions, National Bureau of Standards, U. S. Government Printing Office, Washington, D. C., fifth printing, 1966.

30. Gradshteyn, I. S., and I. M. Ryzhik, Table of Integrals Series and Products (Fourth Edition), Acedemic Press, New York, 1965, (see Formula 6.561, No. 16).

31. See Van Trees [25], p. 253.

32. Muelsman, L. P., Active Filters, Lumped, Distributed, Integrated Digital and Parametric, McGraw-Hill Book Co., 1970, (p. 233).

33. Schwartz, M., Information, Modulation, and Noise (Second Edition), McGraw-Hill Book Co., New York, 1970, (p. 404).

34. Gold, B., and G. M. Rader, Digital Processing of Signals, McGraw-Hill Book Co., 1969, (p. 51).

35. Skolnik, M. I., (editor), Radar Handbook, McGraw-Hill Book Co., New York, 1969, chapter 17-15.

36. Grasso, G., and P. F. Guarguaglini, Clutter residues of a coherent MTI radar receiver, IEEE Trans., Vol. AES-5, No. 2, March 1969, pp. 195-204.

37. Zeoli, G., IF versus video limiting for two channel coherent signal processors, IEEE Trans., Vol. IT- 17, No. 5, September 1971, pp. 579-586.

38. See Nathanson, [13], p.284.

39. Dugundji, J., Envelopes and pre-envelopes of real waveforms, IRE Trans., Vol. IT-4, No. 1, March 1958, pp. 53-57.

40. Rihaczek, A. W., Radar signal design for target resolution, Proc. IEEE, Vol. 53, February 1965, pp. 116-128.

41. Jones, W. S., R. A. Kempf, and C. S. Hartmann, Practical surface wave chirp filters for modern radar systems, Microwave Journal, Vol. 15, No. 5, May 1972, pp. 43-47.

42. See Skolnik, [35], chapter 17-15, pp. 51-52.

43. Davenport, W. B. Jr., Signal-to-noise ratios in band-pass limiters, J. Appl. Phys., Vol. 24, June 1953, pp. 720-727.

44. Manasse, R., R. Price and R. M. Lerner, Loss of signal detectability in band-pass limiters, IRE Trans., Vol. IT-4, March 1958, pp. 34-38.

45. Cahn, C. R., A note on signal-to-noise ratios in band-pass limiters, IRE Trans., Vol. IT-7, January 1961, pp. 39-43.

46. Jones, J. J., Hard limiting of two signals in random noise, IEEE Trans., Vol. IT-9, January 1963, pp. 34-42.

47. Baghdady, E. J., Lectures on Communication System Theory, McGraw-Hill Book Co., New York, 1961, (see p. 506).

48. Lyons, R. G., The effect of hard limiting on signal to interference ratios, Research Report No. 69-1, Dept. of Mathematics, Queens University, Kingston Ont., February 1969.

49. See Nathanson, [13].

50. Barlow, E. J., Doppler radar, Proc. IRE, Vol. 37, No. 4, April 1949, pp. 340-355.

51. Erdelyi, A., Asymptotic Expansions, Dover Press, New York, 1956.

52. Grisetti, R. S., M. M. Santa, and G. M. Kirkpatrick, Effect of internal fluctuations and scanning on clutter attenuation in MTI radar, IRE Trans. Aeronautical and Navigational Electronics, March 1955, pp. 37-41.

53. Thorsteinson, C., R. de Buda, and S. S. Haykin, The effect of limiting in pulse compression MTI radar, accepted for publication as a summary paper by Proc. IEE, 1972.

54. McLaughlin, R. H., and F. V. Bucciarelli, An investigation of an IF logarithmic amplifier and a limiter, Canadian General Electric Company, Technical information series report RQ71EE5, Toronto, Sept. 1971.

55. Shreider, Y. A., (editor), The Monte Carlo Method, Translated from Russian by G. J. Tee, Pergamon Press, London, 1966.

56. Feller, W., An Introduction to Probability Theory and Its Applications, Second Edition, Wiley, New York, 1957, (p. 219).

57. See Feller, [56].

58. Schwartz, M., W. R. Bennett, and S. Stein, Communication Systems and Techniques, McGraw-Hill Book Co., New York, 1966, (p. 299).

59. Papoulis, A., Probability, Random Variables and Stochastic Processes, McGraw-Hill Book Co., 1965, (p. 241).

60. Ward, M. R., and W. W. Shrader, MTI Performance Degradation Caused by Limiting, EASCON 1968 Record, pp. 168-174.

61. McAuley, R. J., A Theory for Optimal MTI Digital Signal Processing, Part I, Receiver Synthesis, Technical Note 1972-14, Lincoln Laboratory, M.I.T., Lexington, Massachusetts, February, 1972.